NTNU – Trondheim
Norwegian University of
Science and Technology

# The effect of ball-milling lithium hydride with lithium/rare-earth borohydrides

Synthesis, decomposition pathways and
hydrogenation properties

Asgeir Olaf Kydland Lysdahl

Master of Science in Physics and Mathematics
Submission date: June 2013
Supervisor: Randi Holmestad, IFY
Co-supervisor: Bjørn Christian Hauback, IFE
Christoph Frommen, IFE

Norwegian University of Science and Technology
Department of Physics

# The effect of ball-milling lithium hydride with lithium/rare-earth borohydrides
# Synthesis, decomposition pathways and hydrogenation properties

Asgeir Olaf Kydland Lysdahl

Master's thesis, June 2013

Department of Physics, Faculty of Natural Sciences and Technology,
Norwegian University of Science and Technology
NO-7491 Trondheim, Norway

Department of Physics, Institute for Energy Technology
NO-2007 Kjeller, Norway

**Abstract**

Mixed-metal borohydride hydrogen storage composites ($3LiBH_4 + LiLn(BH_4)_3Cl$) and reactive hydride composites ($6LiBH_4 + LnH_{2+\delta}$) (Ln = La, Yb) have been synthesized from $LiBH_4$ and the corresponding rare rare-earth chlorides $LnCl_3$. The thermodynamic properties, decomposition pathways and hydrogenation properties of these composites have been studied. The synthesis was performed with high-energy ball-milling, the thermodynamic properties were studied with differential scanning calorimetry, thermogravimetry and mass spectroscopy, changes in the crystal structure during decomposition and re-hydrogenation were followed with synchrotron-radiation powder X-ray diffraction, and volumetry and IR spectroscopy were used to assess the hydrogenation properties. Synthesis of the desired composites was successful, although additional heating was required for the lanthanum composites, whereas the ytterbium composites released diborane during milling. The decomposition product of each mixed-metal borohydride is $LnH_{2+\delta}$ (Ln = La, Yb), which results in the decomposition of $LiBH_4$ at approximately 300 and 366°C for Ln = La and Yb, respectively. The reactive hydride composites decomposed at 334 and 380°C for Ln = La and Yb, respectively, due to an alternative decomposition pathway involving $LiBH_4$ and $LnH_{2+\delta}$. Decomposition under back pressure has only the effect of increasing the decomposition temperature. Both reactive hydride composites show limited reversibility (around 2 wt% $H_2$ could be re-absorbed). The ytterbium-based composites tend to release diborane during decomposition, making the lanthanum-based samples preferable as hydrogen storage materials, in particular the mixed-metal borohydride composite, which released most (5.5 wt%) hydrogen at the lowest (150 - 350°C) temperature.

# Contents


**1 Preface** **iii**

**2 Introduction** **1**

**3 Theory and Background** **6**
3.1 Solid state physics and crystallography . . . . . 6
3.1.1 Crystal systems, centering and symmetry . . . . . 6
3.1.2 Scattering from crystals . . . . . 9
3.1.3 Indexing of crystal planes . . . . . 11
3.2 Physical and chemical properties of borohydrides . . . . . 12
3.2.1 Thermodynamics of sorption reactions . . . . . 12
3.2.2 Tuning of thermodynamical properties and improving reaction kinetics . . . . . 15
3.2.3 Lithium borohydride . . . . . 18
3.2.4 Previously studied lithium-rare earth borohydrides . . . . . 21

**4 Equipment and Experiments** **25**
4.1 Tools, instruments and programs . . . . . 25
4.1.1 Ball milling . . . . . 25
4.1.2 Sample preparation . . . . . 26
4.1.3 Powder X-ray diffraction . . . . . 26
4.1.4 Synchrotron X-ray diffraction . . . . . 29
4.1.5 Differential scanning calorimetry and Thermogravimetric analysis . 30
4.1.6 Residual gas analysis . . . . . 31
4.1.7 Sieverts technique: Pressure-Composition-Temperature experiments . . . . . 32
4.1.8 Auto-indexing, structure solution and refinement . . . . . 35
4.2 Experiments . . . . . 39
4.2.1 Starting materials . . . . . 39
4.2.2 Sample preparation . . . . . 40
4.2.3 Temperature- and pressure monitored milling, spring 2013 . . . . . 41
4.2.4 SR-PXD measurements . . . . . 41
4.2.5 Supplementary experiments, spring 2013 . . . . . 44

**5 Results** **47**
5.1 Starting materials . . . . . 47
5.1.1 Lithium borohydride . . . . . 47
5.1.2 Lithium hydride . . . . . 50

5.1.3 Rare earth chlorides . . . . . 50
5.2 Synthesis of the composites . . . . . 51
5.2.1 $6LiBH_4 + LaCl_3$ sample composition . . . . . 51
5.2.2 $6LiBH_4 + YbCl_3$ sample composition . . . . . 53
5.2.3 $6LiBH_4 + LaCl_3 + 3LiH$ sample composition . . . . . 55
5.2.4 $6LiBH_4 + YbCl_3 + 3LiH$ sample composition . . . . . 57
5.2.5 Pressure- and temperature monitored ball-milling . . . . . 59
5.3 Decomposition pathways and thermodynamical properties . . . . . 63
5.3.1 $6LiBH_4 + LaCl_3$ decomposition . . . . . 63
5.3.2 $6LiBH_4 + YbCl_3$ decomposition . . . . . 67
5.3.3 $6LiBH_4 + LaCl_3 + 3LiH$ decomposition . . . . . 69
5.3.4 $6LiBH_4 + YbCl_3 + 3LiH$ decomposition . . . . . 73
5.4 Hydrogenation properties . . . . . 76
5.4.1 SR-PXD *in-situ* hydrogenation . . . . . 76
5.4.2 *Ex-situ* hydrogenation and redesorption . . . . . 80

**6 Discussion** **87**

**7 Conclusions** **91**

**8 Abbreviations** **92**

**Appendices** **93**

**A Leakage considerations** **94**

**B Refinement data** **96**

**C Color photo gallery** **100**

# Preface

The ongoing research on hydrogen storage has partly been initiated by the requirement for densely stored energy in cars. In the last year at high school, I wrote an assignment on the efficiency of internal combustion engines, and the findings have triggered my interest in alternative solutions ever since. I was therefore glad to get the opportunity to work with one of the leading teams in the world on synthesis and description of hydrogen storage materials at Institute for Energy Technology (IFE). The experimental work I have done, is in the first place part of a huge international search for a usable lightweight hydrogen storage composite. Secondly, it is a field of basic research which has given me insight in numerous instrumental techniques for material characterization. This work in particular demonstrates that methods in solid state physics like *in-situ* synchrotron-radiation powder X-ray diffraction and Rietveld refinement combined with calorimetry, thermogravimetry and mass spectroscopy effectively can be used to understand the chemical reactions between gaseous and crystalline phases.

The work has partially been based on the student project I accomplished fall 2012, both experimentally and with regard to the obtained results. The superior project was initiated by my supervisor Christoph Frommen, which has guided me throughout the process. Similar systems to those I have studied are at the moment being investigated by researchers at IFE and abroad, and I thankfully appreciate valuable discussions with in particular Jørn Eirik Olsen and Marit Riktor. The work started with analysis of already acquired data and collection of relevant information. Then, supplementary experiments were performed and analyzed. During the process, I became aware of the importance of careful preparation and calibration of self-setup experiments, so that less time has to be spent on uncertainty considerations. However, on the whole, I am satisfied with the process and accomplished what was planned.

I owe a debt of gratitude to my supervisors Christoph Frommen and professor Bjørn Hauback at the Physics Department at IFE, and to others of the staff who taught me how to use the various instruments and programs: Stefano Deledda, Satoshi Hino, Georgios Kalantzopoulos, Henrik Mauroy, Jørn Eirik Olsen, Magnus H. Sørby and Olena Zavorotynska. I will also thank professor Randi Holmestad who agreed to be my formal supervisor at NTNU.

Asgeir Olaf Kydland Lysdahl
June 2013

# Introduction

It has been known for a very long time that hydrogen gas can be used as an energy carrier. Today, hydrogen is produced large-scale by electrolysis of water, and is used for several purposes in chemistry and industry. The electrolyser has historically required a steady input power to operate effectively, but pressurized electrolysers have lately been developed that allow for huge variations in the input power (down to 10% of the maximum capacity in the case of NEL P60[1]). This means that emission-free power sources such as wind mills or solar cells that normally give an uncontrollable variating power output, can be used entirely in the production of hydrogen gas. Sent into a fuel cell, its reduction potential with oxygen is transferred into electrical energy, which can be utilized by all kinds of power consuming devices, and water is the only reaction product. This cycle is a way of transferring energy which does not include fossil fuel consumption and release of climate gases. Alternatively, one can effectively produce hydrogen from hydrocarbons (natural gas), either by conventional combustion or by pyrolysis (anaerobic heating)[2], the latter being an emission-free solution.

The main problem with hydrogen gas is its very low volumetric energy density at atmospheric pressure. The volumetric energy density of hydrogen at 1 bar is 10 $MJ/m^3$, while for gasoline it is 31200 $MJ/m^3$[3]. A modern, gasoline-powered car needs around 360 MJ of chemical energy from hydrocarbons to achieve a driving range of 500 km. If we assume that a fuel cell car had the same effective efficiency, the amount of hydrogen gas at atmospheric pressure needed would displace a volume of 36 $m^3$.

Most of todays fuel cell cars use therefore high pressure tanks where hydrogen is stored at 700 bar (4500 $MJ/m^3$) when fully charged. These cars, which are being produced and has been bought by several retailers, have a driving range of over 400 km. The problem with this system, however, is that this carbon composite gas tank has to have a certain shape (cylindrical with spherical ends) in order to withstand the high pressure. Such shapes are difficult to efficiently integrate in the car structure without using too much space. The Mercedes F125! fuel cell plug-in hybrid prototype (2011)[4] solves this problem by storing 7.5 kg of hydrogen gas in a metal-organic framework medium pressure tank which is integrated in the center tunnel between the front seats and the floor assembly and kept at cryogenic temperature. The gas can be loaded at 35 bar of pressure, such that the heavy and space consuming components required by the high-pressure systems are left out. According to the manufacturer, it has a driving range of 1000 km. Toyota has also previously developed a 350 bar 180 L tank with an integrated Ti-Cr-Mn hydrogen-absorbing alloy that stores 7.3 kg hydrogen[5]. Storage in liquid form in low-temperature tanks is also being explored, particularly by BMW, but this technology will not be discussed here.

Hydrogen can be stored in solid compounds in many ways. Uptake of hydrogen in a host is often divided in two kinds of processes, namely physisorption (adsorption) and

chemisorption (absorption). Under physisorption, the hydrogen is bound as hydrogen molecules ($H_2$) to the surface of the host by weak Van-der-Waal interactions. Examples of porous materials that adsorb hydrogen are carbon-nanotubes and -cones, zeolites and metal organic frameworks (MOF). Their superior advantage over other storage materials is the cycling capacity; they can be charged- and recharged almost an unlimited number of times. These materials should have as high surface-to volume ratio as possible, without decreasing the volumetric energy density too much. The best of todays MOF's have gravimetric storage capacities of $> 6.5$ wt%, which can be even higher when loading the gas at a moderate pressure. but they must be kept at cryogenic temperature because of the low adsorption enthalpy[6]. Chemisorption means that the hydrogen gas molecules are broken into single hydrogen atoms after the physisorption and form stronger covalent bonds with chemically active sites on the surface.

In many cases is hydrogen reacting with the host forming a completely different storage product. The storage materials which has been subject to most research so far are metal hydrides. When a metal hydride is formed, the hydrogen atoms are diffusing into the bulk of the material after chemisorption, where they are bounded to the metal host by chemical bonds, having oxidation number $-I$. The alkali and alkaline earth metals usually form strong ionic bonds with hydrogen (ex. $MgH_2$, LiH), while transitional metals and alloys usually form metal bonds. Here, hydrogen is not strongly bound, but occupy interstitial sites in the host, yielding a non-stoichiometric metal hydride (ex. $YbH_{2.5}$, $LaNi_5H_{6.7}$). Participating in a chemical bond makes the electron enter into a hybridized orbital, which reduces the effective radius of the remaining proton significantly. Consequently, the volumetric hydrogen density is far higher in metal hydrides than in atmospheric hydrogen gas and even liquid form. The absorption reaction should be exothermic, such that the process can be reversed by heating the material.

$MgH_2$ is one of the lightest metal hydrides with a theoretical hydrogen content of 7.5 weight percent (wt%). But sadly, it has a decomposition temperature at 1 bar of over 350°C. A Polymer Electrolyte Membrane (PEM) fuel cell normally operates at $< 100$°C and the idea is that the generated heat is used to decompose the hydride. There are several bimetallic and transitional metal hydrides which fulfill this requirement, for example $LaNi_5H_{6.7}$, but they all tend to be too heavy. The U.S. Department of Energy's targets for 2015 is a gravimetric system capacity of 5.5 wt% (6.5 MJ/kg), a volumetric system capacity of 40 kg/m$^3$ (4680 MJ/m$^3$) and a filling time for 5 kg $H_2$ of 3.3 min[7]. System capacity means that the weight of the technical equipment required to utilize the storage material is part of the calculation. For some prototype solutions embedding a metal hydride, the system capacity is as less than half of the compound capacity. Said shortly, solid state solutions struggle to meet the gravimetric capacity target, while gas tanks struggle to meet the volumetric capacity target.

Therefore, in the last decades, much of the research has been in the field of complex hydrides, because the gravimetric hydrogen density of many of these materials are very high. Complex hydrides are crystalline coordination compounds with hydrogen-containing ligands as complex ions (anions) and metal ions as the counter ions (cations). These metals can be alkali, alkaline earth, rare earth or transitional metals. There has been a lot of focus on complex hydrides containing the ligands $[BH_4]^-$ and $[AlH_4]^-$ since these are lightweight and have large gravimetric hydrogen densities. Bound to a metal ion these ligands form so-called borohydrides (or tetrahydroborates), e.g. $M(BH_4)$ (M beeing an alkaline metal) and alanates (or tetrahydroaluminates), $M(AlH_4)$[8]. For example, $LiBH_4$ has very high gravimetric hydrogen density ($18,5$ wt%) and also a good volumetric energy

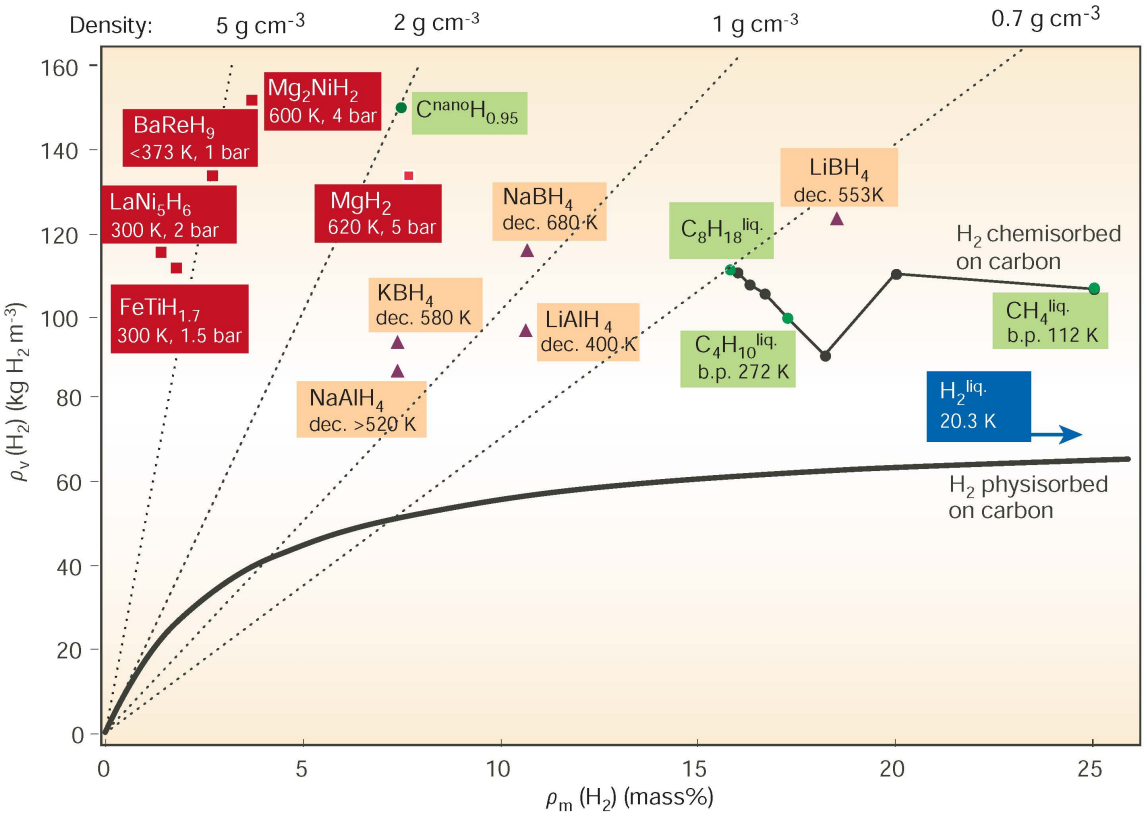


Figure 2.1: Gravimetric and volumetric hydrogen densities for several famous solid state storage materials. (From Nature 2001, vol. 44, page 356[9])

density (43400 MJ/m$^3$). An overview of the gravimetric and volumetric hydrogen densities of different storage materials is depicted in figure 2.1. Metal hydrides are marked red and complex hydrides yellow.

There are important issues that limit the use of lightweight complex hydrides in mobile storage applications, especially the borohydrides. The main problems are high decomposition enthalpy (enthalpy difference between the storage material and the reaction product) and/or low reversibility. $LiBH_4$ is relatively stable and decomposes only when heated above 400°C at 1 bar. The heavier alkali borohydrides are even more stable. $Mg(BH_4)_2$ and the other alkaline earth borohydrides suffer from slow reaction kinetics and are almost impossible to rehydrogenate completely, partially due to the release of boron containing gases. Most fuel cells are severely damaged by diborane. Much effort has been given in order to improve the sorption properties of the relatively inexpensive $Mg(BH_4)_2$. Monometallic borohydrides $M(BH_4)_n$ ($n$ is valence number) of the transitional metals (M = Ti, Mn, Zn, Al) have been synthesized as well, but these have in fact proven to be too unstable. If they do not decompose at standard conditions, which is the case for $Ti(BH_4)_3$, they are irreversible due to low melting temperature and diborane release. The rare-earth borohydride $Y(BH_4)_3$ is stable at standard conditions, but has a high decomposition enthalpy and poor reversibility[10].

However, in 2006 a discovery was made that gave optimism in the search for a well-behaving borohydride. Nakamori et al.[11] investigated the stability of a series mostly known monometallic borohydrides $M(BH_4)_n$ (M = Li, Na, K, Cu, Mg, Zn, Sc, Zr and Hf) by first principle calculations and experiments, and found that the enthalpy of formation

normalized by the number of $[BH_4]^-$ complexes correlates proportionally with the Pauling electronegativity of the cations, $\chi_P$. This suggested that by synthesizing so called mixed-cation borohydrides $MM'(BH_4)_n$, the enthalpy of formation and consequently the thermodynamic properties can be fine-tuned. Also, anion substitution of the $[BH_4]^-$ tetrahedra may alter the charge transfer between the cation and anions and will consequently stabilize or destabilize the crystalline phase. For lithium-based borohydrides, this technique has also the bi-effect of dramatically enhancing the lithium ion conductivity, which makes applications of certain lithium-based borohydrides (for example $LiCe(BH_4)_3Cl$) in battery technology possible[12].

Another way of lowering the decomposition enthalpy is to add compounds that react with the original storage material during decomposition and form more stable end products[13][14]. These materials are called reactive hydride composites. Reaction kinetics can be improved by adding small amounts (typically $1-5$ wt%) of a suitable catalyst or nanostructuring the storage material. The theory related to stability and enthalpy of borohydrides and how the these properties are altered will be deeper reviewed in sections 4.2.5 - 3.2.2.

An often encountered issue of the borohydrides and alanates is their hygroscopic and flammable nature. Complex hydrides also often have low crystallinity, especially when decomposing (example: $Mg(BH_4)_2$), which makes them hard to investigate with diffraction techniques.

Under consideration are also nitrogen-based storage compounds that either liberate hydrogen in the same fashion as complex hydrides (these are based on amide, $LiNH_2$, and imide, $Li_2NH$), or store hydrogen indirect as ammonium in so-called metal ammides (for example $Mg(NH_3)_6Cl_2$). The former compounds show promissory storage capacities, but tend to be plagued by the same drawbacks as the complex hydrides, namely low reaction kinetics. The progress in these new storage materials is however rapidly accelerating. Making reactive hydride composites has also here shown to favorably improve their thermodynamic properties. The latter is a secure way of storing ammonia, but in order to use ammonia as an energy source, it will have to be decomposed, which requires much energy, or a robust solid oxide fuel cell have to be used[6].

To summarize, the requirements a hydrogen storage material has to meet are high gravimetric and volumetric hydrogen densities, low dehydrogenation temperature, good cycling stability, a rehydrogenation time of a few minutes, no explosion risks and low toxicity and cost. In spite of the above mentioned challenges with complex hydrides, there are clear advantages in relation to energy storage in batteries. Compared to batteries, complex hydrides offer much higher volumetric and gravimetric energy densities. The best of todays (2010) prototype hydrogen storage systems have energy densities up to 4.68 MJ/kg and 4.752 MJ/L, whereas the energy density in todays batteries is technology-limited to 0.72 MJ/kg and 0.72 MJ/L[15]. It is not possible to build solid state hydrogen storage systems that can compete with the energy density, low cost and availability (at least for 50 years) of liquid hydrocarbons (i. e. gasoline), but on the contrary, internal combustion engines suffer from a relatively low effective efficiency (especially for gasoline), theoretically bounded by the Carnot efficiency. After more than 150 years of development, it has not exceeded 50% yet. A modern vehicle consuming 0.6 l/10km gasoline (31200 $MJ/m^3$) will have an energy economy of 1.87 MJ/km, whereas the 2012 Honda FCX Clarity is reported[16] to drive 60 miles per kilogram hydrogen (142 MJ/kg[3]), yielding an energy economy of 1.47 MJ/km.

If the cost of fossil fuel production increases significantly and political regulations cre-

ate a suitable economic framework, there will possibly be a demand for energy storage systems where solid state hydrogen storage offers a good solution. As it stands now, it seems uncertain that solid state solutions will be embedded in vehicles, but the infrastructure required to support hydrogen gas filling stations and power networks based on non-stable emission-free power plants will need new ways to store electrical energy in stationary storage systems.

This work will explore two promising hydrogen storage composites based on lithium borohydride and rare earth elements. The choice of materials is based on considerations of previous works on similar systems which will be outlined in the theory section. Theoretical aspects of the sorption processes will be found there as well. The experimental part will be divided in two; one chapter is reserved the description of the utilized techniques and instruments, and the second part covers the numerical and instrumental details of the experiments. Lastly, the results will be presented and guided by a discussion of the properties of the chosen samples.

# Theory and Background

The first part of this chapter will cover some important theoretical principles which will be used in the later analyses. This includes the theory on description of crystals (crystal systems and symmetry) and the theory of scattering from crystals. More practical features concerning experimental setups and software implementations of the theoretical framework will be discussed in chapter 4. In the second part of this chapter, the hydrogen storage properties of borohydrides will be elucidated by considering both reported experimental facts and theoretical predictions of the thermodynamical behavior. We will in this way be able to constrain this study to a few selected systems.

## 3.1 Solid state physics and crystallography

### 3.1.1 Crystal systems, centering and symmetry

A crystal lattice is a periodic mathematical construction of points in space. At each lattice point, we assign a basis, which is a collection of one or more atoms at specific coordinates. A lattice with a basis thus describes a crystal. A repeating unit in the lattice is called a unit cell. It is often described by a set of vectors $\vec{a}$, $\vec{b}$, $\vec{c}$. A lattice vector, which starts at a lattice point and ends at a lattice point can be described as $\vec{R} = n_1\vec{a} + n_2\vec{b} + n_3\vec{c}$, where $n_1$, $n_2$ and $n_3$ are integers. If there is only one lattice point per unit cell, it is called a primitive unit cell.

Three or more lattice points which do not lie on a line span a crystal plane. The periodicity of the lattice will give the plane infinitely many lattice points. A crystal plane is commonly denoted $(hkl)$ where $h$, $k$ and $l$ (called the Miller indices) are the reciprocals of the distance from the cell origin to the plane along $\vec{a}$, $\vec{b}$ and $\vec{c}$, respectively, divided by any common factor. The direction from origin to some lattice point is denoted $[n_1n_2n_3]$, where $n_1$, $n_2$ and $n_3$ are chosen such that $\vec{R}$ points in the same direction[17].

Many non-primitive unit cells can be chosen to describe a crystal, but there is a set of centering conventions which is much used in crystallography and solid state physics. These centering types are listed in in table (3.1).

There are 7 types of crystal systems. With the centering types listed above, it gives in total 14 so-called Bravais lattices. These are shown in figure 3.1. The triclinic lattice has a unit cell where all three angles and all three side lengths are unrestricted. In the monoclinic lattice, there is one unrestricted angle, and two right angles ($\alpha = \gamma = 90°$). The side lengths $a$, $b$ and $c$ are still unrestricted. As the figure shows, it is possible also to have a C-face centered monoclinic unit cell. For the orthorhombic lattice, which has three right angles and three unrestricted sides, the four possible unit cells $P$, $C$, $F$ and $I$ are shown. The tetragonal lattice has three right angles and two sides of equal length. The two possible unit cells $I$ and $P$ are shown. If the lattice is cubic, the primitive cell is called

Table 3.1: Conventional crystallographic centering types. In the third column, the coordinates in side lengths for lattice points in addition to the point defining the lattice (chosen to be in origin) are shown. (1/2, 1/2, 1/2) means that there is a lattice point at $\frac{1}{2}(\vec{a}+\vec{b}+\vec{c})$

| Symbol | Type | Coordinates for lattice points in addition to (0, 0, 0) | Points per unit cell |
|---|---|---|---|
| P | Primitive | - | 1 |
| I | Body centred | (1/2, 1/2, 1/2) | 2 |
| A | A-face centred | (0, 1/2, 1/2) | 2 |
| B | B-face centred | (1/2, 0, 1/2) | 2 |
| C | C-face centred | (1/2, 1/2, 0) | 2 |
| F | All face centred | (0, 1/2, 1/2), (1/2, 0, 1/2), (1/2, 1/2, 0) | 4 |
| R | Rhombohedrally centred | (1/3, 2/3, 2/3), (2/3, 1/3, 1/3) | 3 |

simple cubic ($SC$), the body centered unit cell is called body centered cubic ($BCC$) and the all face centered unit cell is called face - centered cubic ($FCC$). In addition, there is the trigonal (all sides equal and all angles unrestricted) and the hexagonal system. The latter is the honeycomb lattice: Two right angles and one angle of 120°, which plane is normal to the unrestricted side length $c$[18][17][19].

There is a certain set of symmetry operations which can be performed on a given crystal, and a symmetry element is related to each symmetry operation. The possible symmetry operations are the following: $n$-fold rotation about an axis (after a rotation of $\frac{360°}{n}$, the crystal resembles itself), inversion about a point, mirroring through a plane, rotation and translation (a screw axis), and lastly mirroring and translation (a glide plane). When the symmetry operation is a rotation, then the symmetry element is the rotation axis. The mirror plane is the symmetry element of a mirroring and so on. A rotation axis is denoted with the number $n = 1, 2, 3, 4, 6$, and a bar above the number indicates the existence of an inversion point on the rotation axis. In three dimensions, there are no 5-fold symmetry. For a screw axis, an integer $p$ is added as a subscript to the symmetry element: $n_p$. Suppose $n$ lies along the $z$ axis with a lattice constant $c$. Then, after a $n$-fold rotation, the crystal must be translated an amount of $(p/n)c$ in the $z$ direction in order to resemble itself. Furthermore is a mirror plane denoted by the letter $m$, axial glide planes by $a$, $b$ or $c$ (not to be confused with the lattice constants) and diagonal glide planes by the letter $n$. An axial glide plane $a$ exists if the crystal can be mirrored about a plane and then translated parallel to that plane by the amount $\frac{a}{2}$ in the $x$ direction. The similar convention yields the $y$ and $z$ directions. Diagonal glide planes $n$ consist of $m$ and the translation component $\frac{\vec{a}+\vec{b}}{2}$, $\frac{\vec{a}+\vec{c}}{2}$, $\frac{\vec{b}+\vec{c}}{2}$ or $\frac{\vec{a}+\vec{b}+\vec{c}}{2}$. Finally, the notation $\frac{3}{m}$ means a mirror plane normal to a three-fold axis[18].

There will exist several equivalent symmetry elements within a unit cell. The collection of all symmetry elements assembles the space group of the crystal. There are 230 irreducible space groups. The smallest part of the unit cell that will generate the whole unit cell by application of symmetry operations, is called an asymmetric unit[18].

For triclinic systems, there are only two space groups, namely $P1$ and $P\bar{1}$. For monoclinic systems the space group is characterized by the centering type $(P, C)$ and a symbol giving the symmetry in the $y$ direction. For orthorhombic space groups, the symmetries of

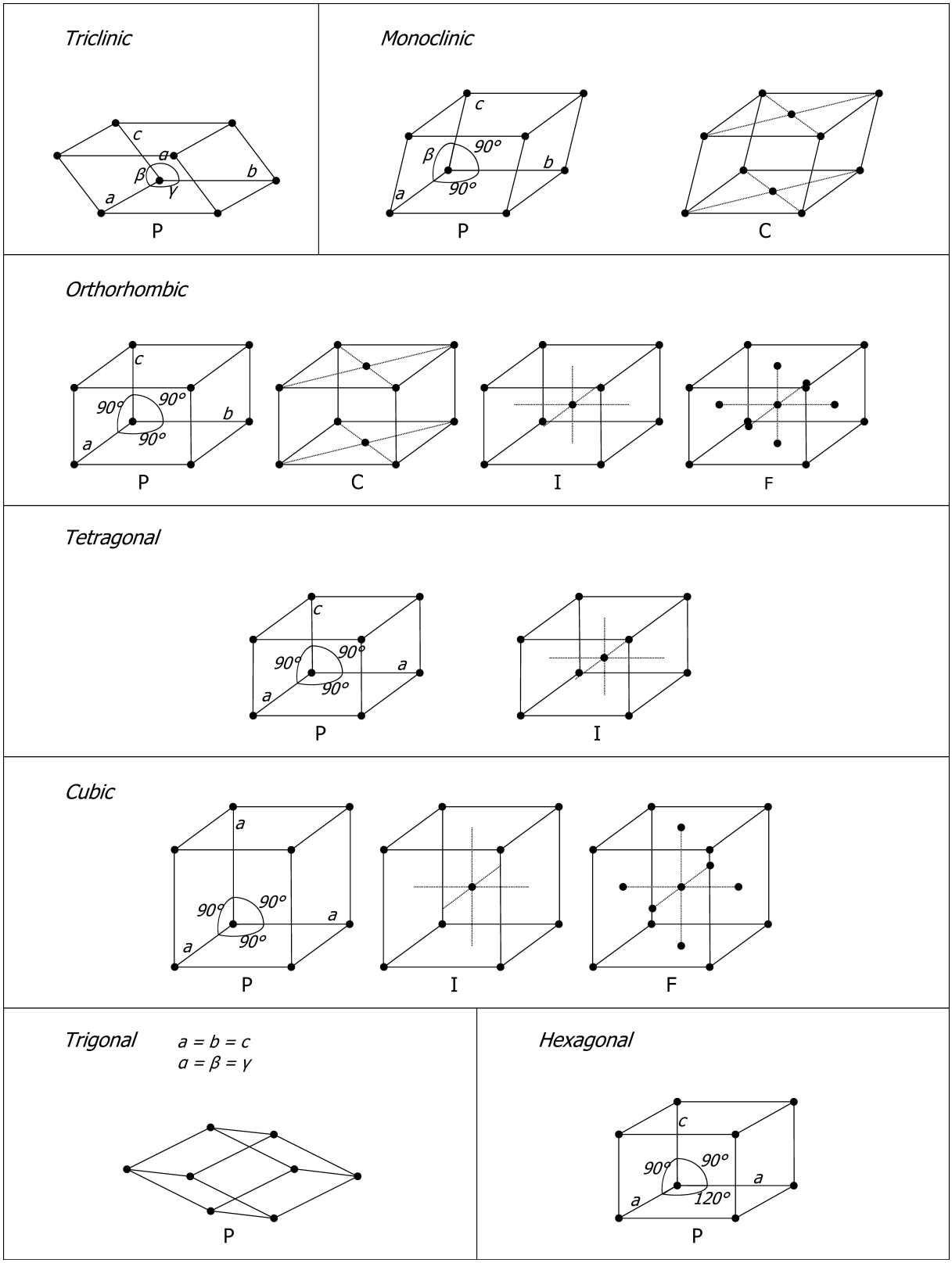


Figure 3.1: The 7 crystal lattice types with the 14 possible unit cell arrangements (Bravais lattices)

the $x$, $y$ and $z$ directions must be specified in that very order in addition to the centering type. For tetragonal systems, the symmetry of the $z$ axis is specified, then the symmetry along the $x$ axis is given, and lastly the symmetry of the $[1, 1, 0]$ direction is specified. In trigonal and hexagonal systems, the symmetry of the $z$, $x$ and $[1, \bar{1}, 0]$ axes is specified in that order. For the cubic systems, the symmetries of the $x$, $[1, 1, 1]$ and $[1, 1, 0]$ axes are specified in that order. It is so, that no less or no more directions are needed in each case for a complete description of the crystal symmetry[18].

### 3.1.2 Scattering from crystals

#### Bragg's law

Electromagnetic radiation, neutrons or electrons that hit a crystal will interact with the atoms in a way which depends on the atomic arrangement, i.e. the crystal system, centering and symmetry. Electromagnetic radiation and electrons interact with the electron density of the atoms, whereas neutrons pass through the atomic orbitals and interact with the nucleus.

If a ray with wavelength $\lambda$ enters the crystal with an angle $\theta$ with some crystal plane (h k l) in direct space, the ray will be partially scattered such that the outgoing ray has the same angle with the plane (see figure 3.2). This happens for all other parallel crystal planes as well. The distance between the planes is $d_{hkl}$. Constructive interference of two parallel scattered rays will occur if the difference in traveled path equals an integer number of wavelengths, that is, if the following condition is fulfilled:

$$2d_{hkl}sin\theta = n\lambda \qquad n \in N \tag{3.1}$$

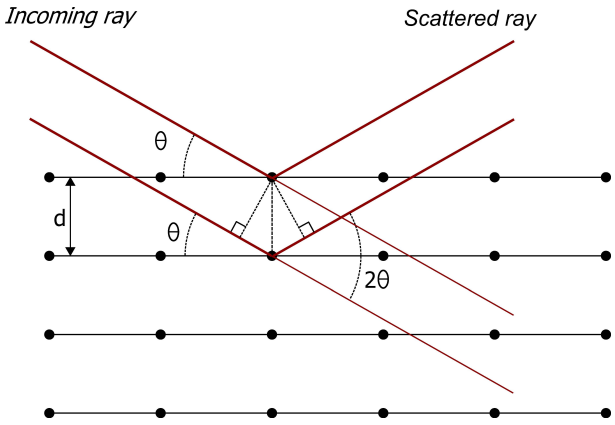


Figure 3.2: The diffraction condition illustrated in direct space (Bragg's law).

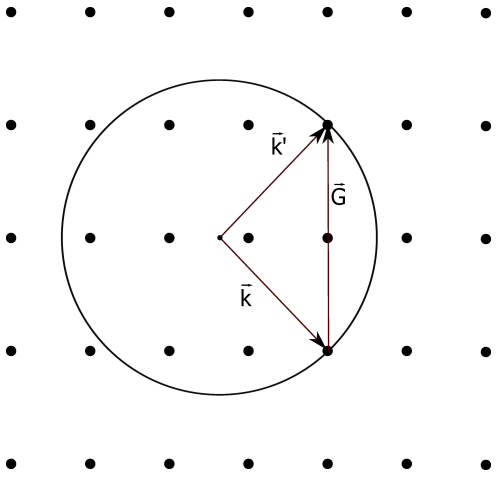


Figure 3.3: The diffraction condition illustrated in reciprocal space (The Ewald construction).

This is called Bragg's law. A Bragg reflection can consequently be assigned to a specific crystal plane. If the size of the unit cell is increased (bigger distance between crystal planes), for example because of thermal expansion, this will result in smaller scattering angles for all reflections, and vice versa ($d \propto 1/sin\theta$).

**Diffraction condition in reciprocal space**

Alternatively, one can also formulate the refraction condition in reciprocal space. The reciprocal space is spun by all wavevectors $\vec{G}$ such that the wave $e^{i\vec{G}\cdot\vec{r}}$ has the same periodicity as the direct lattice. This is fulfilled if $\vec{G}\cdot\vec{R} = 2\pi$. Then, $\vec{G}$ is called a reciprocal lattice vector.

Let the unit cell vectors only in this subsection be defined as $\vec{a} = \vec{a}_1, \vec{b} = \vec{a}_2$ and $\vec{c} = \vec{a}_3$. If the so-called reciprocal unit cell vectors $\vec{b}_1, \vec{b}_2, \vec{b}_3$ are defined as

$$\vec{b}_1 = 2\pi\frac{\vec{a}_2 \times \vec{a}_3}{V_u} \qquad \vec{b}_2 = 2\pi\frac{\vec{a}_3 \times \vec{a}_1}{V_u} \qquad \vec{b}_3 = 2\pi\frac{\vec{a}_1 \times \vec{a}_2}{V_u} \tag{3.2}$$

where $V_u$ is the volume of the unit cell in direct space, they will fulfill the condition $\vec{a}_i \cdot \vec{b}_j = 2\pi\delta_{ij}$, $i, j \in [1, 2, 3]$, and we can formulate the reciprocal lattice vector as

$$\vec{G} = h\vec{b}_1 + k\vec{b}_2 + l\vec{b}_3 \tag{3.3}$$

where $h$, $k$ and $l$ are integers. The reciprocal unit cell vectors are the Fourier transform of the direct lattice unit cell vectors.

Let us now assume that a ray with wavevector $\vec{k}$ hits the crystal, is elastically scattered, and leaves the crystal with wavevector $\vec{k}'$. The angle between the wavevectors is $\theta$. This means that $\left|\vec{k}\right| = \left|\vec{k}'\right| = 2\pi/\lambda$, and we define the momentum transfer vector as

$$\Delta\vec{k} = \vec{k}' - \vec{k} \tag{3.4}$$

$\Delta\vec{k}$ is sometimes denoted $\vec{q}$. It follows from simple geometry that the length of this vector is

$$\Delta k = \frac{4\pi}{\lambda} sin\theta \tag{3.5}$$

Let now two incoming waves with wavevector $\vec{k}$ scatter at two identical lattice points connected with the vector $\vec{R}$. Both of the scattered waves have wavevector $\vec{k}'$. The difference in traveled path between the two rays will be the difference between the projection of $\vec{R}$ along $\vec{k}$ and the projection of $\vec{R}$ along $\vec{k}'$ (eq. 3.6). Constructive interference occurs if this equals an integer number of wavelengths:

$$\vec{R}\cdot\frac{\vec{k}'}{k} - \vec{R}\cdot\frac{\vec{k}}{k} = n\lambda \qquad n \in Z \tag{3.6}$$

With $k = \frac{2\pi}{\lambda}$ and $\Delta\vec{k} = \vec{k}' - \vec{k}$ inserted, this condition can be expressed as:

$$e^{i\Delta\vec{k}\vec{R}} = 1 \tag{3.7}$$

We recognize $\Delta\vec{k}$ as a reciprocal lattice vector:

$$\Delta\vec{k} = \vec{G} \tag{3.8}$$

This is the generalized diffraction condition which is called the Laue interference condition. It is equivalent to Bragg's law (equation 3.1) and is nicely illustrated with the Ewald construction (figure 3.3). The wavevector $\vec{k}$ of the incoming ray is drawn such that the tip ends at a reciprocal lattice point. A circle (a surface in three dimensions) with

radius $k$ is then drawn around the start of the vector. The points on this surface will then define all $\vec{k}$ such that the diffraction condition is met[17][20].

It is readily seen from equation 3.8 and 3.3 that the momentum transfer $\Delta k$ is solely a function of the atomic arrangement and the Miller indices for a specific reflection. Therefore, when diffraction patterns produced with radiation of different wavelengths are compared, a natural choice of abscisse dimension will be $\Delta k$.

**The structure factor**

The intensity of a so-called Bragg peak with indices (h k l) (a reflection from the (h k l) plane), is proportional (more accurately related in equation 4.5) to the square of the structure factor

$$I_{hkl} = |F_{hkl}|^2 \tag{3.9}$$

which is defined as

$$F_{hkl} = \sum_{j=1}^{N} f_j e^{2\pi i(hx_j+ky_j+lz_j)} e^{-\frac{1}{2}\Delta k^2 \left\langle u^2 \right\rangle_j} \tag{3.10}$$

The sum goes over all atoms $j = 1...N$ in the unit cell which has the positions ($x_j$, $y_j$, $z_j$). In that sense, the structure factor and the resulting intensity is a Fourier transform of the atomic arrangement. Only the squared length of the imaginary $F_{hkl}$ is measured, and thereby valuable information about the atomic positions is lost. This is called the *phase problem* in crystallography.

The second exponential function is called the Debye-Waller factor. It contains $\langle u^2 \rangle_j$, which is the isotropic displacement of atom $j$ around its mean position due to thermal excitations. The dimension $1/2 \cdot [wavevector] \cdot [displacement]^2$ is recognized as the energy of a harmonic oscillator.

Lastly, $f_j$, called the atomic scattering factor, is the Fourier transform of the electron density of atom $j$. For electromagnetic radiation, $f_j$ is proportional to the atomic number $Z$, and the Bragg peak intensity from light elements will therefore be much lower than from heavy elements. For powder neutron diffraction (PND), the peak intensity does not depend on the electron density and $f_j$ is constant. $|F_{hkl}|$ decreases with increasing scattering angle because $\Delta\vec{k}$ enters in the exponent of the Debye-Waller factor.

When the atomic positions of a specific symmetry (FCC, BCC *etc.*) is inserted for $x_j$, $y_j$ and $z_j$, will different hkl integers lead to exponents that are integers of $\pi i$, and consequently, $e^{2\pi i(hx_j+ky_j+lz_j)}$ may be $-1$ or 1, and for certain combinations of $h$, $k$ and $l$, $|F_{hkl}|$ may be zero. A certain set of extinction rules applies, depending on the centering type and elements with translational symmetry. The diffraction pattern will be characterized as a cause of this.

### 3.1.3 Indexing of crystal planes

There are infinitely many ways to divide a lattice into parallel equidistant planes, such that every lattice point is part of a plane. If $h, k$ and $l$ have no common factor, that is, $\vec{G}$ is the shortest reciprocal lattice vector, the equation

$$\vec{G} \cdot \vec{R} = n\frac{2\pi}{\left|\vec{G}\right|} \tag{3.11}$$

describes a plane normal to $\vec{G}$ with interplanar distance

$$d = \frac{2\pi}{\left|\vec{G}\right|} \tag{3.12}$$

If this expression is set into Bragg' law (eq. 3.1), we get the following relation:

$$4\pi sin\theta = n\lambda \left|\vec{G}\right| \tag{3.13}$$

In the general triclinic case, the length square of $\vec{G}$ is $\left|\vec{G}\right|^2 = h^2b_1^2 + k^2b_2^2 + l^2b_3^2 + 2hk\vec{b_1} \cdot \vec{b_2} + 2kl\vec{b_2} \cdot \vec{b_3} + 2hl\vec{b_1} \cdot \vec{b_3}$. The reciprocal lattice vectors $\vec{b_1}$, $\vec{b_2}$ and $\vec{b_3}$ have to be calculated from their definitions (eq. 3.2). The procedure for identification and indexing of crystal planes of an unknown crystal now starts with the following: A crystal lattice type and unit cell parameters are postulated and $\left|\vec{G}\right|$ is calculated for non-extinct planes. Then, $\theta$ or $2\theta$ is calculated from equation (3.13) and listed. These computed angles for Bragg peak positions are then compared with the measured ones. With the help of clever algorithms are all possible unit cells within a given parameter range investigated. All the lattice types may be investigated with this procedure[21]. However, it is clear that the cost of the calculation will strongly depend on the number of unrestricted parameters, ranging from six in the triclinic case to one in the cubic case. For a cubic lattice, to take an example, the lattice constant $a$ can be calculated from the measured $\theta$ values in accordance with a trial set of extinction rules which has to be chosen (depending on the centering type - $BCC$, $FCC$ or $SC$). For the right choice of centering, all values for $a$ should be the same.

If contaminating crystalline phases are suspected to be present in the material, one can allow some observed peaks to be unindexed. One should, though, thoroughly ensure that the selected peaks belong to the same phase or not. Here, *in-situ* PXD is a valuable tool. Auto-indexing programs also allow some calculated peaks to remained unexplained by the observed pattern.

## 3.2 Physical and chemical properties of borohydrides

We will here introduce a few theoretical and experimental principles regarding the stability and thermodynamics of borohydrides, as well as the techniques that are used to improve these properties. We will exemplify with the promising lithium borohydride, which is used as a basis the experiments. This will give the opportunity to summarize its crystal structure and sorption properties and previous works that have aimed at improving the thermodynamics of this compound.

### 3.2.1 Thermodynamics of sorption reactions

Consider a hydrogen containing compound that decomposes with a certain enthalpy $\Delta H < 0$ into hydrogen gas and one or more residue products:

$$\mathrm{AH_n}(s) \rightleftharpoons \mathrm{A}(s) + \frac{n}{2}\mathrm{H_2}(g) \qquad n = 1, 2, 3... \tag{3.14}$$

Negative values of the Gibb's free energy of the reaction $\Delta G$ will make this reaction proceed to the right, and positive values to the left. The fact that this reaction can go

in both directions at a given temperature $T$ just by slightly altering the gas pressure $p$, makes it possible to talk about an *equilibrium pressure* $p_e$, at which $\Delta G$ of the reaction is zero. If the gas is considered to be an ideal gas, it can be shown[8] that

$$\Delta G = \Delta G^0 + RTln(Q) \tag{3.15}$$

where $G^0$ is the free energy of the reaction at 25°C and $p_a = 1$ bar, $Q$ is the reaction quotient (from chemistry) and $R$ is the universal gas constant. In this case, where only one of the products is a gas, $Q$ is simply the pressure of this gas divided by the atmospheric pressure. Setting $\Delta G = 0$ yields

$$\Delta G^0 + RTln(\frac{p_e}{p_a}) = 0 \qquad \rightarrow \qquad \frac{p_e}{p_a} = e^{-\frac{\Delta G^0}{RT}} \tag{3.16}$$

Since $\Delta G^0 = \Delta H^0 - T\Delta S^0$, where $\Delta H^0$ is the standard reaction enthalpy and $\Delta S^0$ the standard reaction entropy, we can rewrite equation 3.16 such that the equilibrium pressure is expressed as a function of temperature (standard condition notation is omitted from now on):

$$ln(\frac{p_e}{p_a}) = \frac{-\Delta H}{R}\frac{1}{T} + \frac{\Delta S}{R} \tag{3.17}$$

This is often referred to as the van't Hoff equation or the Arrhenius equation, although the original van't Hoff equation is written slightly differently[8]. The change in entropy is around 130 $\frac{\text{J}}{\text{Kmol}}$ for all metal-hydrogen systems, because it largely corresponds to the entropy of the $H_2$ gas[1]. By measuring the equilibrium pressure at different temperatures, the reaction enthalpy can be calculated from equation 3.17. If the enthalpy is known, the entropy can similarly be calculated.

It follows that the decomposition temperature at atmospheric pressure is

$$T(1 \text{ bar}) = \frac{\Delta H}{\Delta S} \tag{3.18}$$

Ideally, one can assume that reaction 3.14 proceeds completely just when the temperature and pressure requirements are fulfilled. One has then a "plateau pressure", at which all the hydrogen gas is absorbed or desorbed. Plotting the applied pressure of the surrounding gas against the molar fraction of the hydrogen content $c_H = H/M$ ($H$ and $M$ are the moles of absorbed hydrogen and moles of the host, respectively) gives a so-called Pressure-Composition-Temperature (pcT) curve where the length, height and flatness of the plateau pressure gives information about the amount of uptaken hydrogen, required equilibrium pressure and practical usability respectively. To exemplify, pcT-curves and corresponding van't Hoff plot of $LaNi_5$ is shown in figure 3.4. Experiments that implement these features will be discussed in section 4.2.

For metal hydrides, the metal dissolves some hydrogen as a solid solution while the pressure is below $p_e$, known as the $\alpha$-phase. When interactions between the hydrogen atoms in the hydride becomes important, the nucleation and growth of the hydride phase, the $\beta$-phase, begins. As long as the two phases coexist, the equilibrium pressure is almost constant.

[1]It is thereby assumed that all the hydrogen atoms in the hydride are fixed in a lattice without distortions

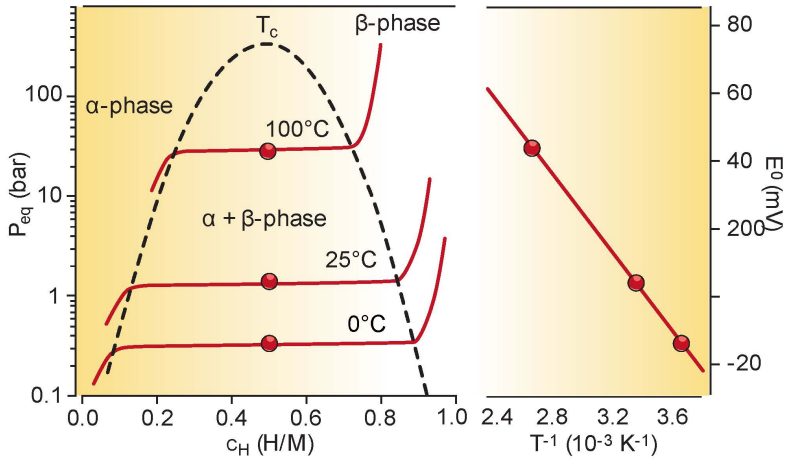


Figure 3.4: Three isothermal pressure-composition-temperature (pcT) curves (left) and a van't Hoff plot (right) of $LaNi_5$ at three isotherms. (From Nature 2001, vol. 44, page 356[9])

Especially among the metal hydrides we find materials with very flat plateau pressures and low $p_e$. This is very advantageous in terms of hydrogen storage, because the reaction can very easily be controlled with technical equipment. However, for the complex hydrides, this plateau is usually not very flat, i.e. the equilibrium pressure increases with the hydrogen content. Equivalently, an endothermic decomposition reaction with a given $\Delta H$ will release hydrogen over a relatively wide temperature range. It has been speculated that this is caused by the directional nature of the covalent bonds in the $[BH_4]^-$ tetrahedra, which gives high activation energies for atomic diffusion[13]. Consequently, the grain surface will react first and the bulk much later. Very slow kinetics will lead to an apparent hysteresis in the pcT curve: $\Delta G$ in equation 3.16 is not longer zero when the process is observed to take place, and the observed pressure under absorption is significantly higher than that of desorption. To overcome this problem, suitable catalysts like $TiCl_3$ or $ZrCl_4$ which intends to activate the material may have favorable effects[13][22]. Since slow atomic diffusion is in principle independent of $\Delta H$, stabilization of the reaction products does not necessarily increase the reaction kinetics.

The decomposition of borohydrides often proceeds via several intermediate steps, which produces one plateau pressure at each intermediate reaction. In a storage system, the pressure then have to be altered if the whole hydrogen capacity is to be accessed. Also, many of the complex hydrides tend to have more negative enthalpies of formation $\Delta H_f$ than the metal hydrides, which makes them more stable[3][9]. Techniques to overcome these problems will be discussed in the following sections.

### 3.2.2 Tuning of thermodynamical properties and improving reaction kinetics

All techniques that are used to improve the sorption properties of complex hydrides can be divided in two groups: One type of methods aims at the lowering of the enthalpy of the decomposition reaction. This includes mainly preparation of reactive hydride composites and synthesis of mixed-metal or anion-substituted borohydrides. The other set of techniques attacks the problem of slow sorption kinetics. The most used methods here are addition of small amounts of a catalyst and nanostructuring of the host.

#### Stabilizing the reaction products

The decomposition temperature at atmospheric pressure will be directly affected by a lower reaction enthalpy, according to equation 3.18. This can also be seen in figure 3.4: By lowering the decomposition enthalpy (the slope in the van't Hoff plot), $1/T$ will be higher for a given equilibrium pressure, and consequently, the decomposition temperature will be lowered. Much effort has therefore been done in order to assess the underlying principles that affect the reaction enthalpy. One approach is the following: A reactive compound B is added to the main host $AH_2$ that react during decomposition and form a different end product $AB_x$ that has a lower $\Delta H_f$ than the original product A:

$$AH_2 + xB \rightleftharpoons AB_x + H_2 \tag{3.19}$$

In this way the reaction enthalpy is lowered. This is illustrated by the enthalpy diagram in figure 3.5.

The maybe most successful application of this technique is the addition of binary hydrides to lithium borohydride, exemplified in section 3.2.3. In this way, the additive is a hydride itself and may contribute to the storage capacity.

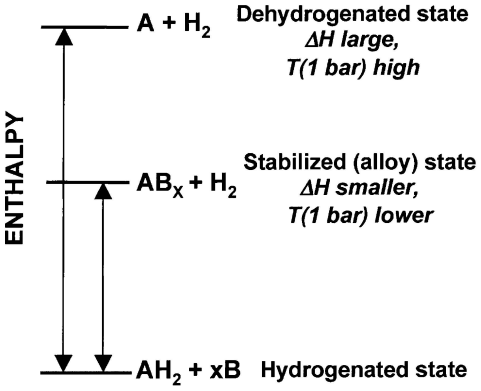


Figure 3.5: Enthalpy diagram showing how the enthalpy of decomposition is lowered by addition of a reactive catalyst. (From J. Alloys Compd., 2007, vol. 446-447, page 410)

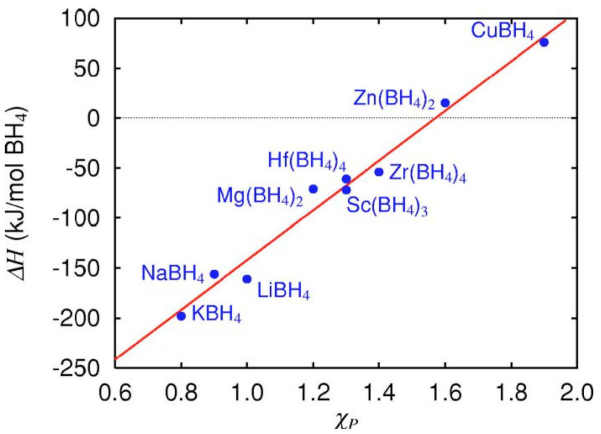


Figure 3.6: Correlation between enthalpy of formation $\Delta H_f$ and Pauling electronegativity $\chi_P$. (From Phys. Rev. B, 2006, vol. 74, page 045126-6)

### Modify the storage material

A second approach is to change the chemistry of the original host and thereby destabilize it. This can be done by substituting of the $[BH_4]^-$ tetrahedra by halide anions and/or substitution/replacement of the metal cations. As mentioned in the introduction, it was discovered by Nakamori et al.[11] and later verified by others that the enthalpy of formation from the elements $\Delta H_f$ per mole of $[BH_4]^-$ is proportional to the Pauling electronegativity $\chi_P$ of the metal cation, in the following way:

$$\Delta H_f = 248.7\chi_P - 390.8 \qquad [\Delta H_f] = \text{kJ/mol BH}_4 \tag{3.20}$$

This is shown for the probed monometallic borohydrides $M(BH_4)_n$ (M = K, Na, Li, Mg, Sc, Hf, Zr, Zn, Cu) in figure 3.6. The interpolated (equation 3.20) line is the result of the least-squares regression. The temperature of decomposition at 1 bar and thereby also the enthalpy of decomposition (according to equation 3.18) was also experimentally observed to correlate linearly with with $\chi_P$, with the highest decomposition temperature for the metal cation of lowest electronegativity[11].

The linear relationship between the cation electronegativity and the stability may be explained by the bonding of the $[BH_4]^-$ group to the metal by bridging hydrogen atoms. As mentioned, hydrogen is bound covalently to boron, owing to the charge density of the latter. By bridging boron and the cation through hydrogen, the molecule becomes electron deficient, i.e. it possess fewer than two electrons per binding orbital. Consequently, the difference in electronegativity between the metal and the boron atom will continuously alter the bridging and thereby influence the stability of the $[BH_4]^-$ group. This is seen by the fact that the alkali alanates are less stable than the alkali borohydrides, because aluminum has lower electronegativity than boron[23]. Moreover, the bending and stretching vibrational modes of the hydrogen atoms in the alkali borohydrides are found to correlate with the cation electronegativity as well[24].

Diborane ($B_2H_6$) is also regarded as electron-deficient, and if the cation electronegativity is too large, the hydrogen will be so strongly shifted towards the cation M that presumably the binary hydride MH will form and thereby release $BH_3$, which thereafter combines pairwise into diborane[23].

### Synthesize mixed-cation and mixed-anion borohydrides

The newly gained knowledge of the stability of complex hydrides has inspired researchers to try to synthesize new so-called mixed-cation (mixed-metal) or mixed-anion borohydrides that have a lower enthalpy of formation than the conventional lightweight hydrides.

Starting with an alkali borohydride $MBH_4$, the goal is to synthesize for example $MM'(BH_4)_m$, where M′ is a metal of higher electronegativity than M, and the integer $m$ depends on the amount and oxidation number of M′, since the net charge have to be zero. $\Delta H_f$ will now depend on the averaged $\chi_P$ of M and M′ according to equation 3.20. The stability in terms of binding energy $E_b$ of hundreds of these theoretical compounds has been estimated by Hummelshøj et al. with density functional theory (DFT) (approximate solution of the Schrödinger equation), and a list of promising candidates within the desired range of $\Delta H_f$ and $E_b < 0$ was laid forth[25].

One efficient way to make new mixed-metal borohydrides is to ball mill an alkali borohydride together with a halide of the desired substitution metal. As opposed to the addition of a catalyst into the hydride, which involves only small amounts of additives, the

technique of ball-milling a complex hydride and a halide in a given molar ratio is based on a so-called metathesis reaction and aims at the formation of a new compound, where the added cations, for example the rare earth metals, substitute the original counter ions in the complex hydride (reaction 3.21).

$$m\mathrm{MBH_4} + \mathrm{M'Cl_n} \rightarrow \mathrm{M_{m-n}M'(BH_4)_m} + n\mathrm{MCl} \tag{3.21}$$

In this mechanochemical reaction, a new mixed-cation borohydride is then hopefully formed after sufficient milling time. For example, the ball milling of $4\mathrm{LiBH_4}$ with $\mathrm{ScCl_3}$ leads to the formation of $\mathrm{LiSc(BH_4)_4}$[26]. The general drawback of the mixed-metal borohydrides is that the MCl byproduct (here LiCl) may be very difficult to remove from the composite and lowers the storage capacity.

Also, similar tuning of the thermodynamic properties can be achieved by substituting the hydrogen atoms or the $[\mathrm{BH_4}]^-$ tetrahedra with halide ions, principally $\mathrm{F^-}$ and $\mathrm{Cl^-}$ respectively. But as we will see in the next section, this effect is unwanted in the case of $\mathrm{LiBH_4}$ since it stabilizes the high temperature phase rather than destabilizing it. It may also occur unintended during ball-milling when halides are present in the composite.

While non-stoichiometric substitution often takes place without the crystal structure being changed, mixed-cation or mixed-anion borohydrides usually assembles completely different structures than the starting hydrides, and they should be examined by means of X-ray or neutron diffraction in order to determine the crystal structure.

Around 30 mixed-cation or mixed-anion borohydrides have been reported so far. Some of these, including $\mathrm{LiCe(BH_4)_3Cl}$ which will be discussed below, contains rare earth ions as additional counter cations. In $\mathrm{LiCe(BH_4)_3Cl}$, the lithium ions are found to have very high conductivity, making this material also attractive as a new solid electrolyte in batteries[12].

However, after four years of extensive research, it has been clear that many of mixed-cation borohydrides proposed by Hummelshøy et al. were not possible to synthesize or were not stable at ambient conditions. This fact reflects the difficulties related to an *a priori* determination of the stability to unknown compounds based on quantum mechanical calculations.

### Addition of catalysts

In 1997, Bogdanovic and Schwickardi[27] added selected titanium-based catalysts to the alanate $\mathrm{NaAlH_4}$ which accelerated the desorption and absorption reactions significantly. The reversibility capacity was greatly improved in relation to pure $\mathrm{NaAlH_4}$. Such a system of $\mathrm{NaAlH_4}$ with $\mathrm{TiCl_3}$ additives can be dehydrogenated and rehydrogenated at least 100 times without significant property changes. The amount of hydrogen exchanged constitutes in this case 3.5 wt% (weight-percent) of the storage material. The rehydrogenation takes place at 125°C and 81-90 bar[3]. There has been build functioning storage systems based on $\mathrm{NaAlH_4}$, but the hydrogen content in this storage system is still very limited due to the relatively heavy sodium alanate.

### Reducing grain size and nanoconfinement

Lastly, reduction of grain size and/or confinement in nanoporous scaffolds is a way to ease the atomic diffusion in the complex hydride and thereby improving reaction kinetics[28]. Actually, by reducing the particle-size to the nm scale, the thermodynamics can also be

altered, because surface effects dominate over bulk effects. Details are provided below with $LiBH_4$ as a host example.

### 3.2.3 Lithium borohydride

Lithium borohydride has been known for many decades, and has been used primarily as a reducing agent in chemistry. The decomposition reaction of $LiBH_4$ into the elements is endothermic, and it is therefore theoretically possible to reverse this reaction and form $LiBH_4$ from the elements by exposing it to the required pressure. This has been verified experimentally, see below.

#### Crystal structure

At room temperature, lithium borohydride crystallizes in the orthorhombic space group *Pnma*. At approximately 107°C it undergoes an endothermic phase transition into a hexagonal structure with space group $P6_3mc$, where the $[BH_4]^-$ groups are reoriented along the *c*-axis. At around 280°C, $hex-LiBH_4$ is reported to melt, and the corresponding melting enthalpy is easily detected by calorimetry. A partial decomposition and hydrogen release (approx. 50%) occurs at above 450°C. At 680°C there is an additional hydrogen release, such that a total of 13.8 wt% has been released up to this point[6].

The crystal structure of $LiBH_4$ at room temperature was described in detail by Soulie et al. in 2002[29] (table 3.2). Synchrotron radiation powder diffraction data were used in the refinement. The same year, Züttel et al.[30] started out from the same atomic arrangement but refined them with a SR-PXD pattern from a new batch of orthorhombic $LiBH_4$ which featured remarkably different relative intensities. This resulted in lattice constants that differed in the third digit. In 2008, a new study by Kang et al.[31] presented another set of lattice parameters, which were different in the second digit (table 3.2). All these reports are based on $LiBH_4$ with purity 95%, and the experiments were performed in room temperature and at atmospheric pressure. Impurities can be contained as substituted atoms in the crystal lattice, which will alter the reflections from $LiBH_4$, or they can be impurity phases which give additional reflections. Both Züttel et al. and Soulie et al. conclude that the $[BH_4]^-$ tetrahedra are strongly distorted with respect to bond lengths, and it is likely that the coordinates of the hydrogen atoms can be changed by pressure, strain or temperature changes. Moreover, $LiBH_4$ is a very weak scatterer, and the relative intensities can be hard to quantify with high precision if there are impurity phases present in the sample.

The lattice parameters found by Soulie et al. and Kang et al. are presented in table 3.2. The atomic positions are not shown, but can be found in reference [29].

The difference in these values underline that one has to treat published lattice parameters of low-purity samples with caution. For this reason, the lithium borohydride batch used in this work has been thoroughly investigated by means of SR-PXD and calorimetric analysis.

#### Anion substitution

Structural and thermodynamic effects of chloride substitution into both phases of $LiBH_4$ has been investigated by Matsuo et al.[33] and Arnbjerg et al.[32]. They both conclude that chlorine substitution yields smaller unit cells, in agreement with the different ionic

Table 3.2: The high- and low temperature phases of $LiBH_4$ compared with anion-substituted $LiBH_4$.

| Phase | Space group | $a$(Å) | $b$(Å) | $c$(Å) | Ref. |
|---|---|---|---|---|---|
| $Ortho - LiBH_4$ | $Pnma$ | 7.17858(4) | 4.43686(2) | 6.80321(4) | [29] |
| $Ortho - LiBH_4$ | $Pnma$ | 7.141(5) | 4.431(3) | 6.748(4) | [31] |
| $Ortho - Li(BH_4)_{0.70}Cl_{0.30}$ | $Pnma$ | 7.001(1) | 4.3236(9) | 6.808(1) | [32] |
| $Hex - LiBH_4$ | $P6_3mc$ | 4.27631(5) | | 6.94844(4) | [29] |
| $Hex - LiBH_4$ | $P6_3mc$ | 4.3228(10) | | 7.0368(10) | [31] |
| $Hex - Li(BH_4)_{0.58}Cl_{0.42}$ | $P6_3mc$ | 4.2139(3) | | 6.7691(7) | [32] |

radii of the anions ($R_{ion}(Cl^-) = 1.81$ Å[34], $R_{ion}([BH_4]^-) = 2.05$ Å[32]). The orthorhombic unit cell contracts anisotropically along the $a$-axis and the hexagonal unit cell contracts isotropically. Different degrees of substitution were studied, and only the phases with maximum chlorine content are quoted here. The lattice parameters for both orthorhombic and hexagonal $Li(BH_4)_{1-x}Cl_x$ from Arnbjerg et al. are shown in table 3.2. Another important effect of chlorine substitution is that the stability of the hexagonal phase is increased. That is, the orthogonal to hexagonal transition occurs at a lower temperature (42°C instead of 102°C) and the melting occurs at a higher temperature (297°C instead of 280°C) at atmospheric pressure[32].

### Decomposition and rehydrogenation reactions

The decomposition and rehydrogenation properties of $LiBH_4$ have been investigated by several groups. At atmospheric pressure, $LiBH_4$ decomposes gradually into LiH and amorphous B (reaction 3.22) above its melting temperature (280°C). The equation shows only the overall decomposition reaction; hydrogen is believed to be released in several subsequent steps around $450-500$°C, similarly to the alanates[6]. However, these amorphous or molten intermediates have proved difficult to determine. There is some experimental evidence (X-ray and Raman spectroscopy) that the borohydride cluster $Li_2B_{12}H_{12}$ is formed as an intermediate[35]. Predicted decomposition temperature and enthalpy for reaction 3.22 is 410°C and $\Delta H = 67$ kJ/mol $H_2$, respectively[13]. The decomposition temperature at 1 bar is observed to be between $450 - 500$°C, and the enthalpy obtained from indirect stability measurements is 74 kJ/mol $H_2$[6] (reported values varies), which indicates slow reaction kinetics. According to reaction 3.18 is now the entropy of dehydrogenation 164 $\frac{J}{Kmol}$, significantly higher than the value for most metal hydrides (130 $\frac{J}{Kmol}$), which is hard to explain[23]. Orimo et al.[36] reported in 2004 that $LiBH_4$ can be decomposed under 10 bar of hydrogen at 600°C, and then completely rehydrogenated under 350 bar of hydrogen at the same temperature. Züttel et al. demonstrated that a pressure of 150 bar at 727°C also reverses this reaction[23].

$$LiBH_4(l) \rightarrow LiH + B + \frac{3}{2}H_2 \qquad \Delta H = 74 \text{ kJ/mol } H_2 \tag{3.22}$$

The enthalpy of formation at standard conditions of $LiBH_4$ is $\Delta H_f^0 = -194.15$ kJ/mol [23], and a temperature too high for practical applications (above 727°C) must be applied in order to decompose it into the elements. Even the decomposition temperature reaction 3.22 is too high if the heat is to be generated on-board a vehicle, and the above mentioned

extreme rehydrogenation conditions makes it clear that pure $LiBH_4$ is not suited as a energy storage material.

### Reactive additives: Magnesium and rare-earth hydrides

An example of successful improvements of $LiBH_4$ systems is the addition of $MgH_2$ to $LiBH_4$ in a molar ratio of 1:2.

$$2LiBH_4 + MgH_2 \rightarrow 2LiH + MgB_2 + 4H_2 \qquad \Delta H = 46 \text{ kJ/mol } H_2 \tag{3.23}$$

As explained in section 3.2.2, more stable end products will result in a lower enthalpy of decomposition. The enthalpy is now reduced to 46 kJ/mol $H_2$ by the formation of $MgB_2$. $T(1 \text{ bar})$ was calculated to be 170°C[13], however, this depends naturally on the calculated entropy, which is reported to be much larger (around 240 J/Kmol) than the expected value of 130 J/Kmol[23]. The origin of this discrepancy is unknown.

When it comes to the actual experiments performed on the $2LiBH_4 + MgH_2$ system, the lowest measured $T(1 \text{ bar})$ was 350°C, because even at this temperature, the reaction time was very long (100 h). In fact, the reaction proceeded in two steps with midpoints at 315 and 410°C, which were assigned to the decomposition of $MgH_2 \rightarrow Mg + H_2$ and the lithium borohydride decomposition, respectively. The reaction enthalpy was in fact slightly lowered, but the kinetics were not improved[13]. Different catalytic additives were tried, which lowered the decomposition temperatures 7-10°C. Incorporating the sample into a nanoporous RF-CA scaffold with pore diameter $D_{avg} = 21$ nm did also significantly improve the kinetics, and the two decomposition events were observed almost to coincide, resulting in a common weight loss of 4.8 wt% around 340°C[28].

The addition of $CaH_2$ has even smaller destabilizing effect, if any, although the decomposition here is a single-step reaction[37].

Rare earth hydrides form even better performing reactive hydride composites with $LiBH_4$ because of formation of stable rare-earth borides. It has been shown[22] that ball-milling of $LaH_{2+\delta}$ or $CeH_2$ with $LiBH_4$ in a molar ratio of 1:6 (reaction 3.24) lowers the calorimetric decomposition events from over 400°C to around 353°C and 363°C for $LaH_{2+\delta}$ and $CeH_2$ additives, respectively. The rare earth hydrides were in this case prepared by milling the rare earth chloride with lithium hydride i a ratio of 1:3, which produced lithium chloride as a by-product. No attempts were made to remove this compound from the mixture.

$$6LiBH_4 + CeH_2 + 3LiCl \rightarrow 6LiH + CeB_6 + 10H_2 + 3LiCl \tag{3.24}$$

Reaction 3.24 releases 5.0 wt% of hydrogen, and was reported[37] to be completely reversed when exposed to 10 bar hydrogen pressure at 400°C for 20 h, using $TiCl_3$ catalyst. Also rehydrogenation at 90 bar for 24 h without catalyst has been observed[38]. In the latter work, a beneficial effect of applying a moderate back pressure during the decomposition was demonstrated: The formation of the rare earth boride $CeB_6$ was promoted in favor of amorphous boron, and the decomposition enthalpy was thereby lowered. According to the van't Hoff equation (3.17), an effect of a higher equilibrium pressure should in theory simply increase the decomposition temperature for a given reaction. What might be the case, is that among several possible decomposition pathways, the one with the lowest decomposition enthalpy will be favored to a greater extent when the pressure high. The effects and mechanisms of back pressure are still disputed, an they will be explored to some extent in this work.

Nanostructuring the $LiBH_4 - CeH_2$ composite and adding a $ZrCl_4$ catalyst was shown to increase the reaction kinetics[22], leading to a total hydrogen release of 5.0 wt% (all available hydrogen from reaction 3.24) which slowly starts at 225°C and is finished at 350°C (decomposition event is 341°C) under a heating ramp of 5°C/min. The nanostructured composites with and without $ZrCl_4$ catalyst showed very good reversibility: After hydrogenation at 400°C and 60 bar, a second decomposition releasing 4.5 and 4.6 wt% started at 295 and 305°C for catalyzed and un-catalyzed systems, respectively. These results are very promising, and by removing LiCl from the composite, the theoretical storage capacity can be increased to 7.4 wt%.

### 3.2.4 Previously studied lithium-rare earth borohydrides

We will now give a necessary overview of previously synthesized and studied rare-earth borohydrides that were found in this work and will be needed in the later discussions.

#### Lithium-Cerium borohydride chloride: $LiCe(BH_4)_3Cl$

In 2009, Gennari and Esquivel published a paper[39] on what they claimed was a new cerium borohydride, $Ce(BH_4)_3$, with a cubic crystal system. The type of centering and space group were not reported. This compound had been produced by ball-milling $3LiBH_4 + CeCl_3$ for 6 hours. The experiment was repeated in 2011 by Frommen et al.[40] and in 2012 by Ley et al.[41] who produced the same diffraction patterns of the ball-milled samples, but this time another compound was proposed to explain the diffraction pattern, namely the mixed-cation and anion-substituted borohydride $LiCe(BH_4)_3Cl$, assembling a BCC structure with space group $I\bar{4}3m$. The formation of this compound was thoroughly proved by DFT calculations of the vibrational spectrum. The lattice parameters are given in table 3.3.

The compound decomposes via several steps. The first step occurs around 220°C, in which $CeH_2$, $H_2$ are formed. It was speculated if the intermediate species $Ce_2(B_{12}H_{12})_3$ was formed as well. Subsequently, at around 250°C, $Ce_2(B_{12}H_{12})_3$ and parts of $CeH_2$ react and form $CeB_6$ and hydrogen gas. Isothermal desorption showed that the first step had a very flat plateau pressure and was reached already at 200°C. Frommen et al. and Gennari and Esquivel reported a reversibility of 13% and 28% of the hydrogen content for 80 bar/340°C and 60 bar/350°C respectively. Further improvements are necessary to make this sample a possible storage material.

#### Lithium-Ytterbium borohydrides

A series of new ytterbium-lithium borohydrides produced by ball-milling and post-annealing of $LiBH_4 + YbCl_3$ in the molar ratios 3:1, 5:1 and 6:1 has recently been published by Olsen et al.[42]. They are listed in table 3.3. Since many of these compounds also are found in the samples studied in this work, they are overviewed in the following.

1 h milling of the $3LiBH_4 + YbCl_3$ composite produced a non-mixed ytterbium borohydride, $Yb(BH_4)_3$ in a primitive cubic modification (labeled $\beta$ in table 3.3) and the tetragonal mixed-cation and anion substituted $LiYb(BH_4)_{4-x}Cl_x$, the latter featuring a similar-looking diffraction pattern as $LiCe(BH_4)_3Cl$, only shifted towards higher scattering angles. The tetragonal phase also allows for a nonstoichiometric degree of substitution

[2]Result obtained for a deuterated sample

Table 3.3: Overview of recently reported ytterbium and cerium containing borohydrides. The first entry ($LiCe(BH_4)_3Cl$) is from reference [40], and the other from reference [42]. The atomic positions are found there as well.

| Phase | Lattice, space group | $x$ | $a$(Å) | $b$(Å) | $c$(Å) |
|---|---|---|---|---|---|
| $LiCe(BH_4)_3Cl$ | Cubic, $I\bar{4}3m$ | | 11.5916(1) | | |
| $LiYb(BH_4)_{4-x}Cl_x$ | Tetragonal, $P\bar{4}2c$ | 1 | 6.1729(3) | | 12.4155(10) |
| $\alpha - Yb(BH_4)_3$ | Cubic, $Pa\bar{3}$ | | 10.70715(15) | | |
| $\beta - Yb(BH_4)_3$ | Cubic, $Pm\bar{3}c$ | | 5.44223(3) | | |
| $Yb(BH_4)_{2-x}Cl_x$ | Orthorhombic, $Pbca$ | 0.3 | 13.20997(20) | 8.26829(12) | 7.44532(11) |
| $Yb(BH_4)_{2-x}Cl_x$ | Tetragonal, $P\bar{4}$ | $0.76^2$ | 6.74763(2) | | 4.28368(2) |

of the borohydride tetrahedra, although refinements gave $x = 1$, yielding the same stoichiometry as the cerium phase.

After longer milling, the $\beta$ modification of $Yb(BH_4)_3$ disappeared and another primitive cubic modification of the same compound arose, labeled $\alpha$. After 6 h of milling of the 3:1 composite only $\alpha - Yb(BH_4)_3$ and small amounts of $LiYb(BH_4)_{4-x}Cl_x$ were present. However, milling in a ratio of 5:1 produced exclusively $LiYb(BH_4)_{4-x}Cl_x$. This phase is then expected to be the major component in the 6:1 sample studied in this work.

Upon annealing at 100°C of a 6:1 composite the compound $Yb(BH_4)_{2-x}Cl_x$ was formed, assembling an orthorhombic symmetry with space group $Pbca$. The degree of substitution was found to be $x = 0.3$. At about 170°C, this compound was reported to transform into a primitive tetragonal phase with space group $P\bar{4}$.

DSC-TGA measurements on the 3:1 sample showed two endothermic events which both were related to mass losses: An event at $105 - 145$°C released 3.6 wt% of both hydrogen and diborane, which was attributed to the decomposition of $Yb(BH_4)_3$ into $Yb(BH_4)_{2-x}Cl_x$, $B_2H_6$ and $H_2$. The second event at $310 - 345$°C was accompanied by a weight loss of 1.2 wt%, corresponding to a decomposition of $Yb(BH_4)_{2-x}Cl_x$ into $YbH_{2+\delta}$. The cycling properties of these borohydrides were not investigated.

### Reversibility enhancement and destabilization of $LiBH_4$ by *in-situ* formation of rare earth hydrides

As mentioned, Gennari et al.[43] have claimed that milling of $6LiBH_4 + LnCl_3$ (for Ln = Ce, Gd) will lead to the following reactions:

$$6LiBH_4 + CeCl3 \rightarrow Ce(BH_4)_3 + 3LiCl + 3LiBH_4 \tag{3.25}$$

Prolonged milling of these products with lithium hydride would furthermore lead to *in-situ* formation of $CeH_2$, which together with $LiBH_4$ constitutes the wanted reactive hydride composite.

$$Ce(BH_4)_3 + 3LiCl + 3LiBH_4 + 3LiH \rightarrow 3LiCl + 6LiBH_4 + CeH_{2+\delta} + \frac{1-\delta}{2}H_2 \tag{3.26}$$

According to Frommen[40] and Ley[41] is the product of reaction 3.25 not $Ce(BH_4)_3$, but $LiCe(BH_4)_3Cl$. This does not necessarily imply that reaction 3.26 gives another product: When $LiCe(BH_4)_3Cl$ reacts with LiH to form $LiBH_4$ and $CeH_2$, the excess lithium and chlorine atoms may rejoin and form LiCl (see equation 3.28). Another possibility is that parts of the produced $LiBH_4$ are being substituted by chlorine ions. The product of equation 3.28 is essentially the same as the left side of equation 3.24, and the same theoretical weight loss of around 5 wt% is expected (depending of course on the element Ln).

$$6LiBH_4 + LnCl_3 \rightarrow LiLn(BH_4)_3Cl + 2LiCl + 3LiBH_4 \tag{3.27}$$

$$LiLn(BH_4)_3Cl + 2LiCl + 3LiBH_4 + 3LiH \rightarrow 3LiCl + 6LiBH_4 + LnH_{2+\delta} + \frac{1-\delta}{2}H_2 \tag{3.28}$$

Since only 6:1 mixtures will be considered in this work, trivalent borohydrides of the type $Ln(BH_4)_3$ are not expected to form, referring to the results obtained by Olsen discussed above. To determine the amount of $LiBH_4$ before and after milling will be one important way to determine if reaction 3.28 has proceeded.

The theoretical hydrogen content was claimed to be 5.6 wt%. The decomposed composite was hydrogenated at 60 bar and 400°C for 2 h, before it was decomposed again. The decompositions were performed both under vacuum and 5 bar back pressure, and the amount of gas released are shown in table 3.4.

Table 3.4: Reported hydrogen release from the $6LiBH_4 + 3LiCl + CeH_{2+\delta}$[43]

| | First dehydriding (wt%) | Second dehydriding (wt%) |
|---|---|---|
| Vacuum | 5.1 | 4.0 |
| 5 bar back pressure | 5.4 | 4.4 |

Gennari et al. concludes from this that back pressure increases both the amount of hydrogen desorbed and the reversibility. It should be noted, however, that their non-isothermal desorption curves show clearly that back pressure slows down reaction kinetics and increases the decomposition temperature by $40 - 50$°C. Lastly, it should be stressed that the decomposition of the products of reaction 3.25 is observed to proceed in a two-step reaction, with $CeH_2$ as an intermediate by-product, whereas the decomposition pathway of the products of reaction 3.26 is single-step.

The rare earth hydride - lithium borohydrides systems show apparently promising hydrogen storage properties, with a reversible hydrogen content of around 4.5 wt% after the second cycle, which can theoretically be increased to above 7 wt% if LiCl is removed. The reaction kinetics is also remarkably enhanced in respect to $LiBH_4 - MgH_2$ systems, especially when the powder is nanoconfined and/or catalyzed. The rehydrogenation must still be performed at $350 - 400$°C, but taking into account that the absorption reaction is exothermic (around 45 kJ/mol $H_2$ for the $LiBH_4 - CeH_2$ composite), a vast amount of heat will be generated during absorption for an upscaled system, and the challenge will rather be to remove this heat. The filling pressure can be provided by the gas loading facility. A slight problem might be the gas release during milling (equation 3.26), and this is to be addressed in this work. What still remains a challenge is the too high desorption temperature and even stronger cycling performance.

It is clear that the necessity of reactive additives and catalysts lowers the storage capacity dramatically from the initial 13.4 wt% released from pure $LiBH_4$. Furthermore,

the system capacity will be much lower than the composite capacity. This together makes other, heavier base borohydrides like $NaBH_4$ or $KBH_4$ very little attractive.

Based on the findings presented here, similar lithium borohydride - rare earth hydride systems will be examined for lanthanum and ytterbium, the former in order to verify or reject the storage and sorption properties already forecasted, the latter to extend our knowledge onto a rare-earth element of divalent nature.

# Equipment and Experiments

## 4.1 Tools, instruments and programs

In this section, the tools, instruments, programs and other techniques used to do the experiments and analyses are presented and explained. We will also focus on features and challenges which come into play when the theoretical framework is applied on real systems. The actual numerical details about the performed experiments are presented in the section 4.2.

### 4.1.1 Ball milling

The Fritsch Planetary Micro Mill Pulverisette 7 (P7) and Pulverisette 6 (P6) are used in this work. Ball mills are commonly used to reduce the particle size or activate the surface, but they can also be used to introduce catalysts into a powder or initiate mechanochemical reactions. The reduction of particle size by energetic milling highly enlarges the surface of a given amount of material, and is preferred when a chemical reaction is desired. The particle size is normally reduced to a few micrometer. Having crystallites of this size or smaller is also of crucial importance when the sample is investigated with powder X-ray diffraction (PXD). This will be explained further in section 4.1.3. Photographs (figure C.1 and C.2) are shown in appendix C at the end. A hand mortar and pestle was used to crush some of the reactants that came in the form of large particles (1 mm) into powder, before milling was initiated.

The P7 mill is a rather simple mechanical tool. It consists of two rotating vial holders mounted on a rotating plate. This plate rotates in the opposite direction, in order to create large changes in the centrifugal force inside the bowls. The mill is called planetary because the two rotations evolve in the same plane. The grinding vials are made of tempered steel, have a capacity of 40 mL, and are filled with grinding balls of tempered steel (diameter 1.00 cm) and the powder mixture. Once the bowls are filled with balls and powder in argon atmosphere, they are closed with lids of tempered steel and rubber gaskets, secured with a steel frame and finally fastened to the rotating frames by a screw clamp (figure C.3). The mill has a timer to control the total milling time, and the rotating speed can be set to a value between 100 and 800 rpm.

The P6 is similar, but larger and more powerful, and here a counterbalance is used instead of two vials, which must be adjusted to the weight of the vial. In this way, only one batch can be prepared at a time. The volume of the P6 vial is 200 mL, and the vials and balls are made of stainless steel. The vial can be outfitted with a special GTM (Gas pressure and Temperature Measurement system) lid containing temperature and pressure sensors for *in-situ* measurement. Since these have resolutions of 0.1°C and 1 mbar respectively, more powder was this time milled, in order to ensure strong enough signals.

The sensors were connected to a tabletop data acquisition device by a wireless transmitting unit, and the pressure- and temperature values were recorded real-time during milling on a computer using the Fritsch GTM software.

The temperature inside the P6 raised to about 31°C at 400 rpm after five hours of milling. Milling at maximum speed caused the temperature to rise to approximately 80°C. This temperature rise comes obviously from the electric engine and the friction from all the moving parts. The temperature is not expected to exceed these values in the P7, because the power consumption is lower. In each case, a temperature raise due to mechanical motion of more than 100°C is not considered possible. An exothermic reaction may of course cause the temperature to raise higher. This is important information, because many samples are observed to undergo phase transformations or reactions when heated.

### 4.1.2 Sample preparation

In order to investigate the milled mixtures with powder X-ray diffraction, the milled powder was brought inside Hilgenberg boron glass or quartz capillaries with diameter 0.5 mm and length ca. 80 mm. A thin rod of glass (diameter 0.3 mm) was used to push the powder inside the capillary. Finally, the capillary was cut in a length suited to the geometry of the X-ray diffractometer (ca 4 cm) and sealed with two-component glue. All handling of the powder including the filling of the bowls was done under argon gas in a MBraun Unilab glovebox (figure C.4) with oxygen and water sensors. The amount of oxygen and water was kept below 1 ppm.

### 4.1.3 Powder X-ray diffraction

#### Geometry

Initial characterization of the starting materials and milled samples was done with a Bruker AXS D8 Advance laboratory diffractometer, which utilizes a Göbel mirror of type GM2 to make a parallell beam onto the sample. The diffractometer is photographed in figure C.6. The sample can be mounted either as a flat plate (used together with Bragg-Brentano geometry), where the rays are reflected and only scatters in the space above the surface, or in a thin, rotating glass capillary (used mainly together with Debye-Scherrer geometry), where the ray is transmitted through the sample. In Debye-Scherrer geometry, the sample is a powder, ideally defined as a collection of infinitely many random oriented crystallites, which are small, often microscopic single crystals. A powder grain consists typically of a number of crystallites. These two geometries are schematically illustrated in figure 4.1. A photograph of the capillary attached to the Bruker sample holder is shown in figure C.5. The capillary geometry was chosen in this work, mainly because oxygen shielding becomes much easier. Additionally, the flat-plate option would require much more material, because the sample should be as thick as possible in order accurately measure the intensities of the peaks and minimize peak shift and asymmetric broadening. This is a problem with respect to the expense of the powders.

#### The diffraction pattern

When the X-ray beam is scattered by a (hkl) plane in a certain crystallite according to Bragg's law (equation 3.1), the scattering angle between the exiting and incoming ray is the only restricted coordinate. In a powder, the normals (direction [hkl]) of the scattering

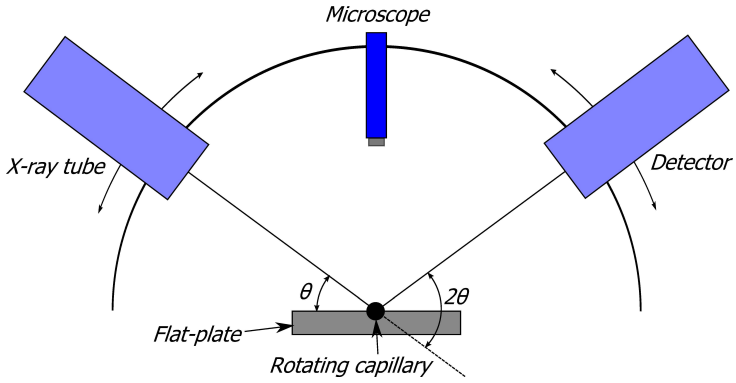


Figure 4.1: The setup of the X-ray tube, the sample and the detector for Debye-Scherrer (capillary) and Bragg-Brentano (flat-plate) geometry.

(hkl) planes have all the same angle with the incoming beam, but they point in arbitrary radial directions. For this reason, there will be a cone in reciprocal space wherever the diffraction condition is fulfilled. Onto a screen perpendicular to the incoming ray, these cones will be projected as circles, showing intensity $I_{hkl}$ as a function of scattering angle $2\theta_{hkl}$. As this image in principle has no information in the azimuthal coordinate, the intensity is integrated all the way round from 0 to $2\pi$ (or over the available range) with a one-dimensional diffraction pattern (also called diffractogram or histogram) as a result. In figure 4.2, a two-dimensional (left) and the corresponding one-dimensional (right) diffraction pattern of $LaB_6$ are shown as an example. The reflections are called Bragg peaks. The $LaB_6$ pattern has a very low and flat background, but for poorly crystalline materials, it will be larger. The shape of the background may contain useful information: Different amorphous materials give different background shapes.

### Relative intensity faults

In macroscopic single crystals, [hkl] will always point in a certain three-dimensional direction, and the peaks will appear as spots on the screen, not circles. Different planes with the same or almost the same $2\theta_{hkl}$ will therefore still give distinguishable reflections on different spots on the screen, each with intensity $I_{hkl}$. From a powder, however, these reflections will completely or partially overlap, and may be difficult to distinguish.

If now the crystallites happen to be very large, there will be fewer diffracting crystallites in a given volume, and the intensity distribution along the circle will be far from uniform. Consequently, the repeatability of the measured Bragg peak intensities will be low. For example, in a sample volume of 20 $mm^3$, if there is around 12 diffracting crystallites with diameter 40 $\mu$m, will there be around and 38 000 if the diameter is 1 $\mu$m[21].

Furthermore, if only one crystallite scatters, and this happens to be a single crystal, the diffraction condition $\Delta k = \vec{G}$ will in general not be fulfilled for a certain spatial orientation of the crystal. This is because the Ewald surface has no volume. Rotation of the sample will then lead to a set of points in reciprocal space which will lie exactly on this surface, producing a single-crystal diffraction pattern. The larger angle the sample is rotated, the lesser is the chance that any reflections are lost[20].

For our purposes, large crystallites and single crystal grains may be the result of a melting and subsequent solidification under pressure. It will then be useful to consider the

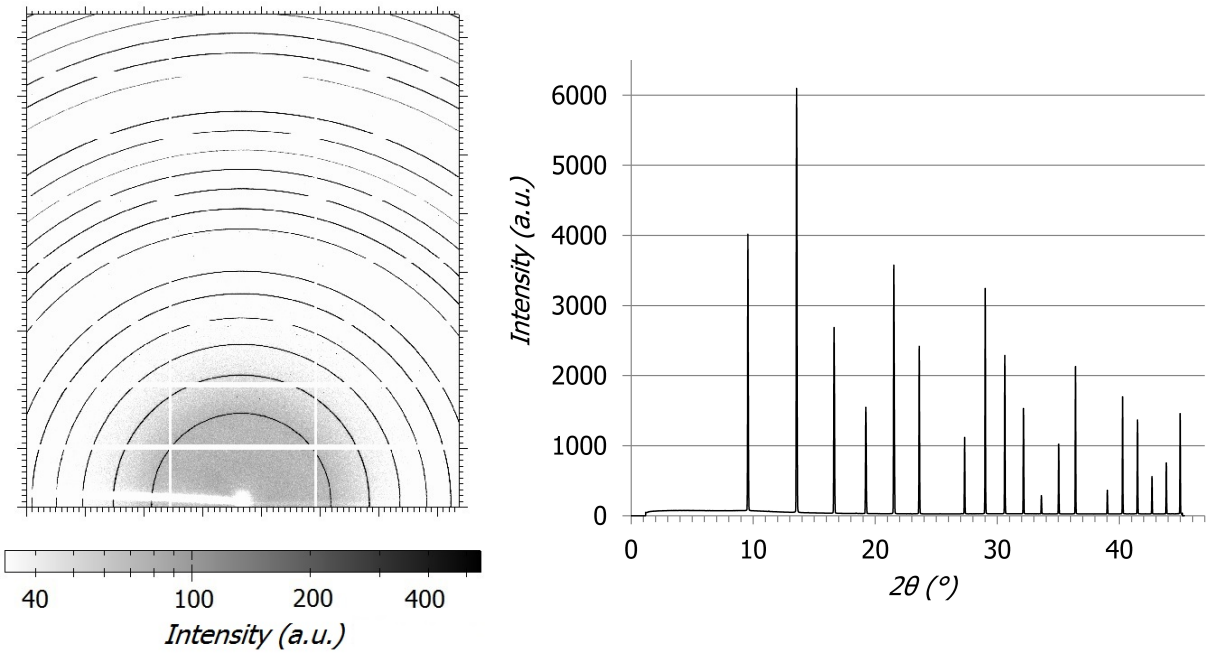


Figure 4.2: Left: Unintegrated diffraction rings from the common calibrant $LaB_6$ obtained with synchrotron radiation PXD. Right: One-dimensional diffraction pattern of $LaB_6$ obtained by integrating each diffraction ring over the azimuthal angle. Consequently, the intensity values for each peak is ten-fold increased.

unintegrated patterns. Moreover, the crystallites may reorient themselves in a systematic manner during solidification, such that the reflections will be overrepresented in certain crystallographic directions. This is called preferred orientation or sample texture. The relative intensities changes severely, and in a worst-case scenario, some reflections may be completely gone. This effect is much less pronounced for capillary geometry compared to flat-plate geometry[21]. Because of the directional dependence of $I_{hkl}$, the effect can actually be used to extract overlapping integrated intensities, which we will not discuss further here.

To increase the number of crystallites radiated and reduce the effect of preferred orientations, the glass capillary was therefore rotated around its axis constantly during measurement with a rotation frequency in the order of magnitude 1 Hz.

### Peak broadening

The capillary geometry requires much less material, but this also means that the grain size should be very small in order to have enough material and sufficiently many crystal orientations under the beam. Grinding is an effective tool to reduce the grain size down to and below 1 $\mu$m and thereby ensure a high packing fraction and proper powder statistics. However, grinding can also introduce disordered regions, strain or other defects in the crystallites which broaden the peaks. Internal stress, dislocations or altered stoichiometry that change the lattice constant along the scattering vector lead to so-called *strain broadening* of the peaks. The length (along the scattering vector) of coherent diffracting regions determines the *size broadening*. These regions usually correspond to the averaged crystallite size, but they can also be bounded by stacking faults or dislocations within the crystallites[21]. The peak width increases inversely proportional with the length of the

coherent region, but with laboratory diffractometers, the size effect is not seen until the crystallites are in the order of magnitude $\sim 10$ nm, and such small grains are usually not produced with a mechanical mill.

**Data quality**

In order to detect partial overlapping peaks and accurately determine the peak intensities, high resolution in $2\theta$ is desired. This is governed by the ray divergence, the collimation of the beam and the detector. Narrow collimation has the penalty of reducing the beam intensity. Therefore, short data acquisition time and high resolution can in principle not be achieved simultaneously. The signal-to-noise ratio can be improved by letting the ray radiate longer onto the sample per step or perform several scans which are finally added together. This is also set by the user. For the Bruker diffractometer and the samples studied here, a scan speed of 1-2 sec/step was usually enough to get a scan of sufficient quality for a database search. It is important that the step length, set by the user, matches the peak width. Otherwise, the pattern curve will not be smooth. The X-ray tube and the detector rotate around the sample (see figure 4.1) in order to scan all Bragg angles of interest, defined by the user.

The required quality of the pattern depends of course also on its purpose. For an initial scan, the aim is to get an overview about the location of the Bragg peaks. For indexing purposes, uncertainty in the position of the peaks should be minimized, high resolution is desired and approximately 20 peaks are needed to get a reliable solution. For structure refinement purposes, a pattern obtained from synchrotron radiation powder diffraction is usually required. Neutron diffraction is helpful to determine the atomic positions of light elements which have low X-ray scattering strength.

### 4.1.4 Synchrotron X-ray diffraction

To acquire diffraction patterns of high resolution and to investigate samples under different conditions, synchrotron radiation powder X-ray diffraction (SR-PXD) was used at the European Synchrotron Radiation Facility (ESRF) in Grenoble, France. The synchrotron accelerates electrons up to 6 GeV before they are sent into a storage ring of diameter 268 m. Very strong bending magnets with superconducting coils are situated along the ring and accelerate the electrons inwards, forcing them to run in a circle. The resulting change in momentum of the electrons produces a X-ray beam, which is sent outwards and collimated. At each bending magnet, there is thus a research laboratory making use of the radiation for several purposes (see figure C.9). There are insertion devices in the straight sections of the storage ring where experiments can be performed as well[44]. In this work, experiments were performed at station A at the Swiss - Norwegian beamline (SNBL), which is situated at bending magnet one (BM01).

Because of the geometry of the synchrotron, the beam is naturally collimated in the vertical plane. A synchrotron radiation source has very high brightness ($\frac{\text{photons}}{\text{mrad}^2\text{s}}$ for a given bandwidth). It is therefore possible to collimate the beam very hard in the horizontal plane and still have a high intensity ray onto the sample. The PILATUS 2M detector used in this work has a grid of semiconductor cells, each being a detector of size 0.102 $\text{mm}^2$, capable of measuring single photons. This allows for a high signal-to-noise ratio, since a certain photon energy threshold can be set. The resolution of the detector is so high that sample imperfections like those discussed above actually influences the shape

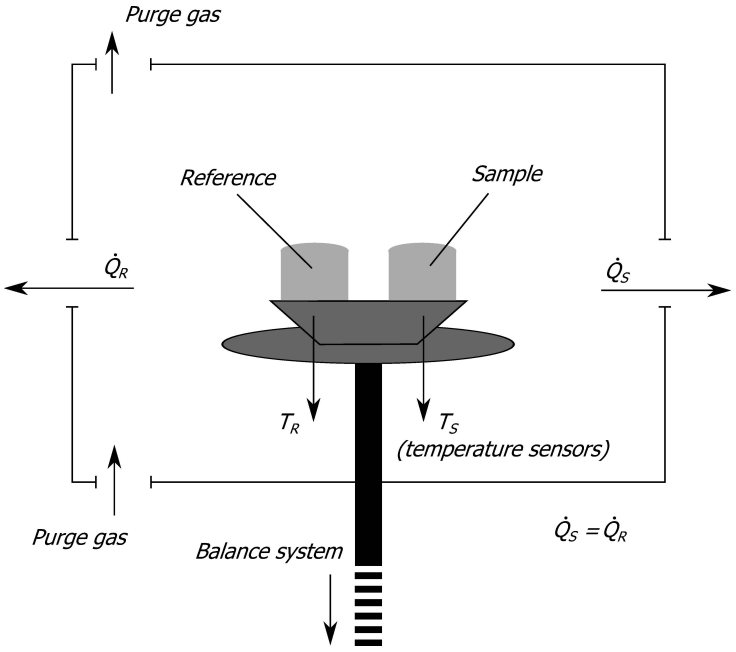


Figure 4.3: Schematics of the DSC-TGA instrument setup

of the Bragg peaks. The detector also has a high dynamic range, and it can be moved in three spatial directions[45].

The larger the sample-detector distance is, the sharper is the image and the narrower the field of view, and the other way around. The sample could be rotated, tilted and moved sideways. An in-house developed software called Pylatus was used to manage the detector motors (figure C.13 and C.14). Another software, Fit2d, was used to integrate the diffraction rings and refine the wavelength and sample-to-detector distance.

The geometry and available space in the laboratory hutch allows many different *in-situ* experiments to be performed. The sample could be connected through air-tight Swagelok fittings and valves to a certain gas environment up to 125 bar. The valves of the gas rig (figure C.12) was be governed from a LabVIEW program specially tailored for this purpose (figure C.15). The sample could be heated by a programmable furnace combined with a gas blower, which was mounted very close ($<$ 1 cm) to the sample. Infrared and Raman spectroscopy can also be performed in order to follow the development of amorphous phases, however, this was not done in this work. These instruments and the detector are shown in figure C.10.

### 4.1.5 Differential scanning calorimetry and Thermogravimetric analysis

The Netzsch STA 449 *F3* Jupiter apparatus is a combined Differential Scanning Calorimeter (DSC) and a Thermogravimetric Analyzer (TGA). Since heating of the sample is done in both techniques, a simultaneous instrument setup is possible, depicted in figure 4.3. A sequence of heating/cooling ramps and isotherms can be programmed for temperatures above room temperature. During measurement, the heat flow from the sample and the weight change is measured.

The term Termogravimetric Analysis is used when the weight of the sample is recorded during heating. The weight changes because of uptake or release of gases. The sample

is usually linearly heated, with a heating rate of $2 - 10°C/min$. A double-tubed furnace is lowered around the sample prior to the experiment (see figure C.7 and C.8). Delicate sensors in the balance mechanism are able to measure forces corresponding to 0.001 mg. The space inside the furnace can constantly be flushed with hydrogen or an inert gas, to protect the sample and keep the atmosphere the same. This will minimize changes in the buoyancy force from the surrounding gas during the experiment. The balance can be tared from the Netzsch software.

Differential Scanning Calorimetry is a calorimetry technique where changes in the difference in heat flow rate between the sample and a reference is measured. The Netzsch apparatus uses a heat flux DSC setup, where the furnace surrounds both the sample and the reference. In this way, equal heating parameters for the sample and the reference are ensured. The sample is placed in a crucible with a lid. The reference is either an empty crucible of the same type or a crucible filled with some inert material. The crucibles are then placed on two plates with build-in temperature sensors. There is a sensor measuring the heat from the reference and the sample as well[46].

Before an experiment is conducted, an empty crucible of the same type as which will be used in the experiments is heated at the correct rate up to a sufficiently high temperature. The resulting DSC and TGA traces are used as a baseline for the experiments. Before the crucible is filled with the sample, the balance is tared with the empty crucible in place.

The TGA trace from the experiments shows the weight of the sample as a function of time or temperature (can be chosen by the user) in percentage of the starting weight. The DSC trace shows qualitatively the absorbed or released heat from the sample in sensor signal strength ($\mu$V/mg), plotted with more positive or more negative values respectively. A positive extremum is related to an endothermic reaction in the sample, and a negative extremum to an exothermic reaction. For borohydrides, an endothermic peak combined with a weight loss can be related to a decomposition reaction, and an endothermic event without associated weight loss can either be attributed to a structural phase transition or melting. Sometimes decomposition and melting happen in a very narrow temperature region and both events can be superimposed on each other. In this case, DSC-TGA experiments during heating are not sufficient to elucidate the nature of the events and additional experiments upon cooling or the use of a melting point apparatus should be considered. An exothermic peak can be associated with a chemical reaction or a crystallization.

### 4.1.6 Residual gas analysis

The gas flow through the DSC-TGA instrument was led to a MKS Microvision-IP quadrupole mass spectrometer and analyzed with the ProcessEye software. This technique will be denoted residual gas analysis (RGA). The gas particles are ionized at a filament and accelerated through a tube. An electric field pulls the particles in one direction, such that the lightest particles are deflected the most. The charge-to-mass ratio is then used to determine the type of molecule, and pressure sensors that monitor the partial pressure of each particle type determine the fraction between them. Two kinds of detectors were used: One standard Faraday cup (FC) detector which monitors partial pressures down to $10^{-7}$ mbar, and one SEM multiplier detector that monitors pressures below $10^{-6}$ mbar. The filament pressure was kept below $10^{-4}$ mbar, and the water level was below $10^{-7}$ mbar.

### 4.1.7 Sieverts technique: Pressure-Composition-Temperature experiments

The Sieverts technique denotes one of two types of experiments usually performed in order to measure the sorption kinetics and the hydrogen uptake in storage materials and thereby to make the pcT- and van't Hoff plots discussed in section 4.2.5. In this method, which is also called volumetry, the amount of gas that is desorbed or absorbed is calculated by considering the temperature, pressure and initial volume of the gas surrounding the sample. The other method, called gravimetry, makes use of an in-build micro-balance that is computer controlled and monitors the sample weight during measurement. Although no isothermal pcT experiments are performed in this work, the importance of Sieverts techniques in respect to hydrogen storage research is so immense that classical volumetry will be briefly outlined in the following. Moreover, the equipment description and possible sources of errors are of greatest relevance for the non-isothermal experiments performed[47].

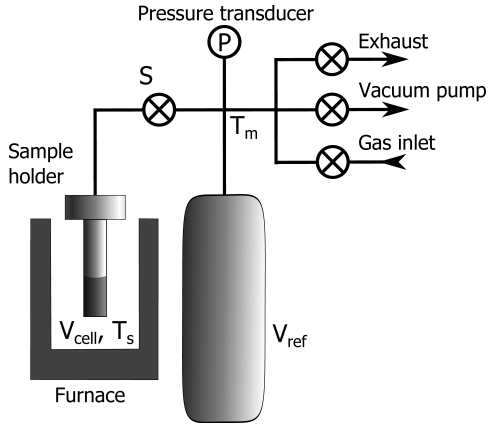


Figure 4.4: pcT apparatus

The minimal apparatus necessary for a volumetric hydrogenation is depicted in figure 4.4. A closed system which includes the reference volume $V_{ref}$ and excludes the sample cell $V_{cell}$ contains a known amount of hydrogen gas at pressure $p_{ref}$, found by knowing the exact total volume $V_{ref} + V_{cell}$, temperature $T_m$ and compressibility $Z(p, T)$ of the gas. The temperature in the sample cell is $T_s$. The gas is initially kept away from the evacuated sample compartment by a valve $S$. The reference volume is simply a container with volume much larger than the manifold and $V_{cell}$, in order to fulfill certain requirements for the ratio $V_{cell}/V_{ref}$ discussed below.

The procedure goes stepwise as follows: Valve $S$ is opened for a short time such that a little amount of hydrogen gas is let into the sample cell. A system pressure $p_{sys}$ is established throughout the whole system ($V_{ref} + V_{cell}$) while the valve is open, together with a new temperature $T_s$ and in principle also a new $T_m$ (although in practice, the latter is constant). When the valve is closed, the hydrogen gas enclosed in the sample cell may be absorbed or the sample may desorb gas (depending on the system pressure and sample temperature), and a new pressure is established in the cell. This state should be kept for a sufficiently long time so that equilibrium is reached and the old value of $T_s$ recovered, in order to produce an isothermal pcT curve. Then, valve $S$ is opened again, and if the amount of gas in the total system is different, $p_{sys}$ will also change from the last step[48].

The number of moles of absorbed or desorbed gas in the $k$th step, $\Delta n^k$, is now calculated from

$$\begin{aligned}\Delta n^k = &\left[\frac{p^k_{ref}}{Z(p^k_{ref}, T^k_m)RT^k_m} - \frac{p^k_{sys}}{Z(p^k_{sys}, T^k_m)RT^k_m}\right] V_{ref} \\ &- \left[\frac{p^k_{sys}}{Z(p^k_{sys}, T^k_s)RT^k_s} - \frac{p^{k-1}_{sys}}{Z(p^{k-1}_{sys}, T^{k-1}_s)RT^{k-1}_s}\right] \cdot (V_{cell} - V_s)\end{aligned} \tag{4.1}$$

$V_s$ is the sample volume. The first bracket is the number of moles that are let into

the sample cell once $S$ is opened at step $k$. Now, in case of absorption, some of this gas is used to fill the "free space" in the sample cell provided by the amount of gas that has been absorbed during the last equilibration (second bracket), and with this amount subtracted, the residue is the absorbed amount.

$Z(p,T)$ has been previously calculated at IFE by two-dimensional regression from experimental data collected from NIST's webpage[49].

$$Z(p,T) = \frac{Z_0 + A_{01}p + B_{01}T + B_{02}T^2 + C_{02}pT}{1 + A_1p + B_1T + A_2p^2 + B_2T^2 + C_2pT} \tag{4.2}$$

$Z_0$, $A_{01}$, $B_{01}$, $B_{02}$, $C_{02}$, $A_1$, $A_2$, $B_1$, $B_2$ and $C_2$ are constants fitted experimentally.
The accumulated uptake is consequently

$$\Delta n = \sum_k \Delta n^k \tag{4.3}$$

By monitoring the change in $p_{sys}$ and the host-to-hydrogen atomic ratio $H/X = \frac{\Delta n}{M/m}$ ($M$ and $m$ are the mass and molar mass of the sample, respectively) from step to step, an isothermal pcT curve can be drawn[48].

There are numerous artifacts that may cause severe errors in this calculation. A review article by D. P. Broom[47] summarizes the most important error sources related to hydrogen sorption experiments. Those that apply for hydrides and are relevant here are mentioned in the following.

**System volume and sample size.** The uncertainty of all relevant volumes should be significantly lower than the volume of the sample. For this reason, hydride samples should be heavier than 50 mg, depending on the density and absorption capacity. The system volume must be so small that the pressure changes are bigger than the uncertainty of the manometer, and it must be so large that a possible sample expansion during hydrogenation cannot affect the volume of the gas.

**Temperature measurements.** The sample and manifold temperatures should be known with high accuracy. Very important is also to minimize possible temperature gradients, which will be present for temperatures far beyond or below the ambient temperature. This could cause cold or hot "spots" in the tubing which produces severe errors. Moreover, if the tube diameter is in the order of magnitude of the free mean path of the gas molecules, which is often the case, a temperature gradient along the tube will produce a pressure gradient as well, consequently increasing the error. This is known as the thermo-molecular effect. In a poorly designed system, it can cause errors up to 100% in the pressure readings. Measuring the sample temperature can be done with a thermocouple placed very closed, even into, the sample. In the setup used in this work, the thermocouple was embedded in the wall of the sample cell, and smeared with copper paste to maximize heat conductivity.

**Thermal effects from the sample.** Hydrides normally absorb hydrogen via an exothermic reaction and the generated heat will obviously affect the measurement. With small aliquots during hydrogenation the effect can be lowered, since the heat will be distributed over multiple, smaller steps, and by letting each step equilibrate properly, the calculations can still be performed. Large aliquots can cause a shift in the plateau pressure.

**Equilibration time.** As mentioned, long enough equilibration times are required to get a proper isothermal pcT curve and consequently correct van't Hoff's plot. If the system is not in equilibrium at step $k$, wrong pressure values will be read. Too bad equilibration will cause the plateau to be shortened, in particular in the high-capacity end, resulting in underestimation of the total sorption capacity.

**Equation of state** Obviously, the ideal gas law would yield unacceptable errors for other than ambient conditions. Choosing the right equation of state is a matter of choosing the best compressibility function, since the real gas law $pV = Z(p,T)nRT$ is the most general case, and all other equations of states like van der Waal's gas law can be rewritten into this form. Different compressibility functions are suited for different pressure and temperature ranges, and the most accurate model for the high pressures and temperatures used in this work is considered to be the one proposed by Hemmes[50].

**Sample activation** The sample may need to be activated, so that the surface is free of any inhibiting coating, which will hamper the sorption kinetics. This can be done by ball-milling the powder and/or perform degassing towards high vacuum (between $10^{-4}$ and $10^{-8}$ mbar) at elevated temperature. For hydrides, desorbing and absorbing the sample a few times is often done to activate it. Even for some new-prepared samples is activation of crucial importance for access to the full storage capacity. In this work, the samples were treated exclusively in an inert environment after milling to ensure no contamination on the surface, and the sample cell was evacuated to a pressure below $5 \cdot 10^{-6}$ mbar, so that a proper activation was secured.

**Leakage** There will always be a leakage in the system, especially over the valve seats, but the leak rate should never result in pressure changes comparable to the initial and final $p_{sys}$ difference. Leak testing can be performed by either filling the system with an inert gas up to the maximum measurement pressure or evacuating it and let the pressure reach a certain lower limit, experimentally found defined for a specific vacuum pump ($5 \cdot 10^{-6}$ mbar in this case). If the pressure change $\Delta p$ due to a leak is much smaller than $p_{sys}$, the leak rate will be almost constant, i.e. the pressure drop will be linear. In appendix A, this is shown mathematically under certain physical approximations. If an absorption curve for example approaches a linear decreasing asymptote for large times, this may be the sign of a leak, and the asymptote can be subtracted in order to get the real absorption curve. It should be noted, however, that the argumentation assumes that the area of the leaking hole in the compartment is constant. In practice, one can imagine that the hole may be larger with higher pressure, depending on what causes the leakage, which will make the curve more exponential. But it has been observed by leak-testing that this effect is usually negligible.

In a volumetric measurement, errors made in a single aliquot will accumulate through the complete measurement for the given isotherm, as opposed to the gravimetric technique, where this is not an issue.

In this work, the pcT experiments are not made stepwise, because it was desired to apply the same conditions as those used in the *in-situ* SR-PXD. In this way, the apparatus is used to measure the absorption and desorption kinetics and is at the same time acting as a hydrogenator. Consequently, isothermal pcT curves and van't Hoff plots cannot be

generated, but the uptaken or desorbed amount of hydrogen can still be calculated, if care is taken to the above mentioned possible error sources, except for the issue of reaching equilibrium at each step, which only applies for isothermal measurements.

### 4.1.8 Auto-indexing, structure solution and refinement

#### Phase identification

After the diffraction pattern has been acquired, known phases can be identified by several methods:

1. Search for peaks belonging to a certain phase manually by reading off the scattering angles and relate them to a suggested unit cell by using Bragg's law.

2. Import the diffraction pattern into a refinement program (for example GSAS), load so-called *crystallographic information files* (CIF) of phases that are expected to be present and fit the calculated pattern with the measured one. (A CIF file contains information about the crystal system, space group, atomic positions, thermal displacement factors *etc.* of a phase, and can be downloaded from sources like the *Inorganic Crystal Structure Database* (ICSD)[51]).

3. Do an automatic search by using a search engine that utilizes different search criteria like high and low symmetry patterns *etc.* In this work, the engine embedded in the Bruker DIFFRAC Plus EVA software was used, which had access to the *International Centre for Diffraction Data* (ICDD) database.

#### Indexing, space group determination and peak extraction

No unknown diffraction pattern of major importance was found in this work, and therefore, we will only for the sake of completeness briefly describe the methods used to arrive at the crystal structure from an unknown pattern.

The reflections belonging to the unknown phase must first be properly localized and verified to belong to the same phase. They can then be auto-indexed with the use of programs like DICVOL or TREOR, which are based on the indexing procedure outlined in the theory section[52]. They will come up with a probable crystal system with lattice parameter(s) that explains as many peaks as possible with as small unit cell as possible[21]. One can manually define the number of allowed unindexed lines. Then, the program CHECKCELL can be used to explore suitable space groups. The indexing and space group determination can also be done in the program FOX[53][54].

Once a plausible space group and a lattice are known, a crystal model can be build in FOX. The real diffraction pattern is imported as well, and an iterative least squares fit (implemented in the Le Bail method) of the diffraction pattern is performed initially in order to fine-tune the unit cell parameter(s). The Le Bail method extracts the single integrated intensities $I_{hkl}$ by applying the mathematical relations between Bragg reflections. The algorithm takes as input a set of arbitrary structure factors and refines simply the appropriate profile parameters, no matter what kind of atoms (or how many) there might be placed in the unit cell. the observed pattern is now adjusted to the ratios between the calculated reflections, and these are used as a new input set, and so on until the refinement converges. If the initial Le Bail-procedure does not give any good fit, it

is certain that no crystal model will explain the diffraction pattern with the given lattice and space group[44].

The chemistry of the system should be known as far as possible, so that one is able to make a good guess at the correct atomic arrangement. When a certain basis is build in the unit cell, a global Monte Carlo optimization procedure can be conducted in FOX. At each configuration trial, the diffraction pattern from the structure model is compared to the real diffraction pattern. If two atoms are placed too close by the program, they will have to be kept away from each other by a minimum distance, set by the user. If an atomic coordinate is locked, it will stay the same, otherwise it will become one of the parameters in the Monte Carlo optimization. Several trials will hopefully give the right structure solution, with the right atoms placed on approximately the right positions[6].

**Rietveld refinement**

The precise atomic positions can lastly be found using the Rietveld refinement method, implemented in for example the FullProf or GSAS[55] programs. The Rietveld method is similar to a Le Bail fit, but is different in the first place because the atom positions and types now are specified and constrains the calculated $F_{hkl}$. The minimizing function in a Rietveld refinement[44] is based on a discretized data set with $n$ points:

$$M = \sum_{i=1}^{n} w_i (y_i^{obs} - y_i^{calc})^2 \tag{4.4}$$

where the weight $w_i = \frac{1}{\sigma_i^2}$ is the inverse of the squared variance and $y_i^{obs}$ and $y_i^{calc}$ are the pattern values at point $i$ for the observed and calculated pattern respectively. The latter is calculated from

$$y_i^{calc} = b_i + S_i \sum_{hkl} M_{hkl} L_i P_i A_{hkl} T_{hkl} \left|F_{hkl}\right|^2 \Phi(\Delta 2\theta) \tag{4.5}$$

The background $b_i$ is described either manually or by refining a polynomial (The Shifted-Chebyshev polynomial is used in this work) with a certain number of terms. If there is large variation in the background, it often has to be selected manually to get a good fit. $S_i$ is a scaling constant, $M_{hkl}$ the multiplicity factor originating from symmetrically equivalent reciprocal lattice points, $L_i$ is the Lorentz factor which depends on the diffraction geometry, $P_i$ is the polarization factor (beam polarization may cause uneven intensity distribution), $A_{hkl}$ is the absorption coefficient and $T_{hkl}$ is a factor correcting for preferred orientations. $\Phi(\Delta 2\theta) = \Phi(2\theta_{hkl} - 2\theta_i)$ is the profile function incorporating instrumental and sample broadening around peak $2\theta_{hkl}$. In this work, the so-called pseudo-Voigt profile function $\Phi_{PV}$ was chosen, which is a linear combination of a Gaussian and a Lorentzian function, considered to be one of the best choices for powder diffraction:

$$\Phi_{PV} = \frac{1}{\pi} \frac{\Gamma_L/2}{(\Gamma_L/2)^2 + (\Delta 2\theta)^2} + \frac{2}{\sqrt{\pi}} \sqrt{\frac{4ln2}{\Gamma_G^2}} e^{-4ln2(\frac{\Delta 2\theta}{\Gamma_G})^2} \tag{4.6}$$

The instrumental resolution broadening is predominantly represented by the Gaussian full peak width at half maximum (FWHM) $\Gamma_G$, whereas the sample broadening from crystallite size and strain effects discussed in section 4.1.3 is the origin of the Lorentzian FWHM $\Gamma_L$. They are angle dependent in the following way:

$$\Gamma_G = \sqrt{G_u tan^2\theta + G_v tan\theta + G_w} \tag{4.7}$$

$$\Gamma_L = \frac{L_y}{cos\theta} + L_x tan\theta \tag{4.8}$$

Here, $G_u$, $G_v$, $G_w$, $L_x$ and $L_y$ are the profile parameters that may be refined in GSAS. The two latter, $L_x$ and $L_y$, correspond to the crystallite size and the strain in the sample, respectively. A variable correcting for asymmetries introduced by the measurement geometry can also be refined.

The unweighted and weighted profile factors $R_p$ and $R_{wp}$ and the goodness of fit $S_{wp}$ are measures of how well the calculated pattern fits the measured one. The profile factors should be as small as possible (usually given in percent). $S_{wp}$ should also be as small as possible, although it is always larger than one.

$$R_p = \frac{\sum_{i=1}^{n} \left| y_i^{obs} - y_i^{calc} \right|}{\sum_{i=1}^{n} y_i^{obs}} \tag{4.9}$$

$$R_{wp} = \sqrt{\frac{\sum_{i=1}^{n} w_i (y_i^{obs} - y_i^{calc})^2}{\sum_{i=1}^{n} (y_i^{obs})^2}} \tag{4.10}$$

$$S_{wp} = \frac{\sum_{i=1}^{n} w_i (y_i^{obs} - y_i^{calc})^2}{n - p} \tag{4.11}$$

$p$ is the number of refined parameters. It is clear that $S_{wp}$ might become less than one if the background is chosen manually: The fit might be very good, although the refined parameters are few[3][44].

The isotropic mean displacement factors $\langle u^2 \rangle_j$ defined in section 3.1.2 can be refined with the parameter $u_{iso}$, measured in units of Å$^2$. By considering the structure factor (equation 3.10), it is clear that the peak intensity is dependent on $\langle u^2 \rangle_j$ for a given atom type j. Therefore, for a large unit cell consisting of numerous elements, the $u_{iso}$ values can take up relative intensity errors originating from other sources, like poor statistics, preferred orientation and absorption effects. With powder diffraction data, it is hard to accurately determine the $u_{iso}$ parameters, but they should lie within $0.01 < u_{iso} < 0.05$ at room temperature, and at least not be negative. $u_{iso}$ should moreover be larger for lighter atoms. This is easily seen by considering a classical harmonic oscillator with constant energy $E$ and frequency $\omega$ (the vibration is thermally exited). The maximum displacement of the particle with mass $m$ and "spring constant" $\kappa$ is then $x_0 = \sqrt{\frac{2E}{\kappa}} = \sqrt{\frac{2E}{m\omega^2}}$, so the displacement increases inversely proportional with the square of the particle mass. If the reflections from a phases are so weak that $u_{iso}$ cannot be refined, it is usually set to the standard value $u_{iso} = 0.025$.

All phases in the sample should be identified and included in the refinement. The fractions between them and the lattice parameters are always refined, and possibly the degree of substitution of atoms or molecules. For a new structure, the atomic positions should also be refined. In addition, one can refine the detector zero-point error, the wavelength (for calibration purposes) and several other instrumental and profile parameters. Only a few parameters should be refined initially, and later, others may be included, depending on the data quality and crystallinity of individual phases. Refinement of too many parameters simultaneously will lead to divergence.

All the important steps in the process of making and describing a new crystal structure are summarized in the flow diagram below (figure 4.5).

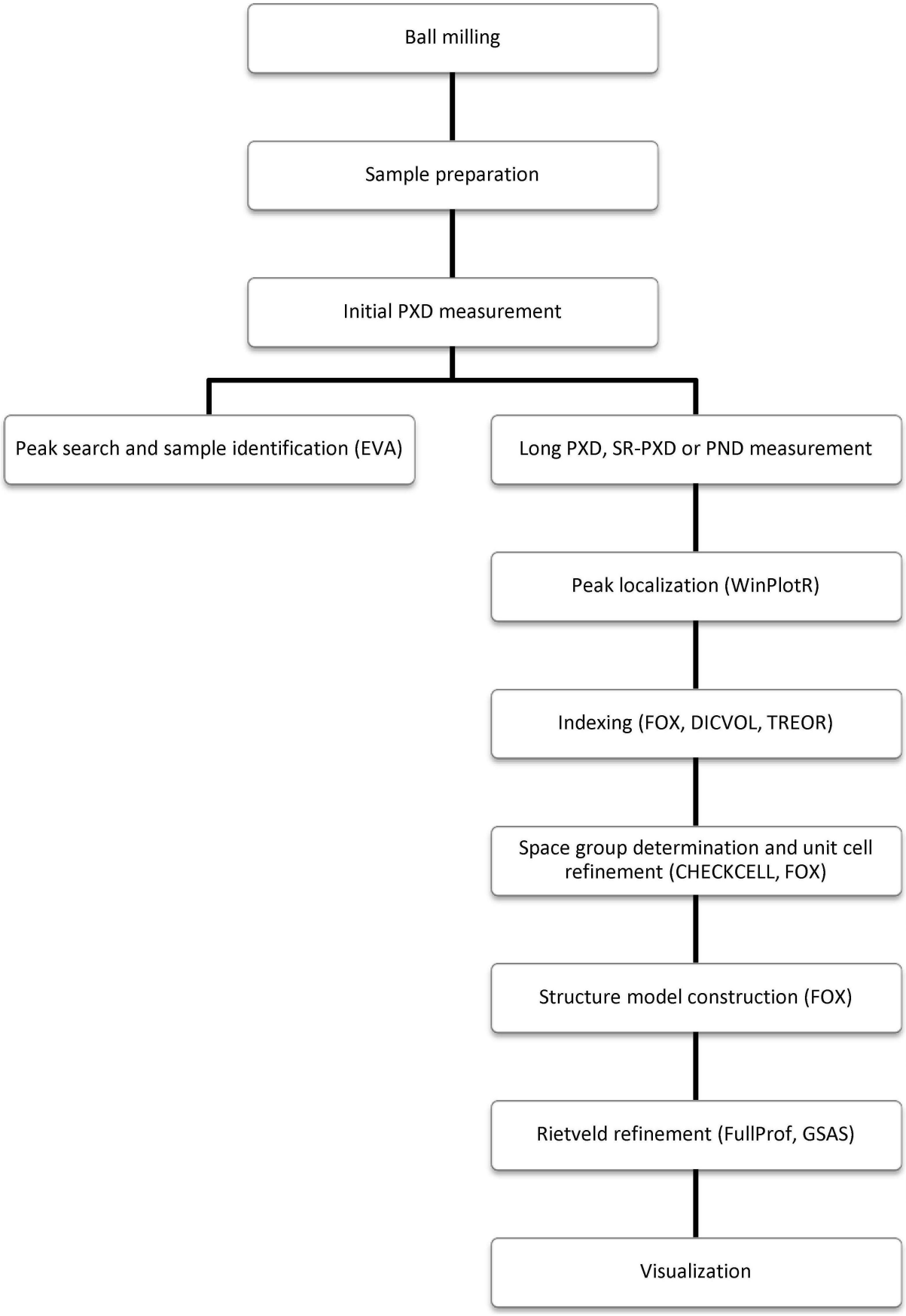


Figure 4.5: Flow diagram summarizing the important steps in the process of making and describing a new crystal structure. Useful programs are written in parenthesis.

## 4.2 Experiments

This chapter will contain the numerical and methodological specifications of the experiments, and the results will follow in the next chapter. The work in this master is partially based on samples prepared at IFE summer 2012 and SR-PXD experiments performed at ESRF in Grenoble November 2012 by a research team from IFE, the author included. Some of the results from these experiments are analyzed in this work, and will be presented here. Then, the supplementary and expanding experiments performed by the author in this work are presented. Table 4.1 summarizes all the experiments referred to in this work.

Table 4.1: Overview of all experiments used and analyzed in this work.

| Type of experiment | Place | Date | Experimentalist(s) |
|---|---|---|---|
| Sample preparation (P7) and characterization (lab-PXD, DSC-TGA) | IFE | Jun.-Jul. 2012 | IFE team members |
| *In-situ* SR-PXD characterization | ESRF | Nov. 2012 | IFE team members, author |
| Control check of old samples (lab-PXD, DSC-TGA-RGA) | IFE | Jan.-Feb. 2013 | author |
| Renewed sample preparation (P7) and characterization (lab-PXD, DSC-TGA-RGA) | IFE | Jan.-Feb. 2013 | author |
| Desorption and hydrogenation experiments (pcT) | IFE | Feb.-Mar. 2013 | author |
| Characterization of desorbed and hydrogenated samples (IR, lab-PXD, DSC-TGA) | IFE | Feb.-Mar. 2013 | author |
| Characterization of starting materials (High resolution SR-PXD, DSC-TGA-RGA) | ESRF, IFE | Mar.-Apr. 2013 | IFE team members, author |
| Pressure- and temperature monitored ball milling (P6) | IFE | Mar.-Apr. 2013 | author |
| *In-situ* SR-PXD characterization | ESRF | May 2013 | IFE team members, author |

### 4.2.1 Starting materials

Because of the uncertainty related to the absoluteness of the lattice parameters of $LiBH_4$, the batch used (Sigma-Aldrich, 95% purity) was investigated with SR-PXD, DSC-TGA-RGA and IR. This is important not only to check the state of the starting materials, but also to get as exact knowledge as possible about the crystallographic and thermodynamic properties for later analysis. LiH (Sigma-Aldrich, 95% purity) and the rare earth chlorides $LaCl_3$ and $YbCl_3$ (Sigma-Aldrich, 99.99% purity) were investigated by means of lab-PXD.

### 4.2.2 Sample preparation

**Sample preparation, summer 2012**

In June and July 2012, the mixture $6LiBH_4 + LnCl_3$ (hereafter denoted *Ln*, see sample notation in table 4.2) was milled for 5 h at a speed of 400 rpm for a series of rare earth elements. The samples of lanthanum and ytterbium were chosen to be investigated in this work, although the ytterbium containing sample, *Yb*, had been erroneously milled at a speed of 310 rpm. 7 balls were used to mill the powder mixture, which in every case weighted 0.700 g, giving a ball-to-powder weight ratio of 40:1. This constraint on the total sample weight combined with the molar ratios between the reactants, gives the following relations for the mass of the rare earth chloride ($M(LnCl_3)$) and the mass of lithium borohydride ($M(LiBH_4)$) in a given mixture ($m(LnCl_3)$ and $m(LiBH_4)$ being the molar masses of the respective compounds, $\mathcal{M}$ the total mass of the mixture):

$$M(LnCl_3) = \frac{\mathcal{M}m(LnCl_3)}{6m(LiBH_4) + m(LnCl_3)} \qquad M(LiBH_4) = \frac{\mathcal{M}m(LiBH_4)}{m(LiBH_4) + \frac{1}{6}m(LnCl_3)} \tag{4.12}$$

70 mg of each milled sample was extracted for further investigations, and the rest was milled for additional 1 h with lithium hydride in order to make the composite $6LiBH_4 + LnCl_3 + 3LiH$ (hereafter referred to as *LnLi*, see table 4.2). Similarly, the mass of the lithium hydride was found from the equation

$$M(LiH) = \frac{\mathcal{M}m(LiH)}{2m(LiBH_4) + \frac{1}{3}m(LnCl_3) + m(LiH)} \tag{4.13}$$

The sample notation for all analyzed samples is defined and the milling conditions are summarized in table 4.2.

Table 4.2: Sample notation. The temperatures given are the set temperatures for the programmable gas blower ($T_b$) in the SR-PXD measurements. *As-milled* is abbreviated a.m.

| Sample | Label |
|---|---|
| $6LiBH_4 + LaCl_3$ milled 5 h at 400 rpm | *La* |
| $6LiBH_4 + YbCl_3$ milled 5 h at 400 rpm/310 rpm[1] | *Yb* |
| $6LiBH_4 + LaCl_3 + 3LiH$ milled 1 h at 400 rpm | *LaLi* |
| $6LiBH_4 + YbCl_3 + 3LiH$ milled 1 h at 400 rpm | *YbLi* |
| a.m. $6LiBH_4 + LaCl_3$ heated to 400°C under vacuum | *LaVac* |
| a.m. $6LiBH_4 + LaCl_3$ heated to 400°C under back pressure | *LaBack* |
| a.m. $6LiBH_4 + YbCl_3$ heated to 400°C under vacuum | *YbVac* |
| a.m. $6LiBH_4 + YbCl_3$ heated to 400°C under back pressure | *YbBack* |
| a.m. $6LiBH_4 + LaCl_3 + 3LiH$ heated to 440°C under vacuum | *LaLiVac* |
| a.m. $6LiBH_4 + LaCl_3 + 3LiH$ heated to 440°C under back pressure | *LaLiBack* |
| a.m. $6LiBH_4 + YbCl_3 + 3LiH$ heated to 400°C under vacuum | *YbLiVac* |
| a.m. $6LiBH_4 + YbCl_3 + 3LiH$ heated to 400°C under back pressure | *YbLiBack* |

[1]The different milling speed had very little effect on the samples, and they are thus equally named.

The 2012 samples were characterized with DSC-TGA, heating them with a linear heating rate of 5°C/min up to 400°C. RGA was not performed in these initial experiments. *La*, *Yb* and *YbLi* were characterized with laboratory PXD short after synthesis.

#### Sample preparation, spring 2013

Since especially the pcT experiments required relatively much material, new batches of the samples *La*, *Yb* and *YbLi* had to be milled in spring 2013. Also, it was desired to mill the ytterbium samples again to investigate the possible consequences of different milling speeds. The new samples were compared to the old ones and verified by means of PXD measurements. The samples were now investigated with RGA as well.

### 4.2.3 Temperature- and pressure monitored milling, spring 2013

Exactly the same speed, milling time and powder-to-ball weight ratio were used in the P6 millings. The only difference was the amount of powder in the vial this time was 2.000 g. 20 balls were therefore used to obtain the same ball-to-powder weight ratio. The pressure and temperature data were read every 5.2-5.6 s.

The *LaLi* sample prepared in the P6 mill were brought to the SR-PXD session at ESRF in May 2013. They did not resemble exactly the same patterns as the previous synthesized *LaLi* samples, but were still considered usable. This will be discussed further in the result chapter.

### 4.2.4 SR-PXD measurements

#### SR-PXD, November 2012

*La*, *LaLi*, *Yb* and *YbLi* were investigated in November 2012 with SR-PXD at ESRF *in-situ* under decomposition and hydrogenation. *LaLi* was remeasured in another session in May 2013. The experiments were performed twice, first with the sample exposed to vacuum under decomposition, denoted *LaVac etc.*, and then with the sample exposed to a moderate back pressure of hydrogen (approximately 5 bar), denoted *LaBack etc.* (see table 4.2). The vacuum pressure could not be measured because it exceeded the lower range of the pressure gauge (10 mbar), but since a membrane pump was used, it was most probably between 1 and 10 mbar.

The PILATUS detector was set to acquire data over a period of 30 s, and used 8-10 s to reset. An image was therefore taken every 38 s approximately. A log file with filename, time, gas blower temperature ($T_b$) among other information was written for each image. The sample was heated from room temperature to $T_b = 400$°C at a heating rate of 5°C/min, with and without back pressure. The sample was then allowed to dwell at this final temperature for 20-30 min. Subsequently, approximately 100 bar of hydrogen pressure was introduced in the system, with $T_b$ kept still at 400°C for additional 30-60 min. Then, the sample was cooled slowly (5°C/min) to 300°C and faster ($10-20$°C/min) down to room temperature.

A heating rate of 5°C/min and data acquisition time of 38 s yields a $T_b$ step size of 3.2°C/min between each image. Since the events also were seen to occur over a range of several images, the uncertainty in the temperature readings is estimated to $\Delta T_b = 6.4$°C.

Lanthanum hexaboride ($LaB_6$) was used as a calibrant for the wavelength refinement, sample to detector distance and integration in Fit2d. The wavelength was refined to be

$\lambda = 0.694118$ Å. The lattice constant was refined from high resolution data (another detector) with fixed detector distance, giving $a = 4.1564$ Å. The National Institute of Standards and Technology (NIST) standard value is 4.1569 Å. The refined value was used to refine the wavelength on station BM01A, and thereafter, the lattice constant was again refined with the PILATUS detector at two different positions, resulting in the values $a = 4.1612$ Å and $a = 4.1409$ Å for a sample-to-detector distance of 143 and 393 mm respectively. This means that data from the PILATUS detector should not be used to accurately determine cell parameters. A minimum uncertainty of $\Delta a = 0.02$ Å follows from this.

The exact details of each *in-situ* SR-PXD experiment are listed for convenience in table 4.3 and 4.4.

Table 4.3: *In-situ* SR-PXD desorption and hydrogenation experiments of $6LiBH_4 + LnCl_3$

| Sample | Experimental module and gas blower temperature $T_b$ | System pressure |
|---|---|---|
| *LaVac* | Decomposition from 35.8°C to 400°C at 5°C/min | dyn. vac. |
| | Dwelling at 400°C for 15.5 min | dyn. vac. |
| | Hydrogenation at 400°C for 31.0 min | 100 bar |
| | Cooling from 400°C to 300°C at 5°C/min | 100 bar |
| | Fast cooling from 300°C to room temperature | 100 bar |
| *LaBack* | Decomposition from 42.1°C to 400°C at 5°C/min | 5 bar |
| | Dwelling at 400°C for 15.5 min | 5 bar |
| | Hydrogenation at 400°C for 31.5 min | 100 bar |
| | Cooling from 400°C to 300°C at 5°C/min | 100 bar |
| | Fast cooling from 300°C to room temperature | 100 bar |
| *YbVac* | Decomposition from ca.30°C to 400°C at 5°C/min | dyn. vac. |
| | Dwelling at 400°C for 23 min | dyn. vac. |
| | Hydrogenation at 400°C for 24.5 min | 90-100 bar |
| | Step from 400°C to 350°C | 90-100 bar |
| | Dwelling at 350°C for 29 min | 90-100 bar |
| | Cooling from 350°C to room temperature | 90-100 bar |
| *YbBack* | Decomposition from 37°C to 400°C at 5°C/min | 6.4 bar |
| | Dwelling at 400°C for 18.5 min | 6.4 bar |
| | Hydrogenation at 400°C for 30.5 min | 100-105 bar |
| | Cooling from 400°C to 300°C at 5°C/min | 100-105 bar |
| | Fast cooling from 300°C to room temperature | 100 bar |

Some comments about the uncertainty of the pressure and temperature values given in tables 4.3 and 4.4 should be made here. For the later discussion, we will need as good error estimates as possible.

Because of a significant leak in the SR-PXD sample holder, the system had to be refilled with hydrogen gas to maintain the desired pressure. The leak rate was varying, but the change in pressure did not exceed $\frac{dP}{dt} = 5$ bar/min at 100 bar. The uncertainty in the pressure measurements at 100 bar is estimated to be ±5 bar.

No temperature calibration was undertaken for the decomposition series of *Yb*, *YbLi* and *La*, but the blower was on the other hand mounted very close to the capillary ($< 2$ mm). To get useful information out of this data, the thermal behavior of known compounds in the samples ($LiBH_4$ and LiCl) are used to fix the temperatures to a certain

Table 4.4: *In-situ* SR-PXD desorption and hydrogenation experiments of $6LiBH_4 + LnCl_3 + 3LiH$

| Sample | Experimental module and gas blower temperature $T_b$ | System pressure |
|---|---|---|
| *LaLiVac* | Decomposition from 26°C to 440°C at 5°C/min | dyn. vac. |
| | Dwelling at 440°C for 20 min | dyn. vac. |
| | Hydrogenation during cooling from 440°C to 300°C at 5°C/min | 92 bar |
| | Fast cooling from 300°C to room temperature | 92 bar |
| *LaLiBack* | Decomposition from 26°C to 440°C at 5°C/min | 5.4 bar |
| | Dwelling at 440°C for 22 min | 5.4*bar* |
| | Hydrogenation during cooling from 440°C to 340°C at 5°C/min | 90 bar |
| | Fast cooling from 340°C to room temperature | 90 bar |
| *YbLiVac* | Decomposition from 43°C to 400°C at 5°C/min | dyn. vac. |
| | Dwelling at 400°C for 33 min | dyn. vac. |
| | Hydrogenation at 400°C for 20 min | 100 bar |
| | Hydrogenation at 350°C for 7.5 min | 100 bar |
| | Fast cooling from 350°C to room temperature (no data) | 100 bar |
| | Single image at 24°C (end of cooling) | 100 bar |
| *YbLiBack* | Decomposition from 32°C to 400°C at 5°C/min | 5.6 bar |
| | Dwelling at 400°C for 27 min | 4.5 bar |
| | Hydrogenation at 400°C for 55 min | 100 bar |
| | Cooling from 400°C to 300°C at 5°C/min | 100 bar |
| | Fast cooling from 300°C to room temperature | 100 bar |

extent, although the stability of especially $LiBH_4$ may be altered by the presence of reacting/catalyzing compounds or anion substitution.

Just before the last two series were measured (*LaLiVac* and *LaLiBack*), the temperature programmed gas blower had been moved out of position, so that the actual momentary sample temperature was much lower (approx. 60%) than the set temperature of the blower. A temperature calibration of this setup confirmed this. The decomposition had only proceeded half-way, and it was decided to remeasure the sample in May 2013.

**SR-PXD, May 2013**

In this session, the wavelength was refined to $\lambda = 0.68291$ Å. The lattice constant uncertainty was still $\Delta a = 0.02$ Å. The same experimental setup was used, but this time a temperature calibration was performed before and after the measurements by melting indium ($T_{melt} = 156$°C) and tin ($T_{melt} = 232$°C) powders filled into a sapphire tube. A linear relation between the read blower temperature and the real sample temperature was assumed. This was verified by calculation of the thermal expansion coefficient for tin, which is approximately linear in the relevant temperature range. The calibration is given in equation 4.14 for the vacuum decomposition (and subsequent hydrogenation) and in equation 4.15 for the back pressure series. The calibration could be exactly reproduced after the heat blower had been elevated and lowered again.

$$T_{calib} = 0.80T_b - 3.4 \qquad [T_{calib}] = [T_b] = {}^\circ\mathrm{C} \tag{4.14}$$

$$T_{calib} = 0.84T_b - 3.5 \qquad [T_{calib}] = [T_b] = {}^\circ\mathrm{C} \tag{4.15}$$

The constants in equation 4.14 and 4.15 are in fact relative uncertain, because the ambivalent temperature in the experiment hutch could vary between 19 and 23°C, which could influence the starting sample temperature, bearing in mind the blower-sample distance of around 1.0 cm for these measurements. The temperature gradient in the area around the sample will obviously be affected from this, and the heating rate may consequently not be linear at temperatures above 232°C.

The reading uncertainty corresponds to the temperature increase during the time between each image, and is approximately ±3°C. The uncertainty due to the varying ambivalent temperature is estimated to be ±2°C. We then have a plausible error estimate of ±5°C up to 232°C, and possibly larger uncertainties at higher temperatures. To find one-to-one relations between the SR-PXD series and measured calorimetric events can help to fix the temperature somewhat better.

In the presentation of the results, we will plot the SR-PXD data against $T_{calib}$ for the $LaLi$ sample and against $T_b$ for all other samples.

### 4.2.5 Supplementary experiments, spring 2013

#### Combined DSC-TGA-RGA measurements

The four *as-milled* (a.m.) samples $La$, $LaLi$, $Yb$ and $YbLi$, the desorbed sample $YbLiBack$ and the hydrogenated $LaLiVac$, $LaLiBack$, $YbLiVac$ and $YbLiBack$ samples were studied by means of simultaneous DSC, TGA and RGA. Because some of the measurements carried out in summer 2012 showed unfinished desorption processes at 400°C, the samples were this time heated up to 500°C at a rate of 5°C/min. The balance mechanism and the sample holder were kept under flowing argon gas with flow rates of 20 ml/min and 50 ml/min respectively. The exhaust was led to the mass spectrometer and analyzed.

#### pcT measurements

The samples milled with lithium hydride were decomposed and hydrogenated in the pcT apparatus for reversibility investigations. It was desired to apply experimental conditions for the pcT measurements as similar to the ESFR experiments as possible, in order to justify comparison of these two experimental series. However, the geometry and technical properties of the tubing systems, furnace and thermometers *etc.* were necessarily different, especially the volume of the pcT sample holder, which was much bigger than the small part of the sapphire capillary exposed to the X-ray beam at ESRF. This required a larger amount of sample in the pcT experiments. Since longer desorption and absorption times are the consequences of using more material, the sample was allowed to dwell for 30 min at 400°C instead of 15-20 min and to hydrogenate at 100 bar for 24 h instead of 30 min. The heating rate of the desorption was set to exactly the same. The pressure was chosen as close as possible to the intended SR-PXD conditions. The hydrogenation temperature was chosen just below the thermodynamic event that releases hydrogen gas, but the measured temperature $T_s$ on the pcT sample holder stabilized to another temperature than was set on the furnace. A temperature dependent offset of $\pm 10 - 15$°C had to be accounted for,

and it was therefore difficult to heat the samples to exactly the desired temperatures. The experimental conditions applied in the four pcT measurements are summarized in table 4.5. Only the resulting sample temperature $T_s$ is shown. The pressure and temperature values were read every 30 s. The nominal uncertainties in the pressure and temperature readings are $\Delta T_s = 0.1$°C and $\Delta p_{sys} = 0.1$ mbar.

Table 4.5: pcT measurements of *LaLi* and *YbLi* desorbed under vacuum and back pressure.

| Sample | Experimental module and approximate sample temperature ($T_s$) | $p_{sys}$ (at module start) |
|---|---|---|
| *LaLiVac* | Decomposition from 27°C to 411°C at 5°C/min | dyn. vac. |
| | Dwelling at approximately 405°C for 30 min | dyn. vac. |
| | Fast cooling to 348°C | dyn. vac. |
| | Hydrogenation at 348°C for 24 h | 101 bar |
| | Cooling to room temperature | dyn. vac. |
| *LaLiBack* | Decomposition from 24°C to 411°C at 5°C/min | 5.9 bar |
| | Dwelling at approximately 405°C for 30 min | 8.6 bar |
| | Fast cooling to room temperature (Investigation of powder) | vac. |
| | Fast heating to 355°C | vac. |
| | Hydrogenation at 349 (start at 355°C) for 24 h | 103 bar |
| | Cooling to room temperature | dyn. vac. |
| *YbLiVac* | Decomposition from 24°C to 427°C at 5°C/min | dyn. vac. |
| | Dwelling at approximately 425°C for 30 min | dyn. vac. |
| | Fast cooling to 377°C | dyn. vac. |
| | Hydrogenation at 371°C (start at 377°C) for 24 h | 102 bar |
| | Cooling to room temperature | dyn. vac. |
| *YbLiBack* | Decomposition from 25°C to 435°C at 5°C/min | 5.5 bar |
| | Dwelling at approximately 427°C for 30 min | 8.0 bar |
| | Fast cooling to room temperature (Investigation of powder) | vac. |
| | Fast heating to 378°C | vac. |
| | Hydrogenation at 368°C (start at 378°C) for 24 h | 101 bar |
| | Cooling to room temperature | dyn. vac. |

Before conducting each experiment, the sample holder was evacuated until a pressure below $5 \cdot 10^{-6}$ mbar was reached, in order to ensure that all connections were sufficiently tightened.

### Lab-PXD Measurements

All samples were investigated with the Bruker AXS D8 Advance diffractometer. It uses a copper anode with a wavelength doublet ($Cu - K_{\alpha 1,\alpha 2}$) with $\lambda_1 = 1.54056$ Å and $\lambda_2 = 1.5444$ Å for $K_{1\alpha}$ and $K_{2\alpha}$ respectively. The weighted mean wavelength $\bar{\lambda} = \frac{2\lambda_1+\lambda_2}{3} = 1.54184$ Å was used in the calculations. Scan speeds varying from 2-4 sec/step and step lengths of ca. 0.019° were chosen. Each scan required in this way at least 2 h to complete, and often more, depending on the chosen $2\theta$ range.

### IR Measurements

A.m. $LaLi$, a.m. $YbLi$, $LaLiBack$, $YbLiBack$ and all the four pcT-hydrogenated samples were measured with a Bruker ALPHA FT-IR spectrometer. An attenuated total reflection (ATR) module utilizing a single diamond crystal was used. 24 scans with resolution 2 $cm^{-1}$ were made of each sample.

# Results

In the presentation of the results, we will bear in mind the two central questions that are to be answered: 1. Is the proposed recipe outlined in section 3.2.4 for *in-situ* synthesis of destabilizing rare-earth hydrides applicable also for the corresponding lanthanum and ytterbium systems? 2. If so, do these systems perform as well as the reported cerium hydride composite with respect to hydrogen storage and sorption properties? What are the advantages/disadvantages compared to the samples where a major part of the hydrogen is bounded as mixed-metal borohydrides?

Answering the first question will mainly be accomplished in section 5.2 by qualitative and quantitative analyses of the *as-milled* $La/Yb$ and $LaLi/YbLi$ samples. The main tool will be Rietveld refinement of synchrotron X-ray diffraction data which will deliver a relatively reliable estimate for the composition of crystalline phases. The amount of gas released during milling will be determined by pressure- and temperature monitored ball-milling.

The second question will be answered by considering DSC-TGA-RGA and SR-PXD data of *in-situ* desorption (section 5.3) and hydrogenation (section 5.4) experiments of all the samples. The 5.4.2 hydrogenation experiments will also elucidate the sorption and storage properties.

The important findings will be summarized and treated further in the discussion. But firstly, the results from the investigations of the starting materials $LiBH_4$, LiH and $LnCl_3$ (Ln=La, Yb) will be presented.

## 5.1 Starting materials

### 5.1.1 Lithium borohydride

#### Synchrotron X-ray diffraction

The refined SR-PXD scan at room temperature of 95% pure $LiBH_4$ and Si powder hand-mixed in a weight ratio of 1:0.053 is shown in figure 5.1. The black crosses are observed data points, the red solid line is the calculated pattern and the blue solid line at the bottom is the difference between the two. The pattern was refined in GSAS, with the atomic arrangement from reference [29] as a first trial. The lattice parameters, phase fractions (relative scaling), zero point offset and a Shifted Chebyschev background polynomial with 18 terms were refined for all phases including $LiBH_4$, LiCl and Si. For the two former, all thermal displacement parameters and profile parameters $G_u$, $G_v$, $G_w$, $L_x$ and $L_y$ were refined. The profile parameters for LiCl were manually found, because of very weak intensities. For $LiBH_4$, also all the atomic positions were refined. Convergence was reached with $R_{wp} = 3.16\%$, $R_p = 1.94\%$. The good fit clearly reflects the fact that there

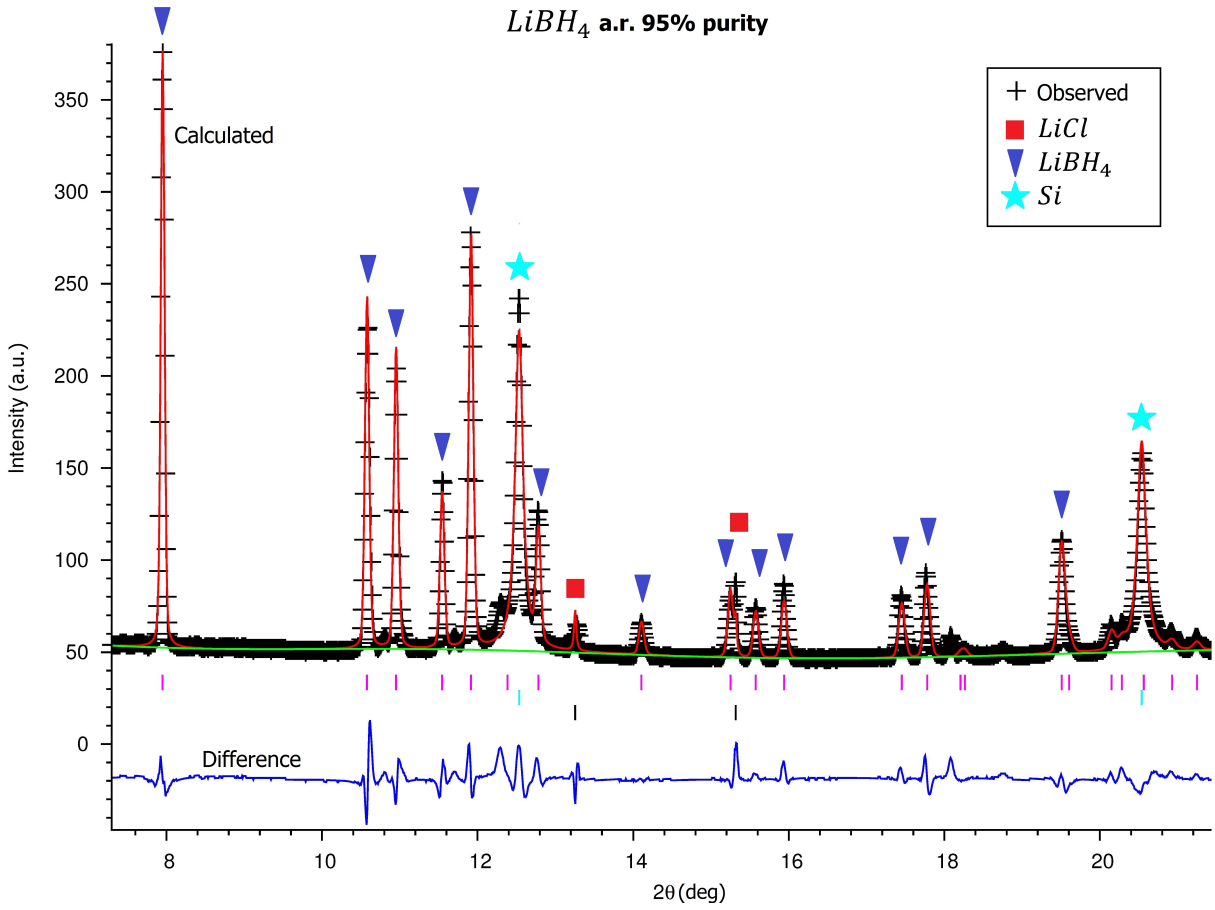


Figure 5.1: SRPXD of 95% pure $LiBH_4$ with Si powder as internal reference. $\lambda = 0.68291$ Å.

were few and known compounds in the sample. The lattice constants and molar fractions are shown in table 5.1.

Table 5.1: Refined lattice parameters of identified phases in the *as-received* $LiBH_4$ batch measured at room temperature.

| Phase | Space group | $a$(Å) | $b$(Å) | $c$(Å) | Molar fraction (mol%) |
|---|---|---|---|---|---|
| $ortho - LiBH_4$ | $Pnma$ | 7.156(4) | 4.417(6) | 6.790(3) | 91.38 |
| $Si$ | $Fd\bar{3}m$ | 5.417(6) | | | 8.36 |
| $LiCl$ | $Fm\bar{3}m$ | 5.124(2) | | | 0.26 |

The lattice constant for silicon fits very well the NIST standard value ($a = 5.43119(5)$ Å[49]). This means that the lattice constants for this $LiBH_4$-batch are correct within three significant digits. They all fall in the expected range when compared with table 3.2. The calculated amount of impurities, LiCl included, is the nearly the double of what was stated from the provider.

The refinement did not include an explanation for the additional small peaks visible at $2\theta = 10.8, 11.7$ and $12.3°$. They can be explained with a hexagonal unit cell with space group $P6_3mc$ and lattice constants $a = 4.187$ Å and $c = 6.694$ Å. Although $hex - LiBH_4$ has exactly this unit cell, are the lattice parameters significantly bigger, even with a 50%

chlorine substitution (table 3.2). Also, this phase is not supposed to form only by applying mechanical force to the powder.

### IR spectroscopy

The infrared spectrum of lithium borohydride has been thoroughly examined by McQuaker [56], Zavorotynska et al.[57] among others. In these previous studies, factor group analysis and DFT calculations were used to assign the vibrational modes to the observed peaks. The $LiBH_4$ sample studied in the present work is shown in figure 5.2, and the spectrum is very equal to that recorded by McQuaker. The latter was measured at -193°C and many peaks were therefore sharper (less thermal vibration).

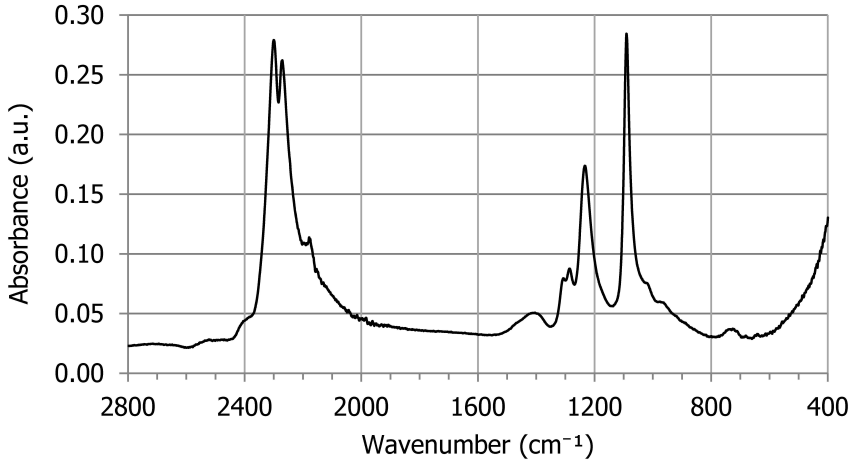


Figure 5.2: Room temperature IR spectrum of 95% pure $LiBH_4$

The lowest frequencies (below 1600 $cm^{-1}$) correspond to bending region of the $[BH_4]^-$ groups in $LiBH_4$, and the highest frequencies correspond mainly to the stretching region of the $[BH_4]^-$ groups. The IR peaks are assigned to the stretching ($\nu_3$) and bending ($\nu_2$, $\nu_4$) vibrational modes by comparing the spectrum with the previous works. To arrive at the correct assignments, one can consider the factor and site group symmetries of the molecule and arrive at the corresponding irreducible representations, to be able to set up a Hessian matrix and calculate the normal modes. This however exceeds the scope of this work. The results are shown in table 5.10 in section 5.4.2 together with the results from the *LaLi* and *YbLi* samples. Frequencies labeled with one inverted comma have A′ symmetry, and those marked with two inverted commas have A″ symmetry. The former symmetry species is symmetric with respect to $\sigma_d$, and the latter is antisymmetric with respect to $\sigma_d$. $\sigma_d$ is the symmetry element of improper rotation of the $T_d$ point group of the free $[BH_4]^{-1}$ tetrahedron[58]. No translatory modes are presented since these fall outside the wavenumber domain (below 400 $cm^{-1}$).

### DSC-TGA measurements

The results from the DSC-TGA measurement of pure $LiBH_4$ are shown in figure 5.3. The sample was heated to 500°C with a rate of 5°C/min.

The first endothermic peak at 115.5°C comes from the orthogonal to hexagonal phase transition mentioned in section 3.2.3. The temperature for this event reported in reference [36] is 107°C. However, the temperature ramp this group used was 10°C/min and the

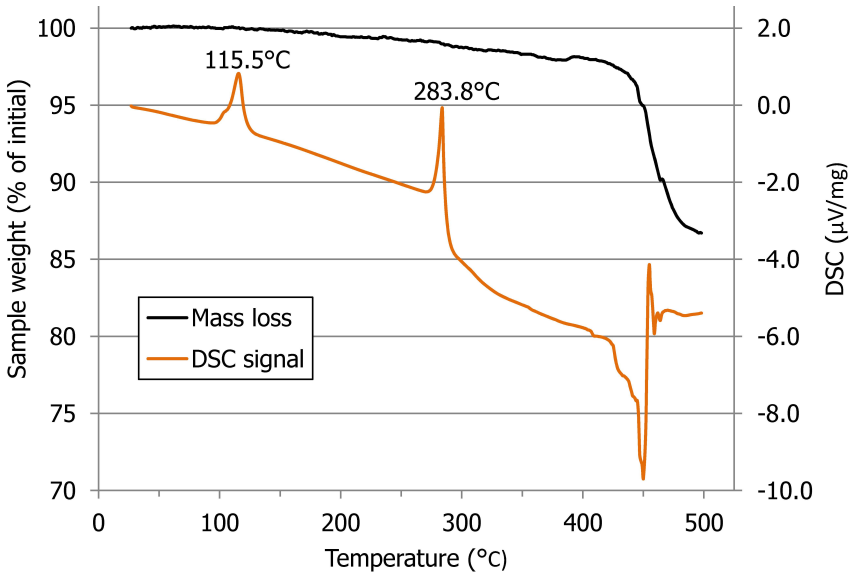


Figure 5.3: DSC-TGA curves of 95% pure $LiBH_4$. Heat rate: 5°C/min.

ambient atmosphere was hydrogen at atmospheric pressure, so the comparison basis is not optimal. The next endothermic peak belongs to the melting of $LiBH_4$, and the measured temperature, 283.8°C falls in the expected region and deviates only little from the reported 280°C. The decomposition temperature and consequently following gas release is indicated by the TGA trace, which shows a weight loss of 11.4 wt% between $400 - 500$°C, in accordance to previous reports (see section 3.2.3). The DSC trace is spoiled in this region due sensor contamination by foaming $LiBH_4$.

Since the chemical reaction and consequently the DSC trace obviously depend on heating rate, atmosphere and batch quality, and since calibration methods and/or sensors can influence the trace as well, the values from the present measurement of $LiBH_4$ will be used as basis for later analyses.

### 5.1.2 Lithium hydride

*As-received* lithium hydride (95% purity) was investigated with lab-PXD. The major contribution was from the $Fm\bar{3}m$ phase of LiH, but remnants of $Li_2O$ and LiOH were also identified by searching in the ICDD database. The three phases were imported GSAS together with the diffraction pattern and some cycles were run (convergence with $R_{wp} = 13.4$ and $R_p = 10.4$), just in order to get an approximate calculation of the composition of the sample. The batch contained 94.9 wt% LiH, 3.6 wt% $Li_2O$ and 1.5 wt% LiOH, in agreement with the purity claimed by the provider.

### 5.1.3 Rare earth chlorides

The two rare earth chlorides used in this work were ordered in several batches (all with purity 99.99%) and different starting materials have been used for different samples. All the batches were controlled by comparing the lab-PXD diffraction patterns of $LaCl_3$ and $YbCl_3$ visually with the published patterns found in the ICDD database. No contaminating phases where found, but the reported peak intensities for ytterbium chloride deviated slightly from the ones measured.

## 5.2 Synthesis of the composites

Although nothing is reported on the exact composition $6LiBH_4 + LnCl_3$ (Ln = La, Yb), the very similar systems $3LiBH_4 + LnCl_3$ (Ln = La, Yb) as well as $6LiBH_4 + LnCl_3$ (Ln = Ce, Gd) and $6LiBH_4 + CeCl_3 + 3LiH$ have been investigated and have been presented in section 3.2.4. It is expected that the present experiments will exhibit similar properties as has been observed for these systems. There will most probably be developed common phases in the systems with the same rare earth chloride but different molar ratios, and the rare-earth containing phases are expected to be similar for different rare earth elements, because of similar chemical properties. That is, the reported $LiCe(BH_4)_3Cl$ phase may very well also be developed in the *LaLi* sample, only with lanthanum instead of cerium: $LiLa(BH_4)_3Cl$.

Furthermore, it is *a priori* expected that the proposed metathesis reactions that produces the intermediate cerium borohydride (equation 3.25) and thereafter the cerium hydride (equation 3.26) also takes place for the corresponding lanthanum and ytterbium systems, only corrected with the right rare-earth borohydride intermediate:

$$6LiBH_4 + LnCl3 \rightarrow LiLn(BH_4)_3Cl + 2LiCl + 3LiBH_4 \qquad (Ln = La, Yb) \tag{5.1}$$

$$LiLn(BH_4)_3Cl + 2LiCl{+}3LiBH_4{+}3LiH \rightarrow 3LiCl{+}6LiBH_4{+}LnH_{2+\delta} + \frac{1-\delta}{2}H_2 \ (Ln = La, Yb) \tag{5.2}$$

The molar fractions of the reaction compounds of the first (5.1) and second (5.2) expected metathesis reactions will be compared with observed values in the following four sections.

The PXD measurements of both the new and old *La*, *Yb* and *YbLi* samples will be presented, in order to elucidate equalities or inequalities which can hamper the later comparative analyses. The container used to transport the 2012 samples back to Norway after the measurements at ESRF was not tight, so the single sample vials were exposed to air. These small vials were sealed with Parafilm, but oxygen diffusion can still not be disregarded, and they were therefore measured again with lab-PXD in 2013, so they could be used for further analysis (including pcT and IR measurements). Naturally, the SR-PXD scans of the old samples will serve as basis for quantitative phase fraction determinations.

### 5.2.1 $6LiBH_4 + LaCl_3$ sample composition

In figure 5.4, the SR-PXD and lab-PXD measurements (lower and middle curve respectively) of the 2012 *La* sample are compared with a lab-PXD scan of the new 2013 *La* sample. They are plotted against the $\Delta k$ axis, which allows patterns measured at different wavelengths to be compared. The old and new *La* samples should be identical, since exactly the same milling parameters were chosen (section 4.2.2). However, at a first glance, this seems not to be the case.

In the old *La* sample, there is a phase present (green triangle markers) which was found to be isostructural to the cubic $I\bar{4}3m$ phase of $LiCe(BH_4)_3Cl$. By exchanging the cerium atoms with lanthanum, giving $LiLa(BH_4)_3Cl$, this phase gave a perfect fit with the measured pattern in the refinement discussed below. Remnants of unreacted $LaCl_3$ (brown circle markers) with the hexagonal $P6\frac{3}{m}$ space group was detected. For

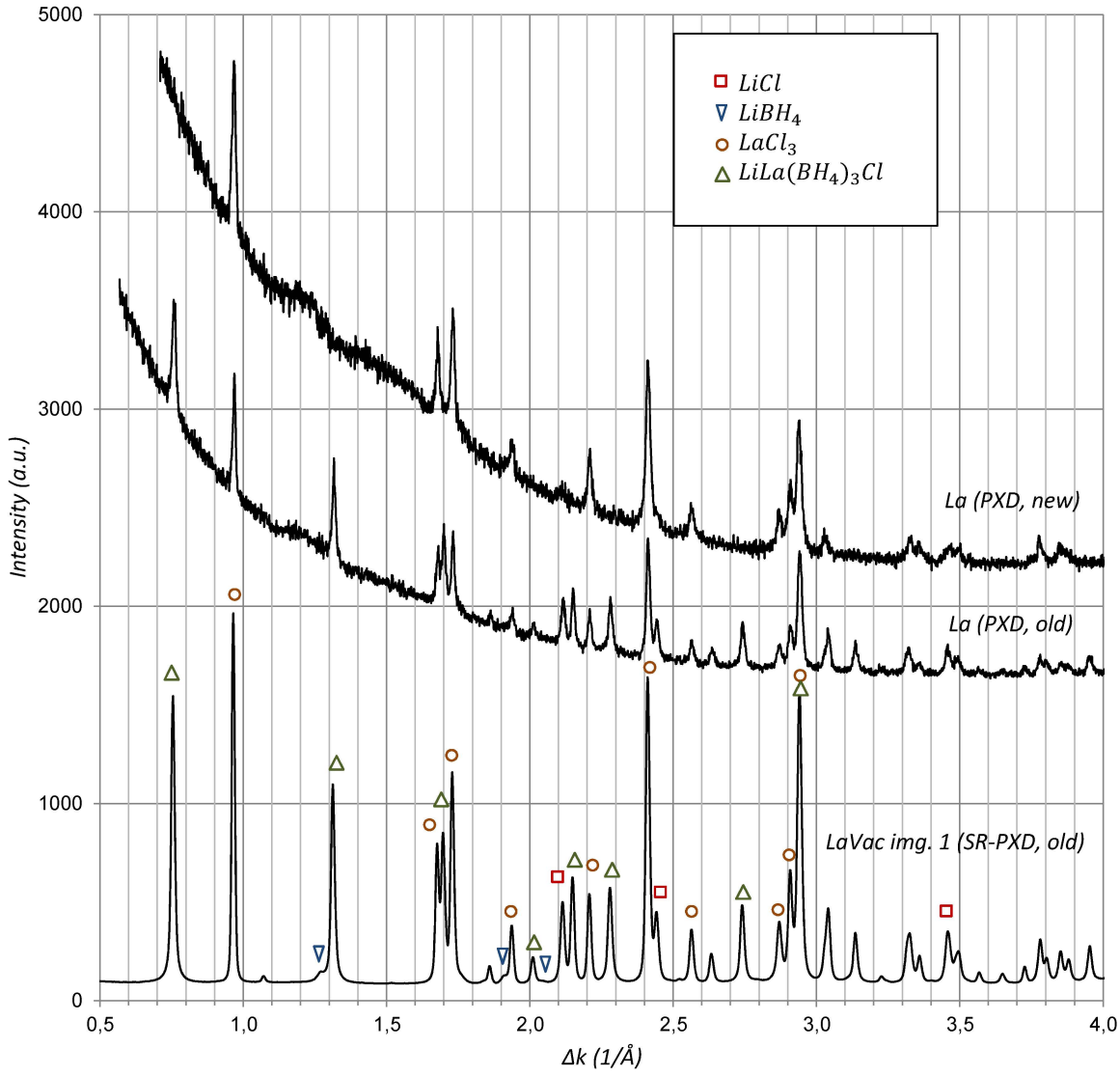


Figure 5.4: Upper scan: Lab-PXD of the 2013 a.m. *La* sample
Middle scan: Lab-PXD of the 2012 a.m. *La* sample
Lower scan: 1st SR-PXD image of the 2012 a.m. *La* sample

the new batch, however, $LiLa(BH_4)_3Cl$ did not crystallize. It is most probably still there, only in an amorphous state. The rise of the background around $\Delta k = 1.1 - 1.3$ in the upper PXD scan indicates that there are more amorphous material in the new sample. Another argument for this is that the DSC traces of the two samples are almost equal (see next section). Peaks from orthorhombic $LiBH_4$ are observed for both samples in the high resolution SR-PXD scan. Lithium chloride (red square markers) is present in every *as-milled* sample.

To say something quantitatively about the molar ratios in the sample, a Rietveld refinement of the SR-PXD scan in figure 5.4 was performed with GSAS. The four phases in figure 5.4 were included, and the phase fractions, lattice constants, zero-point offset and 24 terms of a Shifted Chebyschev background polynomial were refined for all phases. The profile parameters $G_u$ and $L_x$ were refined for $LaCl_3$ and $LaLi(BH_4)_3Cl$ and $L_x$ was refined for LiCl. Refinement of more profile parameters and thermal displacement factors

resulted in divergence in these values. The not-refined $G_u$ and $L_x$ parameters were set to values that visually gave a good fit, and the thermal displacement factors were set to the standard value. The refinement gave a $R_{wp} = 6.77\%$, $R_p = 5.02\%$ for 41 variables (including the background polynomial). The resulting refinement plot of the calculated and observed pattern is attached in appendix B (figure B.1). The refined phase fractions and molar ratios are shown in table 5.2. Column four and five show the refined and expected (equation 5.1) molar fractions of each compound. The standard deviation of the weight fraction value ($\sigma_f$) determined by the program gives a hint of the uncertainties in the refinement, but it was observed that for example changing the number of terms in the background polynomial could give a weight fraction $f$ far outside the range indicated by $\sigma_f$, with an experience-estimated relative error of $\frac{\Delta f}{f} = 5\%$.

Table 5.2: Chemical composition of the *La* sample by Rietveld refinement.

| Phase | Refined fraction (wt%) | $\sigma_f$ (wt%) | Molar weight (g/mol) | Refined fraction (mol%) | Expected fraction (mol%) |
|---|---|---|---|---|---|
| $ortho - LiBH_4$ | 19.9 | 1.5 | 21.78 | 57.6 | 50.0 |
| $LaCl_3$ | 39.3 | 0.11 | 245.26 | 10.1 | 0.0 |
| LiCl | 17.3 | 0.25 | 42.39 | 25.7 | 33.3 |
| $LiLa(BH_4)_3Cl$ | 23.5 | 0.11 | 225.83 | 6.6 | 16.7 |

As was qualitatively seen in figure 5.4, the refinement confirms that there are still a large portion of $LaCl_3$ present in the sample, and there are lesser reaction products formed as a cause of this. Since this sample proved to be partially unreacted, one can ask why this sample was chosen to be studied. The answer is that the *LaLi* sample exhibited a quite different decomposition pathway than *La*, and had a confined and quick release of hydrogen, as opposed to *La*, which decomposes much slower and moreover in several steps. In total, the lanthanum samples proved to exhibit similar properties as the previously studied cerium composites discussed in section 3.2.4, which we will come to later.

### 5.2.2 $6LiBH_4 + YbCl_3$ sample composition

Prior to PXD analysis, the old and new *Yb* samples were not expected to be completely equal, because the new *Yb* sample was milled at a higher speed (400 rpm) than the old sample (310 rpm). The fact is, they are actually very similar, at least from a first glance at the diffraction patterns in figure 5.5. The SR-PXD and lab-PXD scans of 2012 *Yb* are displayed at the bottom and in the middle, and the lab-PXD scan of the 2013 *Yb* at the top. There is a difference, however: The trivalent ytterbium borohydride $LiYb(BH_4)_3Cl$ phase is present in both samples, but the divalent ytterbium borohydride $Yb(BH_4)_{2-x}Cl_x$ (black crosses) is only present in the 2012 sample. The lab-PXD scan of the 2012 sample (measured after transportation) also shows that the peak intensity of $LiYb(BH_4)_3Cl$ has been weaken relative to LiCl, which indicates that this borohydride is unstable and/or has been exposed to small amounts of oxygen.

A quantitative determination of weight and molar fractions of the composites was again achieved by refining the SR-PXD data. All four compounds identified in figure 5.4 were included, and the phase fractions, lattice constants, zero-point offset and 36 terms

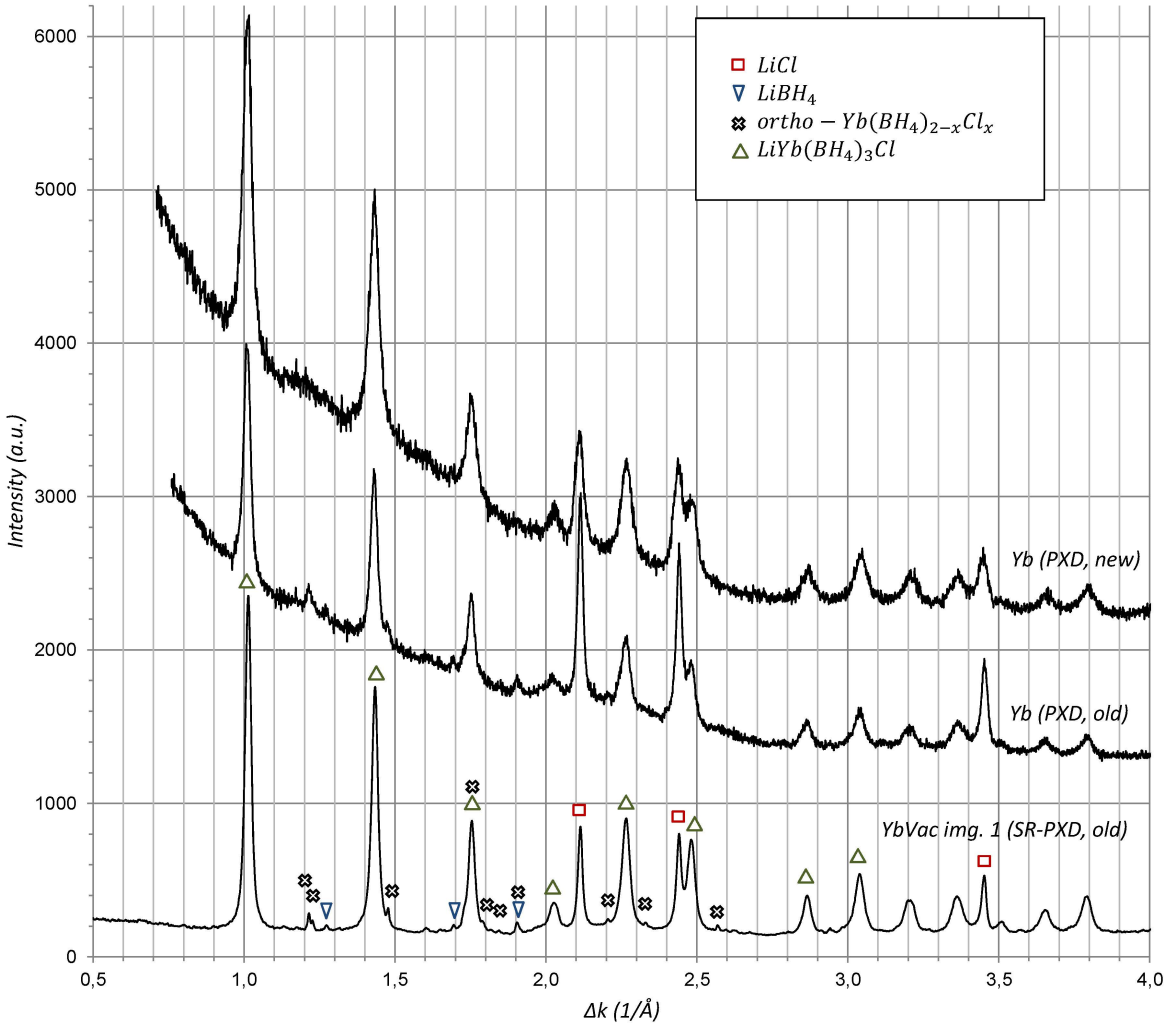


Figure 5.5: Upper scan: Lab-PXD of the 2013 a.m. $Yb$ sample
Middle scan: Lab-PXD of the 2012 a.m. $Yb$ sample
Lower scan: 1st SR-PXD image of the 2012 a.m. $Yb$ sample

of a Shifted Chebyschev background polynomial were again refined for all phases. $G_u$ and $L_x$ were refined for all phases but $LiBH_4$. Thermal displacement factors were only found to converge into physically meaningful values for LiCl, and they were set to the standard value for all other phases. The degree of chlorine substitution in $Yb(BH_4)_{2-x}Cl_x$ was not refined, since the intensity of this phase was too low to allow for convergence of this parameter, and $x$ was set to 0.3, as was found in reference [42]. The refinement converged with $R_{wp} = 4.35\%$, $R_p = 3.32\%$ for 50 variables. The fractions are listed in table 5.3. The refinement plot is attached in appendix B (figure B.2).

It is seen that the amount of $LiBH_4$ this time is much lower than expected from equation 5.2. The amount of $LiBH_4$ is also the most uncertain, indicated by $\sigma_f$, because of the low intensity of this phase, but the deviation from the expected fraction cannot be explained by this alone. One possibility is that some $LiBH_4$ has been amorphisated. Another explanation is that the first metathesis reaction has already completed and that the products, the ytterbium borohydrides, are partially decomposed again during milling, producing more LiCl, amorphous ytterbium compounds and hydrogen or diborane gas.

There is at least no ytterbium chloride present, and the amount of rare earth borohy-

Table 5.3: Chemical composition of the $Yb$ sample by Rietveld refinement.

| Phase | Refined fraction (wt%) | $\sigma_f$ (%) | Molar weight (g/mol) | Refined fraction (mol%) | Expected fraction (mol%) |
|---|---|---|---|---|---|
| $ortho - LiBH_4$ | 11.5 | 0.79 | 21.78 | 30.3 | 50.0 |
| LiCl | 42.9 | 0.17 | 42.39 | 58.1 | 33.3 |
| $LiYb(BH_4)_3Cl$ | 43.8 | 0.066 | 225.83 | 11.1 | 16.7 |
| $Yb(BH_4)_{1.7}Cl_{0.3}$ | 1.77 | 0.059 | 208.90 | 0.5 | 0.0 |

drides is higher here than in the $La$ sample. This proves that reaction 5.1 has proceeded further in the $Yb$ case. This effect, namely that heavier rare-earth elements require shorter milling times to form new borohydrides from $LiBH_4$, was also discovered for potassium borohydride and rare earth chlorides in the specialization project accomplished by the author last fall, and was explained by the different ionic radii of the elements. It was therefore no surprise that the $La$ sample had reacted lesser than the $Yb$ sample after the same amount of time.

Another, practical feature concerning the 2013 $La$ and $Yb$ samples should be mentioned: When the milling vials were opened in the glovebox, there was a distinct difference in the consistence of the $La$ and $Yb$ powders. Whereas the $Yb$ sample was fluffy, dry and clear off the walls, the $La$ sample was compressed and smeared out onto the walls and was hard to scratch off. It is difficult to deduce physical results from these observations, but there must necessarily have been different centrifugal forces and strain acting on the two samples, and better mixing is assumed to have taken place in the $Yb$ case. Also, a significant response in the oxygen sensor level was observed right after the vials were opened. If the vials were tight, this will mean that hydrogen or diborane gas was produced during milling.

### 5.2.3 $6LiBH_4 + LaCl_3 + 3LiH$ sample composition

No new batch of $LaLi$ sample was made, because the sample from summer 2012 was well preserved, proved by PXD and DSC-TGA measurements. The first SR-PXD scan of this sample from the vacuum decomposition at room temperature is shown in figure 5.6, and the known phases are marked.

Table 5.4: Chemical composition of the $LaLi$ sample by Rietveld refinement.

| Phase | Refined fraction (wt%) | $\sigma_f$ (wt%) | Molar weight (g/mol) | Refined fraction (mol%) | Expected fraction (mol%) |
|---|---|---|---|---|---|
| $ortho - LiBH_4$ | 44.8 | 1.4 | 21.78 | 73.4 | 60.0 |
| $LaCl_3$ | 25.3 | 0.096 | 245.26 | 3.7 | 0.0 |
| LiCl | 26.7 | 0.20 | 42.39 | 22.4 | 30.0 |
| $LiLa(BH_4)_3Cl$ | 3.21 | 0.040 | 225.83 | 0.5 | 0 |
| $LaH_{2+\delta}$ | 0 | 0 | 140.92 ($\delta = 0$) | 0.0 | 10.0 |

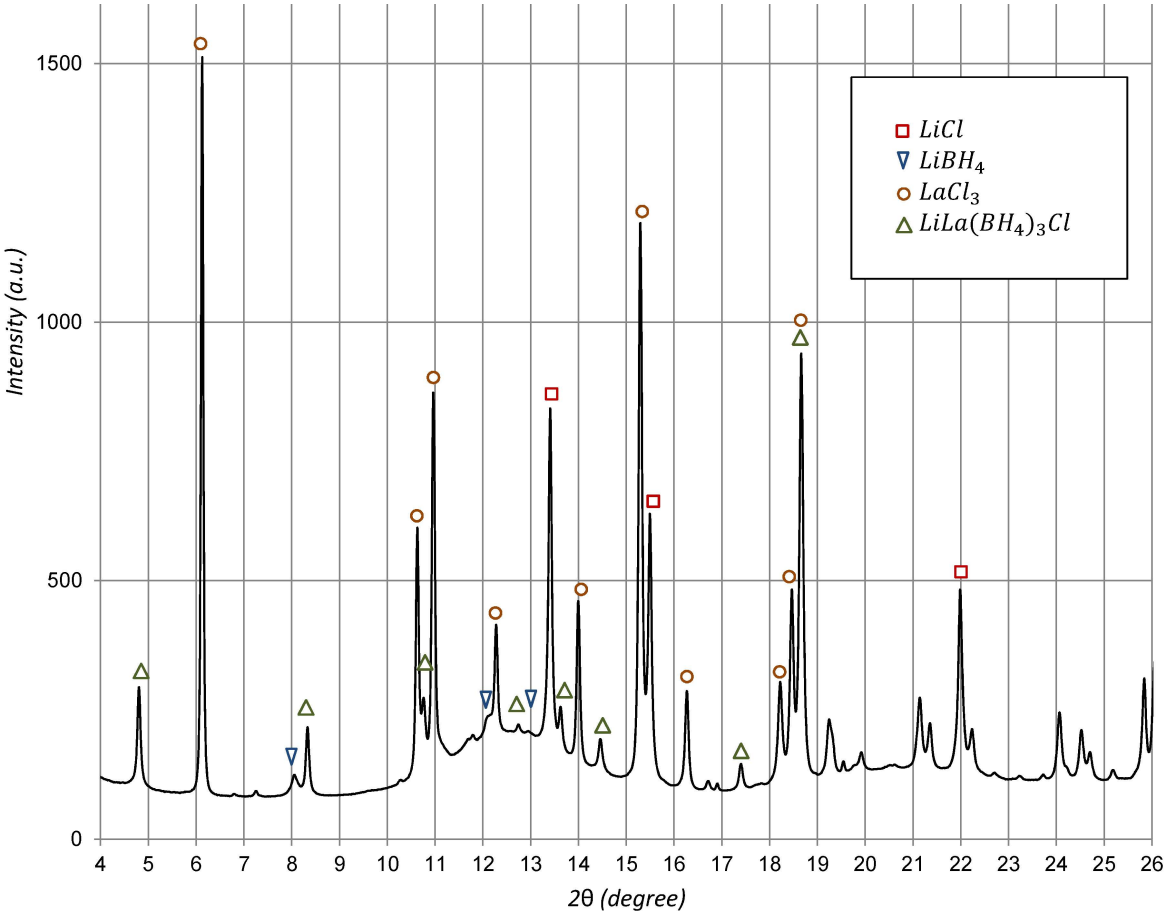


Figure 5.6: SR-PXD scan of the a.m. 2012 *LaLi* sample at room temperature.

Similarly to the a.m. *La* sample, *LaLi* contained LiCl, $LaCl_3$ $LiLa(BH_4)_3Cl$ and $LiBH_4$, only in slightly different amounts, although the compounds on the right side of equation 5.2 rather was expected. Attempts to include the cubic phase of $LaH_{2+\delta}$ in the refinement did not give a reasonable fit, and this phase is most probably not present, at least not crystalline. The four identified phases were included and the fractions, lattice constants and the zero-point offset were refined. The background was selected manually, due to large variations. The displacement parameters converged into physically meaningful values for LiCl and $LaCl_3$. $G_u$ and $L_x$ were refined for all phases except $LiBH_4$. The refinement converged with $R_{wp} = 4.19\%$, $R_p = 2.39\%$. The calculated weight and molar fractions of these four phases are given in table 5.4. The refinement plot is attached in appendix B (figure B.3).

When the values in table 5.4 are compared to the molar ratios calculated for the *La* sample (table 5.2), the following conclusions can be drawn: The refined values indicate much more $LiBH_4$ after the second milling, and if they are reliable, this means that reaction 5.2 has proceeded partially. Only partially, because no $LaH_{2+\delta}$ is formed yet. This suggests that equation 5.2 is a multi-step reaction in the lanthanum case. If the estimated $LiBH_4$ content is wrong, and closer to the first value (19.9 wt%), we can still predict the chemistry from the three more reliable estimates (referring to the $\sigma_f$ values in table 5.4). In table 5.5, it is shown that the amount of $LiLa(BH_4)_3Cl$ is reduced much more in the second milling than $LaCl_3$ and LiCl. This means that once LiH has been added, reaction 5.2 is more easily commenced than the continuing of reaction 5.1.

Table 5.5: Compared molar ratios from the *La* and the *LaLi* samples

| | *La* | *LaLi* |
|---|---|---|
| $LaCl_3$ : $LiLa(BH_4)_3Cl$ | 1.54 | 7.28 |
| $LiCl$ : $LiLa(BH_4)_3Cl$ | 3.92 | 44.3 |

### 5.2.4 $6LiBH_4 + YbCl_3 + 3LiH$ sample composition

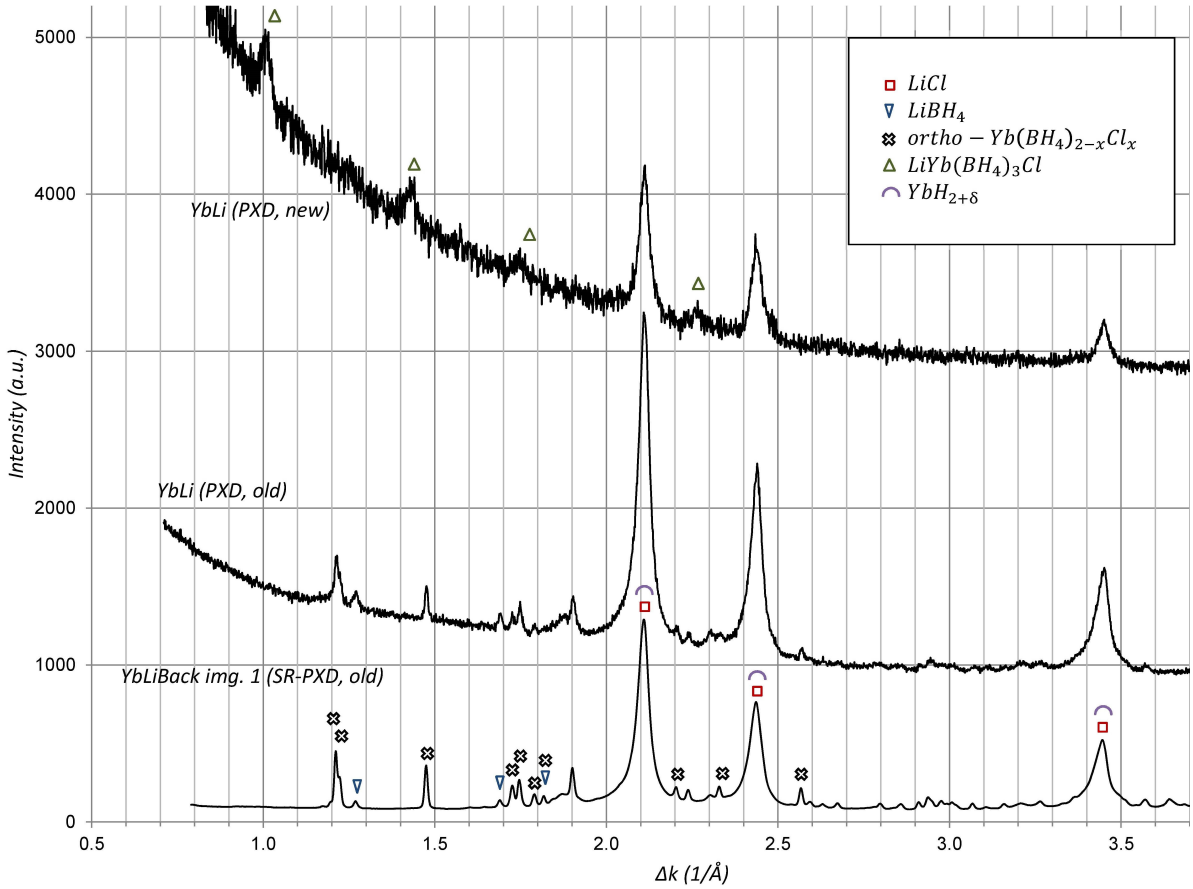


Figure 5.7: Upper scan: Lab-PXD of the 2013 a.m. *YbLi* sample
Middle scan: Lab-PXD of the 2012 a.m. *YbLi* sample
Lower scan: 1st SR-PXD image of the 2012 a.m. *YbLi* sample. The first images from the vacuum and back pressure desorption were exactly the same.

In figure 5.7, the PXD and SR-PXD scans of *YbLi* are shown. In the 2012 sample, $Yb(BH_4)_{2-x}Cl_x$ was still there after the second milling, but the trivalent $LiYb(BH_4)_3Cl$ phase was gone. In the 2013 *YbLi* sample, however, there is still some $LiYb(BH_4)_3Cl$ left, although it has been drastically reduced in intensity compared to the *Yb* sample. Because of high signal-to-noise ratio, the divalent phase as well as lithium borohydride are hard to identify in the 2013 sample from the present data.

The non-Gaussian shape of the strong peaks at the LiCl positions suggests that another cubic phase with same lattice constant but different FWHM is overlapping. Actually, the expected $Fm\bar{3}m$-phase of $YbH_{2+\delta}$ has lattice constant $a = 5.192$ Å, which is very similar to the lattice constant of LiCl.

A Rietveld refinement in GSAS was again carried out. Firstly, the FCC phase of LiCl was included, but the relative peak intensity did not match very well. The first and the fourth peak in the pattern were too intense, and the second too weak. Thereafter, the almost totally overlapping FCC $YbH_{2+\delta}$ was added instead, and this pattern matched slightly better, but a mismatch of the opposite kind was quite distinct to recognize. That is, the first and the fourth peak were slightly to high, whereas the second too weak. This strongly supports that both of the compounds were present in the sample.

The two phases mentioned above were refined together with orthorhombic $LiBH_4$ and orthorhombic $Yb(BH_4)_{2-x}Cl_x$. The divalent ytterbium borohydride phase is a very strong scatterer and was easy to identify (black crosses in figure 5.7). The substitution modification $Yb(BH_4)_{1.7}Cl_{0.3}$ was also this time found to give a good fit, although the substitution degree was not refined. A very few additional peaks could not be identified. The background was selected manually. The lattice parameters, the phase fractions and the zero point offset were refined for all phases. $G_u$ and $L_x$ for $Yb(BH_4)_{2-x}Cl_x$, LiCl and $YbH_{2+\delta}$ were refined, for the two latter however not simultaneously. The displacement factors were refined only for LiCl. The system did easily diverge if more parameters were refined. The refinement should however suffice to give a rough estimate of the chemical composition in the sample. The refinement plot is attached in appendix B (figure B.4). Convergence under the above conditions was achieved with a $R_{wp} = 5.59\%$ and $R_p = 4.17\%$, yielding the following composition:

Table 5.6: Chemical composition of the $YbLi$ sample by Rietveld refinement.

| Phase | Refined fraction (wt%) | $\sigma_f$ (wt%) | Molar weight (g/mol) | Refined fraction (mol%) | Expected fraction (mol%) |
|---|---|---|---|---|---|
| $ortho - LiBH_4$ | 0.322 | 0.0085 | 21.78 | 61.3 | 60.0 |
| LiCl | 0.311 | 0.0032 | 42.39 | 30.3 | 30.0 |
| $Yb(BH_4)_{1.7}Cl_{0.3}$ | 0.085 | 0.00058 | 202.73 | 1.7 | 0.0 |
| $YbH_{2+\delta}$ | 0.3256 | 0.0011 | 0.282 ($\delta = 0$) | 6.7 | 10.0 |

The agreement with the expected sample composition is astonishing good, with the exception of ytterbium hydride, for which the fraction was especially hard to determine because of the overlapping with LiCl. There were very little ytterbium borohydride left in the sample, and all the trivalent ytterbium borohydride has reacted, as opposed to the lanthanum case. Also the massive increase of $LiBH_4$ content is in accordance with what is expected. Together, this proves that the second metathesis reaction (equation 5.2) for $Ln = Yb$ has been fully initiated once LiH is added. The unexpected ratio of 1.92:1 for LiCl and $LiBH_4$ in the $Yb$ sample discussed previously does not seem to hamper the reaction much. Also in table 5.6, the uncertainty of the $LiBH_4$ content is the biggest. What is however noteworthy, is that the small amounts of divalent ytterbium borohydride do not really take part in the reaction. The calculated molar percentage actually increases from 0.5 to 1.7%, probably due to the reduction of trivalent into divalent ytterbium borohydride (reaction 5.7) discussed in section 3.2.4. This important detail will be explored further.

In table 5.7, the expected molar ratios according to right side of equation 5.2 are compared with the ratios emerging from table 5.6.

The ratios here do in fact reinforce the good fit in table 5.6, although the three last values deviate slightly: Normally, the given amount of rare-earth containing compounds

Table 5.7: Molar ratios of the compounds in $YbLi$ from expected reaction pathway and refinement

| Compounds/elements | Refined molar ratio | Expected molar ratio |
|---|---|---|
| $LiBH_4 : LiCl$ | 2.02 | 2 |
| $LiCl : YbH_{2+\delta}$ | 4.54 | 3 |
| Li : Yb | 10.89 | 9 |
| Cl : Yb | 3.60 | 3 |

is underestimated, because these heavy atoms have high X-ray absorption which is dependent on the wavelength and other parameters. This explains the discrepancy in the $LiCl : YbH_{2+\delta}$, Li : Yb and Cl : Yb ratios. Also, the chlorine substitution in ytterbium borohydride is not refined, although this would have a small effect due to the low molar ratio of this phase.

We will preliminary conclude that the ytterbium system tends to follow the proposed equation much better than the lanthanum system studied here. The last unknown in equation 5.2, namely the hydrogen gas, remains to be quantified. Gas- and temperature-monitored ball-milling of the same samples will be an important tool in order to assess the nature of the process.

### 5.2.5 Pressure- and temperature monitored ball-milling

All the four samples were milled in the Fritsch Pulverisette 6 ball mill which allowed for a tracking of the temperature and pressure inside the sealed vial. The results are all shown in figure 5.8. The thermal energy developed as a cause of friction and deformation results in a temperature and consequently pressure rise for all samples. However, when the milling was ended (seen in the figures after 5 h for $Ln$ and 1 h for $LnLi$), stationary conditions were achieved after some time, and the pressure generated from this thermal energy asymptotically decreased, until it was almost constant. For the moderate conditions in these experiments, the gas should not behave much different than an ideal gas. Still, the compressibility $Z(p,T)$ of hydrogen (equation 4.2) was embedded in the gas law (equation 5.3) to minimize errors.

$$n = \frac{pV}{Z(p,T)RT} \tag{5.3}$$

The number of released gas molecules was calculated from the measured pressure and temperature values and plotted for both the ytterbium and lanthanum samples (lowermost plots in figure 5.8). Because much of the gas was released in the beginning of the milling, the milling time is plotted logarithmically in these two figures. The gray curve plotted together with the raw data in the uppermost four figures is the pressure that is calculated from the measured temperature using the compressibility of hydrogen. This was done in order to probe the reliability of the molar calculation: The calculated and measured pressure curves fit reasonably well within the stationary range, which makes the molar calculation reliable. A common observation is that the calculated pressure is a bit too high just after the milling ends, or said another way: The measured temperature is too high. Right after milling, the temperature increases and the pressure decreases, which is unphysical in a stationary closed system. We could think of the following possible explanations:

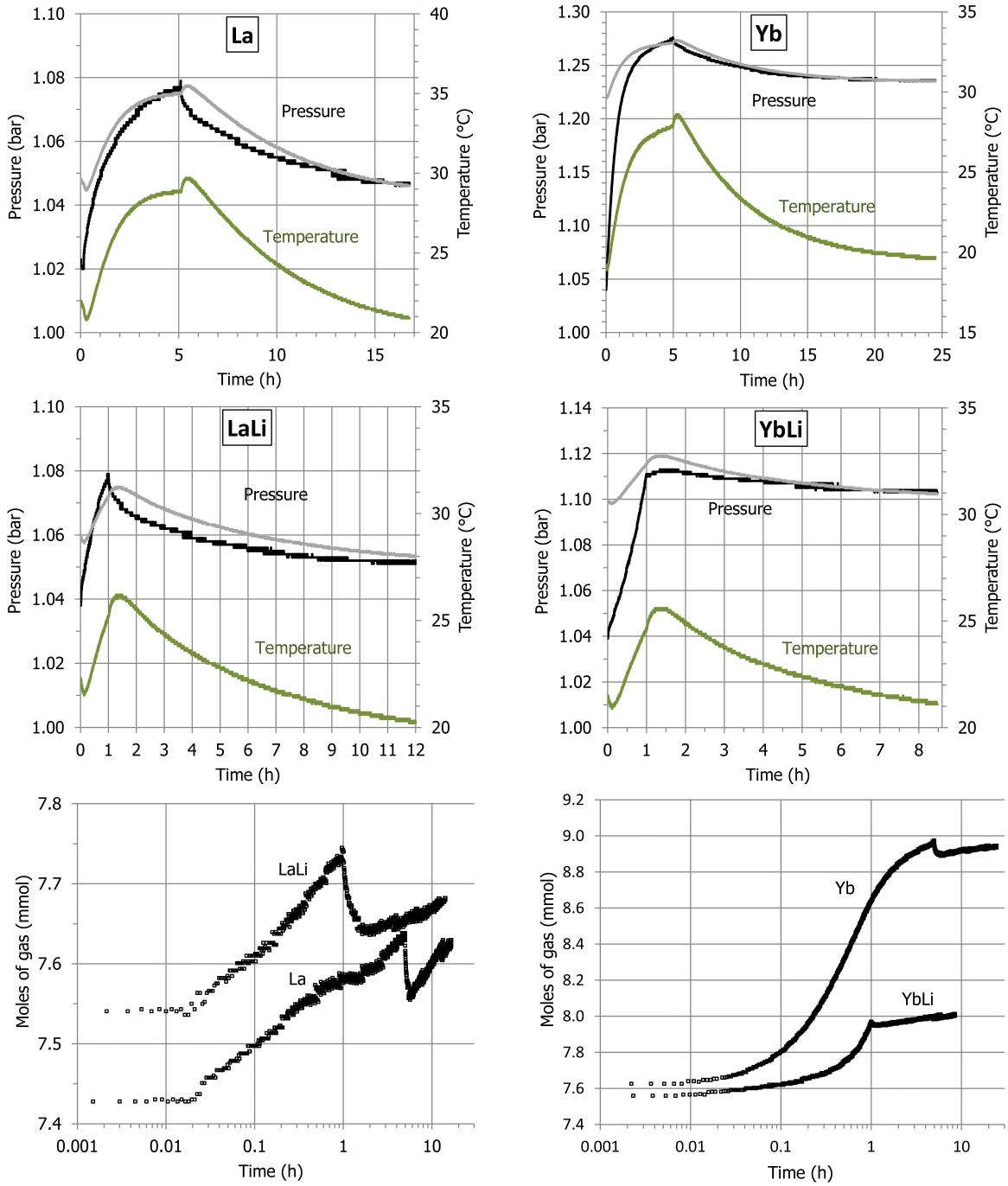


Figure 5.8: Pressure and temperature measured *in-situ* during ball milling of *La* (upper left), *LaLi* (middle left), *Yb* (upper right) and *YbLi* (middle right). The gray curves are the pressure values calculated from the temperature and the compressibility of hydrogen, using the last measurement points as reference. The two figures at the bottom show the calculated amount of gas present during milling.

1. There are temperature differences in the apparatus during milling which is caused by the rapid movement of some of the parts which are air-cooled. There will consequently be a temperature gradient throughout the vial wall during milling. When the movements stop, the heat will distribute evenly and the temperature in the sensor area will increase more than the sample temperature, which will stay constant

or decrease.

2. The energetic movement of the balls creates currents in the gas which causes the pressure at the sensor point to increase during milling.

   In each case, these effects are of instrumental character, and they obviously dominate in the lanthanum samples where the pressure increase is much smaller. But luckily, the effect is only intermediate, and only the values at the beginning and the end of the measurement are needed for the molar calculations. The difference between the calculated and measured pressure curves at the very beginning of each measurement should correspond to the amount of gas developed during milling.

The exact results are presented in table 5.8, with weight percent calculations in case of pure hydrogen release and a combined hydrogen/diborane release.

Table 5.8: Calculated moles of gas lost during milling

| | $\Delta n$ (mmol) | $\delta$ | Mass loss, $H_2$ (wt%) | Mass loss, $\frac{1}{2}H_2 + \frac{1}{2}B_2H_6$ (wt%) |
|---|---|---|---|---|
| *La* | 0.196 | - | 0.0198 | (0.291) |
| *LaLi* | 0.152 | 0.9[1] | 0.0153 | (0.226) |
| *Yb* | 1.319 | - | (0.1332) | 1.958 |
| *YbLi* | 0.446 | 0.6 | (0.0451) | 0.662 |

The ytterbium samples both release more gas than the lanthanum samples. In principle, we do not know what kind of gas is released, but we will in the next sections see that the lanthanum based samples do not release diborane during heating, and it is therefore unlikely that this is produced during milling. No $LaH_{2+\delta}$ was observed in the a.m. *La* and *LaLi* samples, so the calculated value of $\delta$ is hypothetic. It's closeness to one is simply a mathematical consequence of a small $\Delta n$, and if no $LaH_{2+\delta}$ is produced, no gas should be released anyway, which is also the case.

The synthesis of *Yb*, which is supposed to not release any gas, indeed does. It is reasonable to conclude that ytterbium samples are more unstable than the lanthanum samples because of the possible reduction from a borohydride containing trivalent $Yb^{3+}$ to a borohydride containing divalent $Yb^{2+}$, (reaction 5.7) a process which releases equal amounts of hydrogen and diborane gas molecules. This is the only reaction that can release gas in the milling of *Yb*, since no $YbH_{2+\delta}$ is produced. $LiYb(BH_4)_{4-x}Cl_x$ is therefore considered to be an unstable intermediate in the metathesis reaction.

The gas released during synthesis of *YbLi* should partially originate from the $YbH_{2+\delta}$ formation, but the amount of $Yb(BH_4)_{2-x}Cl_x$ increased with from 0.5 mol% in *Yb* to 1.7 mol% in *YbLi*, which proves that diborane is produced here as well, according to equation 5.7. If we assume that the composition calculated in table 5.6 applies for the P6 millings and that all ytterbium enters into crystalline phases, we can proceed with the following argumentation:

Let's say we start out with $M$ moles $YbCl_3$ initially. From column 5 in table 5.6 it is now trivial that 75% of the ytterbium atoms has gone into $YbH_{2+\delta}$ and 25% into $Yb(BH_4)_{2-x}Cl_x$ (*via* the intermediate $LiYb(BH_4)_3Cl$). It would then be $0.75M$ moles $YbH_{2+\delta}$ in the composite, and according to equation 5.2 $0.75M\frac{1-\delta}{2}$ of $H_2$ should be released. $0.25M$ $Yb(BH_4)_{2-x}Cl_x$ is produced, and it follows from equation 5.7 that in

[1]Calculated from equation 5.2. No production of diborane assumed.

total $0.25M$ moles of hydrogen and diborane gas is produced from the ytterbium borohydride reduction reaction. In the two P6 milling steps of the $YbLi$ synthesis, a total of $1.32+0.45 = 1.77$ mmol gas was produced, and there were initially 4.609 mmol $YbCl_3$. In other words, 0.383 moles of gas was produced per mole of $YbCl_3$. If we assume that the P6 and P7 samples are equal, we then have the following equation for the total amount of gas produced out of $M$ moles of $YbCl_3$:

$$0.383M = 0.75M\frac{1-\delta}{2} + 0.25M \qquad \Rightarrow \qquad \delta = 0.645 \approx 0.6 \tag{5.4}$$

However, there are now made so many approximations that this result is very uncertain. The P6 milled samples not were the ones refined, and the samples do probably not have the exact same composition. The two reactions 5.7 and 5.2 could have other ytterbium-containing end products or some of the compounds could be amorphous. The calculated composition of the P7 milled samples is uncertain and we do not know the composition of the P6 milled samples. The lattice constant of $YbH_{2+\delta}$ changes very little with $\delta$, and an internal reference in the sample would be needed if this approached is being used to fix $\delta$. This has not been been done.

## 5.3 Decomposition pathways and thermodynamical properties

We have now gained insight in the mechanochemical reactions that produces the desired hydrogen storage composites, and how successful the discussed recipe is for the lanthanum and ytterbium systems.

The next task is to investigate how these composites behave as hydrogen storage materials. First in turn is to analyze the DSC-TGA-RGA and *in-situ* SR-PXD results in order to assess the decomposition pathways and hereby related chemical reactions of hydrogen release.

The discussed temperature uncertainty in the *in-situ* SR-PXD data constitutes a big challenge when changes in the diffraction patterns are going to be related to the calorimetric events measured with the DSC apparatus. When it is referred to the blower temperature, an accuracy of 1°C will be used, but the discussed uncertainty of $\Delta T_b = 6$°C should be added to each of these readings. The calorimetric readings have lower uncertainty, and will be referred to with an accuracy of 0.1°C. Although the heating rate was set the same in the calorimetric and in-situ SR-PXD measurements, a severe temperature offset may cause the heating conditions to be different. A further difficulty in relating the events which each other is the different atmosphere and pressure conditions during the DSC and SR-PXD measurements. Known processes like the orthorhombic to hexagonal phase transition of $LiBH_4$ can be used as guidelines to get an idea of the error in the temperature scale for each experiment. But as we have seen, this transition temperature can be lowered by chloride substitution in $LiBH_4$ or just the presence of catalysts, and will be a very uncertain reference. Identification of phases subsequently emerging and reasonable and qualitatively assignments of them to the calorimetric measurement is the most secure way to proceed with the analysis.

### 5.3.1 $6LiBH_4 + LaCl_3$ decomposition

#### Decomposition against vacuum

The results from the DSC-TGA-RGA experiment of the 2013 and 2012 *La* sample (solid and dotted lines respectively) are shown in figure 5.9 (The traces of the latter are from the 2012 measurement.)

The TGA and DSC traces of the two samples are almost identical, which is a strong indication that the 2013 synthesized sample indeed is the same as the 2012 sample, although $LiLa(BH_4)_3Cl$ was not crystalline in the newest sample. The initial discrepancy in the sample weight can be explained by bad stabilization and taring of the balance or errors in the correction file. The slight shifts in the DSC events are within the uncertainty of the calorimeter. In the following analyses, it will be referred to the temperature values of the old sample, since this was the one measured with SR-PXD.

The TGA trace exhibit two weight losses, one of 1.05 wt% from $150 - 200$°C and another double-step decomposition which releases 4.15 wt% from approximately 260°C. They are accompanied with a small and a bigger RGA signal of hydrogen detection, respectively. Around 300°C, there is a large hydrogen release as well. No diborane was detected. What we can say initially, is that the hydrogen content in $LiLa(BH_4)_3Cl$ is only 3.22 wt%, assuming that reaction 5.2 takes place completely, which is not enough to

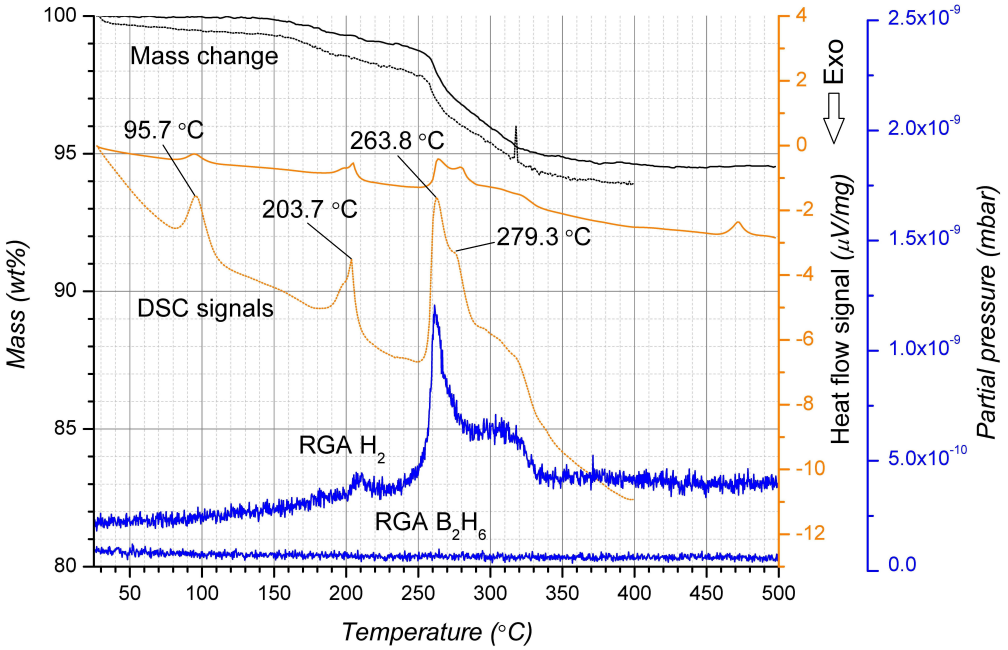


Figure 5.9: DSC and TGA curves of the 2012 (dotted) and 2013 (solid) *La* sample, as a function of temperature. The temperature ramps of the two measurements were identical. The RGA traces are from the 2013 sample.

explain the total hydrogen release of 5.20 wt%. This means that $LiBH_4$ has to decompose at least partially before 350°C.

The first endothermic event at 95.7°C in the 2012 DSC trace corresponds to the orthorhombic to hexagonal phase transition of $LiBH_4$. For pure $LiBH_4$ from the same batch measured at the same conditions, this transition happened at 115.5°C (figure 5.3). This stabilization of the hexagonal phase has been observed for $6LiBH_4 + CeCl_3$ previously[39], and is explained by chlorine substitution into $LiBH_4$[32]. This event is also seen on the right side in figure 5.10, where all the SR-PXD images up to isothermal conditions in the range $2\theta = 10.8 - 13.4$ are displayed subsequently, starting from the back with the first image: The first black line ($T_b = 115$°C) shows where the fifth peak from $ortho - LiBH_4$ (marked with the blue spike) vanishes and the third peak from $hex - LiBH_4$ arises (marked with a blue spike and a $h$). Although the atmosphere in the DSC and SR-PXD measurements were different, is it believed that the phase transition temperature measured with the DSC (95.7°C) is more or less the same in the SR-PXD case, and consequently, the real sample temperature at $T_b = 115$°C should be somewhat lower, probably between 96 and 100°C.

At the first black line in figure 5.10, also a rise in the $LiLa(BH_4)_3Cl$ phase and an increased descend in the $LaCl_3$ phase is observed. This is very likely due to a renewed activation of reaction 5.1, which was not completed after ball-milling. In other words, a temperature of around 100 °C causes a heat transfer equivalent to the activation energy needed for the reaction to proceed, and the sample composition should now agree even more with the right side of equation 5.1.

Next, there is a doublet in the DSC trace around 200°C (exact 198.9 / 203.7°C). $LiCe(BH_4)_3Cl$ was reported[39] to decompose exactly around 200°C by isothermal desorption. It is therefore plausible that one of the two DSC events around 200°C correspond to a decomposition of $LiLa(BH_4)_3Cl$. The other event might be a melting. A decomposi-

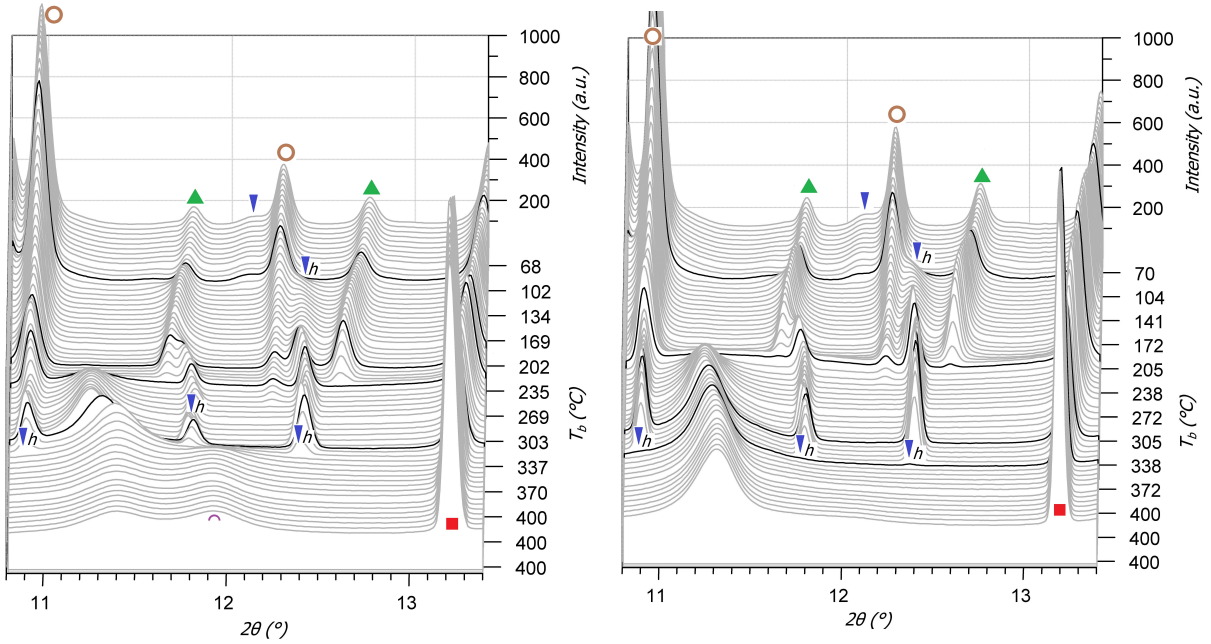


Figure 5.10: Decomposition of *La* under vacuum (left) and back pressure (right).
Blue spikes: $LiBH_4$. Hexagonal phase marked *h*.
Green triangles: $LiLa(BH_4)_3Cl$.
Brown circles: $LaCl_3$.
Red squares: LiCl.
Purple arcs: $LaH_{2+\delta}$. Orthogonal phase marked *o*.

tion or melting of this phase (marked with green triangles) is observed around the second black line in figure 5.10 ($T_b = 242°C$). The intensity of the LiCl peaks is almost unchanged. Simultaneously, the intensities of the $LiBH_4$ reflections increase, and they move steadily towards higher angles in this region (seen by zooming in on the relevant peak, not shown), which means that the unit cell contracts, caused by chloride substitution. Chlorine atoms have higher scattering strength and smaller ionic radius than $[BH_4]^-$ groups. These chlorine atoms must then come from $LiLa(BH_4)_3Cl$, indicating that this compound decomposes, at least partially. When using the molar fractions in table 5.2, the hydrogen content in $LiLa(BH_4)_3Cl$ constitutes 1.27% of the total sample weight, which allows for the 1.05 wt% release of hydrogen in this first decomposition step. And there is probably even more $LiLa(BH_4)_3Cl$ available, as discussed above.

The third black line marks the start for an unknown, broad peak around $2\theta = 11.25°$, which is believed to be a decomposition product of $LiLa(BH_4)_3Cl$, probably a species containing hydrogen and lanthanum or boron. Much effort has been done in order to identify or solve this intermediate, without success. At around $T_b = 353°C$ (close to the fourth black line), this broad peak suddenly shifts to $2\theta = 11.38°$, which also is the case with the other peaks of this phase (not shown). This is believed to be a further decomposition of this intermediate, and is attributed to the strongest DSC peak at 263.8 °C and the observed hydrogen release which occur simultaneously. The weak peak at $2\theta = 11.90°$ is assumed to be the first peak of the $Fm\bar{3}m$ - phase of $LaH_{2+\delta}$. The other peaks belonging to this phase are identified as well (not shown). This is now considered to be the final decomposition product of $LiLa(BH_4)_3Cl$. Regardless of what the intermediate phase is, will the overall decomposition of $LiLa(BH_4)_3Cl$ be

$$LiLa(BH_4)_3Cl \rightarrow LiCl + LaH_2 + 3B + 5H_2 \tag{5.5}$$

which yields a hydrogen releases of 2.7 wt% from the sample ($\delta$ set to zero for convenience). This explains the weight loss up to around 270°C.

The melting of hexagonal $LiBH_4$ is attributed to the DSC peak at 279.3 °C, which is closest to the melting point of pure $LiBH_4$ (283.8°C, see figure 5.3). The three peaks associated with it in figure 5.10 start to descend at $T_b = 363$°C (marked with the fourth black line), which indicates a melting or a decomposition. The abrupt (at least in the vacuum decomposition) vanishing of the peaks suggest that indeed a melting takes place.

The right shoulder on the DSC trace at around 300 °C coincides nicely with the mentioned RGA signal of hydrogen detection, and is attributed to a decomposition of $LiBH_4$. In this way only can the total hydrogen loss up to this temperature be explained. The decomposition temperature is far lower than that of pure lithium $LiBH_4$ (450-500 °C), which can only be explained by an alternative decomposition pathway. Since $LaH_{2+\delta}$ was observed to form at 264°C, this is supposed to be the destabilizing agent.

It is clear from the above analysis that there is a huge difference between the SR-PXD blower temperatures $T_b$ and the DSC-measured temperatures $T_s$. By using the phase transition and melting temperatures of $LiBH_4$ as reference points, one arrives at the relation

$$T_s = 0.74T_b + 11 \tag{5.6}$$

According to this correction, an indicated blower temperature $T_b = 400$°C reduces to a sample temperature of $T_s = 291$°C, and consequently, the SR-PXD series does probably not cover the decomposition of $LiBH_4 + LaH_{2+\delta}$, which is also seen by the preserved $LaH_{2+\delta}$ reflections at isothermal conditions.

A steady decrease in the $2\theta$- values for LiCl throughout the temperature ramp period is consistent with a linear thermal expansion in this temperature region[59].

### Back pressure decomposition

Almost the same behavior was seen when the *La* sample was decomposed under back pressure. All the images in the same $2\theta$ range ($10.8° - 13.4°$) are displayed on the right side in figure 5.10. The values of $T_b$ for the hexagonal-orthorhombic phase transition of $LiBH_4$ and other events were not found to deviate more from the corresponding events in the vacuum series than the uncertainty of the reading. Moreover, we have seen that systematic errors are present. A general effect from the back pressure is therefore not possible to deduce from these data.

But there is one important difference: The broad peak at $2\theta = 11.90$ belonging to $LaH_{2+\delta}$ does not appear in the back pressure series, and this compound is probably not formed. Moreover, the reflection at $2\theta = 11.38°$ belonging to the unknown intermediate does neither shift significantly nor decrease in intensity as it does in the vacuum series. Probably, the decomposition temperature of this compound is highly pressure dependent (small $\Delta H$), and would have happened at higher temperatures, according to the van't Hoff equation (equation 3.17). In that sense is the previous reported inhibiting effects of back pressure in agreement with this experiment.

### 5.3.2 $6LiBH_4 + YbCl_3$ decomposition

#### Decomposition against vacuum

The results from the DSC-TGA-RGA measurements of *Yb* milled and measured summer 2012 at 310 rpm (dotted lines) and *Yb* milled spring 2013 at 400 rpm (solid lines) are presented in figure 5.11.

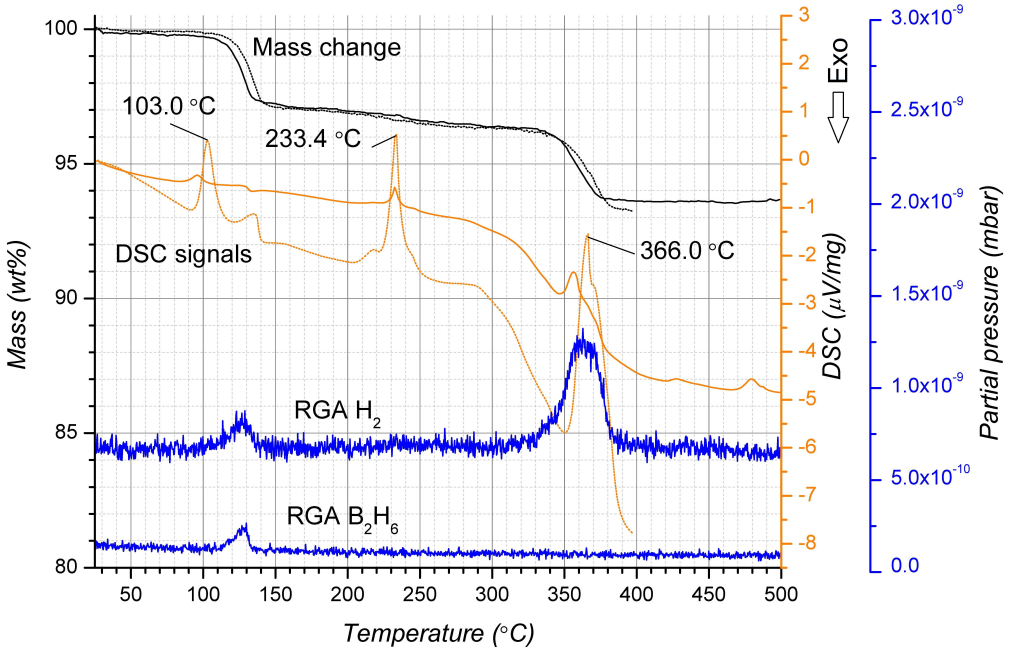


Figure 5.11: DSC and TGA curves of the old (dotted) and new (solid) *Yb* sample, as a function of temperature. The temperature ramps of the two measurements were identical. The RGA traces are from the 2013 sample.

The DSC and TGA curves of the two different samples are similar, except for a slight shift towards lower temperatures for some of the events in the new sample. This means that the different milling speeds had minor consequences for the metathesis reaction. The RGA traces are from the 2013 *Yb* sample.

The TGA trace shows two distinct decomposition events, one at around 125°C of 2.53 wt% and one at around 355°C of 2.68 wt%. The first event is accompanied with a RGA detection of hydrogen and diborane, whereas the second is a pure hydrogen release.

The SR-PXD-studied decomposition of *Yb* up to isothermal conditions is shown for all low-angle peaks ($2\theta = 6 - 17°$) in figure 5.12. The calorimetric events are discussed together with the events observed in the *in-situ* SR-PXD data. The assignments in the following analysis will again refer to the temperatures of the old sample's DSC curve.

The orthorhombic-hexagonal phase transition of $LiBH_4$ was observed in the SR-PXD data at $T_b = 113°C$, which corresponds to the endothermic peak in the DSC trace at 110.6°C. This is slightly lower than the temperature for pure $LiBH_4$ (115°C), indicating a much lesser degree of chlorine substitution (if any) than in the *La* sample.

It is reminded (see section 3.2.4) that the $Yb^{3+}$-containing borohydride $Yb(BH_4)_3$ was reported to decompose into the $Yb^{2+}$-containing $Yb(BH_4)_{2-x}Cl_x$ borohydride, diborane and hydrogen. $LiYb(BH_4)_3Cl$, which is the major borohydride in the present sample, also contains trivalent ytterbium. The second endothermic event at 135.0°C which is

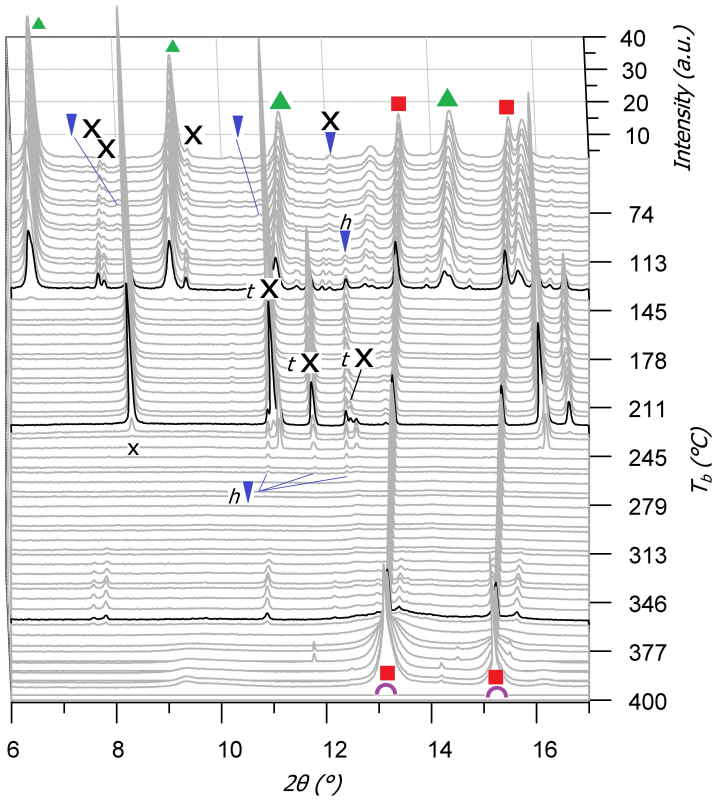


Figure 5.12: Selected *in-situ* SR-PXD images of $Yb$ decomposed under vacuum.
Blue spikes: $LiBH_4$. Hexagonal phase marked $h$.
Green triangles: $LiYb(BH_4)_{4-x}Cl_x$.
Black crosses: $Yb(BH_4)_{2-x}Cl_x$. Tetragonal phase marked $t$.
Red squares: LiCl.
Purple arcs: $YbH_{2+\delta}$.

accompanied by a loss of both diborane and hydrogen gas is thus a result of the reduction of trivalent ytterbium into divalent ytterbium (reaction 5.7).

$$\mathrm{LiYb(BH_4)_3Cl} \rightarrow (1-x)\mathrm{LiCl} + x\mathrm{LiBH_4} + (\mathrm{tet})\mathrm{Yb(BH_4)_{2-x}Cl_x} + \frac{1}{2}\mathrm{B_2H_6} + \frac{1}{2}\mathrm{H_2} \quad (5.7)$$

The diborane and hydrogen gas released here constitutes 2.5 wt% of the total $Yb$ sample, taking into account that only 0.7 moles $LiYb(BH_4)_3Cl$ were formed per mol $YbCl_3$ (found from table 5.3). This is in very good agreement with the observed weight loss. Divalent ytterbium has higher electronegativity than trivalent ytterbium and the borohydride group will thus be destabilized, as previously discussed. The solid byproducts written here ($LiBH_4$ and LiCl) are proposed as a possible decomposition pathway. This reaction is also observed in the SR-PXD data: At the first black line ($T_b = 135°C$), the peaks from $LiYb(BH_4)_3Cl$ (marked with green triangles) vanishes. Simultaneously, $Yb(BH_4)_{2-x}Cl_x$ (marked with black crosses) transforms from the orthorhombic to the tetragonal phase (listed in table 3.3).

The strong $tet-Yb(BH_4)_{2-x}Cl_x$ peaks gradually shift towards higher $2\theta$ values throughout the region $T_b = 135 - 232°C$ as a result of increased chloride substitution (higher $x$) and/or hydrogen/diborane release. This is consistent with the almost continuous weight loss of about 1.0 wt% between the two decomposition steps in the TGA trace.

At the second black line in figure 5.12, the peaks from $tet-Yb(BH_4)_{2-x}Cl_x$ borohydride vanishes. In the DSC trace, there is a strong endothermic peak at 232.8°C which according to Olsen[42] could be connected to a peritectic decomposition. This results in a sudden decrease in the Bragg peak intensity of $tet - Yb(BH_4)_{2-x}Cl_x$ in the SR-PXD data and simultaneous formation of a molten/amorphous product.

The $hex-LiBH_4$ peaks were not seen to shift significantly, and their intensities are low, both indicating almost no chlorine substitution, verifying the assumption above. They are observed to fade away around $T_b = 262$°C. The corresponding calorimetric event likely to be the melting of $LiBH_4$ is the rise of the dotted (2012) DSC trace around 280°C in figure 5.11.

Lastly, at the third black line in figure 5.12, $tet - Yb(BH_4)_{2-x}Cl_x$ finally decomposes into $YbH_{2+\delta}$ (marked with purple arcs) and LiCl (seen by an increase in the reflections from the latter). This is attributed to the second weight loss and the endothermic event at 366°C in figure 5.11, in accordance to the conclusion drawn by Olsen. The overall decomposition pathway of the ytterbium borohydride will then be

$$\begin{aligned} LiYb(BH_4)_3Cl \rightarrow &\quad Yb(BH_4)_2 + LiCl + \tfrac{1}{2}B_2H_6 + \tfrac{1}{2}H_2 && (5.8)\\ \rightarrow &\quad YbH_2 + 2B + LiCl + \tfrac{1}{2}B_2H_6 + \tfrac{7}{2}H_2 && (5.9) \end{aligned}$$

Chlorine substitution is omitted and $\delta$ is set to zero for simplicity. This does not affect the overall gas release significantly. The amount of diborane and hydrogen released constitutes 3.6 wt% of the total sample if the composition given in table 5.3 is correct. Even with the composition of reaction 5.2 (in that case a 5.1 wt% gas release), the observed weight loss is not explained, and also in this case, we can conclude that $LiBH_4$ decomposes right after 366°C through an alternative pathway involving $YbH_{2+\delta}$. This reaction probably corresponds to the right shoulder of the endothermic peak at 366°C. An unknown phase with weak reflections appearing right before this event in the SR-PXD data may take part in the reaction, but is not investigated further. The reflections from ytterbium hydride appear just before isothermal conditions is reached, and the decomposition products of $LiBH_4 + YbH_{2+\delta}$ are not not revealed here either.

**Decomposition against back pressure**

The SR-PXD data of the decomposition of $Yb$ under back pressure are very equal to the vacuum series, and are thus not shown. Actually, $YbH_{2+\delta}$ was observed here as well. One small difference was that the $ortho-Yb(BH_4)_{2-x}Cl_x$ phase increased for a while after the $LiBH_4$ phase transition before it faded away again at $T_b = 147$°C, which is significantly later than in the vacuum series. The fading of $hex - LiBH_4$ were observed at $T_b = 258$, which is in the same temperature region as in the vacuum series. This time, a slight increase of the LiCl peaks was observed in addition at this temperature. The only clear consequence of back pressure decomposition is a slight inhibiting effect of a few °C for the orthorhombic-tetragonal transition of $Yb(BH_4)_{2-x}Cl_x$.

### 5.3.3 $6LiBH_4 + LaCl_3 + 3LiH$ decomposition

Figure 5.13 shows the DSC-TGA-RGA measurements of the 2012 $LaLi$ sample (solid lines), which proved to stay undamaged during the transportation. Also the DSC and TGA traces of the $La$ sample are shown with dotted lines as comparison. The previous

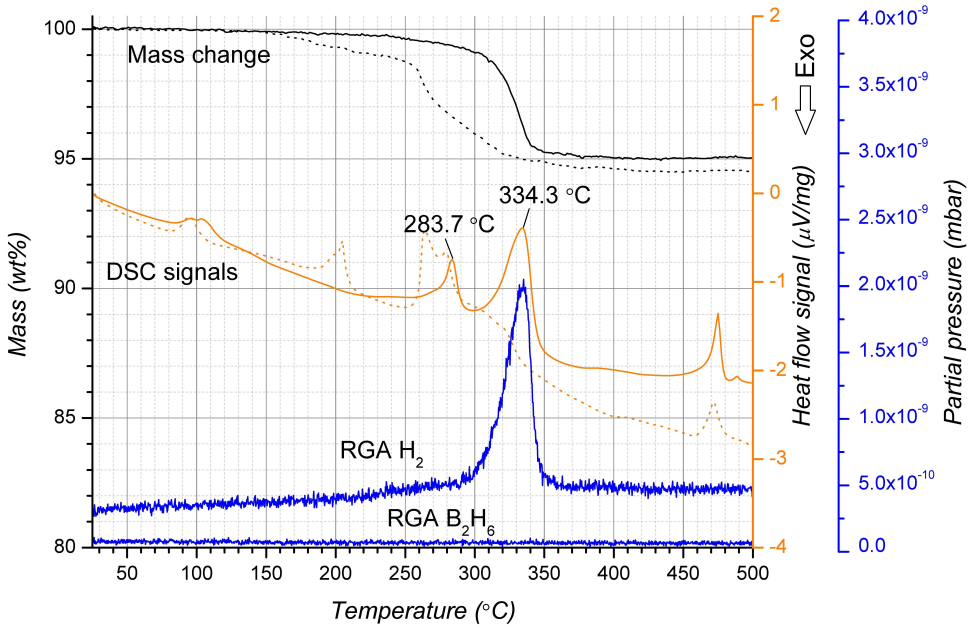


Figure 5.13: DSC-TGA-RGA curves of the *LaLi* sample, as a function of temperature. The DSC and TGA curves of *La* are shown dotted for comparison.

refinements have shown that the compounds in the *as-milled* samples are the same, although with different molar ratios. Completely different decomposition processes of *La* and *LaLi* are therefore not expected.

At a first glance, however, the process is indeed very different from the *La* sample, and very similar to the previously studied $6LiBH_4$-$CeCl_3$-LiH sample (see section 3.2.4). The TGA curve shows an abrupt weight loss of 4.8 wt% at $300-340$°C, which is accompanied by a single endothermic event at 335.7°C and a strong RGA signal of hydrogen gas. This event corresponds most likely to a single-step decomposition reaction, presumably of $LiBH_4$, whereas the *La* sample was seen to decompose in a multi-step reaction due to the presence of $LiLa(BH_4)_3Cl$. The DSC trace up to the decomposition also indicates two different pathways. The first endothermic peak is lowered to 95.2°C and indicates again a stabilized hexagonal $LiBH_4$ phase and hereby lowered phase transition temperature. The melting occurs also slightly higher (285.5°C compared to 283.8°C for pure $LiBH_4$), which also supports this. The absence of the endothermic peaks related to $LiLa(BH_4)_3Cl$ around 200°C observed in figure 5.9 is consistent with the deductions from the phase fraction analysis of that the *LaLi* sample contains much less $LiLa(BH_4)_3Cl$ than the *La* sample. If $LiBH_4$ is the main decomposing compound, the shift of the decomposition temperature from 450°C (inflection point) to 330°C is a major improvement, although it still happens over the melting point. $LaH_{2+\delta}$ could not be identified in the *as-milled* sample, and the question now arises, what destabilizes $LiBH_4$, if $LaH_{2+\delta}$ happens to be absent throughout the whole process.

In figure 5.14, all images up to isothermal conditions from the *LaLiVac* (left) and the *LaLiBack* (right) series are displayed for $2\theta = 8.4 - 14.2°$. The terminal calibrated temperature was $T_{calib} = 345$ and 370°C respectively. The images are plotted subsequently along the $T_{calib}$ axis, with values calculated according to equation 4.14 and 4.15 for *LaLiVac* and *LaLiBack* respectively. It is reminded that the terminal blower temperature was set to $T_b = 440$°C for both series, and that the reading uncertainty is estimated

to be ±7°C, i.e. $\Delta T_{calib} = 14$°C. The slightly different calibrations give rise to the different end temperatures of 345 (vacuum) and 370°C (back pressure). All identified phases are represented in the displayed range and are marked as before (see figure caption).

As mentioned in the experimental section, was the *LaLi* sample remeasured in May 2013, because the first measurements of this series were partially ruined by an extreme temperature offset. The P6-prepared sample brought to the last session had a slightly different initial composition, with the absence of crystalline $LiLa(BH_4)_3Cl$ as the most important difference. The initial state of this sample has not been refined, but can be seen in the backmost images in figure 5.14. In the measurements from November 2012 (not presented), $LiLa(BH_4)_3Cl$ was seen to rise in intensity at around $T_{calib} = 115$°C, before it vanished at the same time as the reflections of $hex-LiBH_4$ were seen strengthen and shift towards higher angles, i.e. the same behavior as what was seen in the *La* sample. For all other phases, the development under heating was identical in both the *LaLi* samples. It is thus concluded that reaction 5.1 is activated also under heating of the *LaLi* sample.

Finally, it should be stressed that the wavelength used in these measurements were $\lambda = 0.68291$ Å instead of the previously used $\lambda = 0.694118$ Å. From Bragg's law, we find that

$$\frac{d\lambda}{\lambda} = \frac{d\theta}{tan\theta} \tag{5.10}$$

so with a relative wavelength difference of $\frac{d\lambda}{\lambda} = 0.0163$, we get a scattering angle shift of $d\theta = 0.0007°$ at $2\theta = 5°$ and $d\theta = 0.0036°$ at $2\theta = 25°$, meaning that reflections to a great extent can be compared with the other measurements.

The overall process looks similar to the *La* case, but the following differences are observed, in addition to the absence of $LiLa(BH_4)_3Cl$: Firstly, the unknown phase represented by the broad peak around $2\theta = 11.25°$ in the *La* sample is not present. Secondly, the background is much higher from $2\theta = 11 - 14°$, so there can be compounds taking part in or catalyzing the reactions which cannot be identified with SR-PXD. Thirdly, $LaH_{2+\delta}$ decomposes around $T_{calib} = 344$°C (right before the isotherm is reached), reacts with boron and forms $LaB_6$ in the vacuum decomposition. This does not happen in the back pressure decomposition, on the contrary, the $LaH_{2+\delta}$ peaks increases in intensity.

The phase transition of $LiBH_4$ is observed to begin at $T_{calib} = 104$°C and $T_{calib} = 114$°C for the vacuum and back pressure series respectively (marked with the first black line in both plots). The first reading fits reasonably well with the corresponding DSC event (95.2°C) within the estimated uncertainty. In the back pressure case, the transition occurs at a significantly higher calibrated temperature. If the temperature scales are correct, this again indicates that back pressure inhibits the reaction.

Chlorine substitution of $[BH_4]^-$ groups in $hex - LiBH_4$ is observed between the first black line and $T_{calib} \approx 200$°C. The second peak with hkl indices (002) shifts to higher angles significantly more than the first (100) reflection , and a little more than the third (101), meaning that the unit cell contracts mainly along the *c*- axis. The consequently minor release of gases is also detected in the TGA trace which gradually descends before the melting. This is in agreement with the reported lattice constants for chlorine substituted $LiBH_4$ (table 3.2), although the group[32] concludes that $hex - LiBH_4$ contracts isotropically. The non-isotropic electronic density and directional bondings of the $[BH_4]^-$ tetrahedra will eventually lead to an non-isotropic elongation if they are all oriented along the c-axis in the hexagonal modification.

The broad reflections from $LaH_{2+\delta}$ are emerging from around $T_{calib} = 220$°C in both

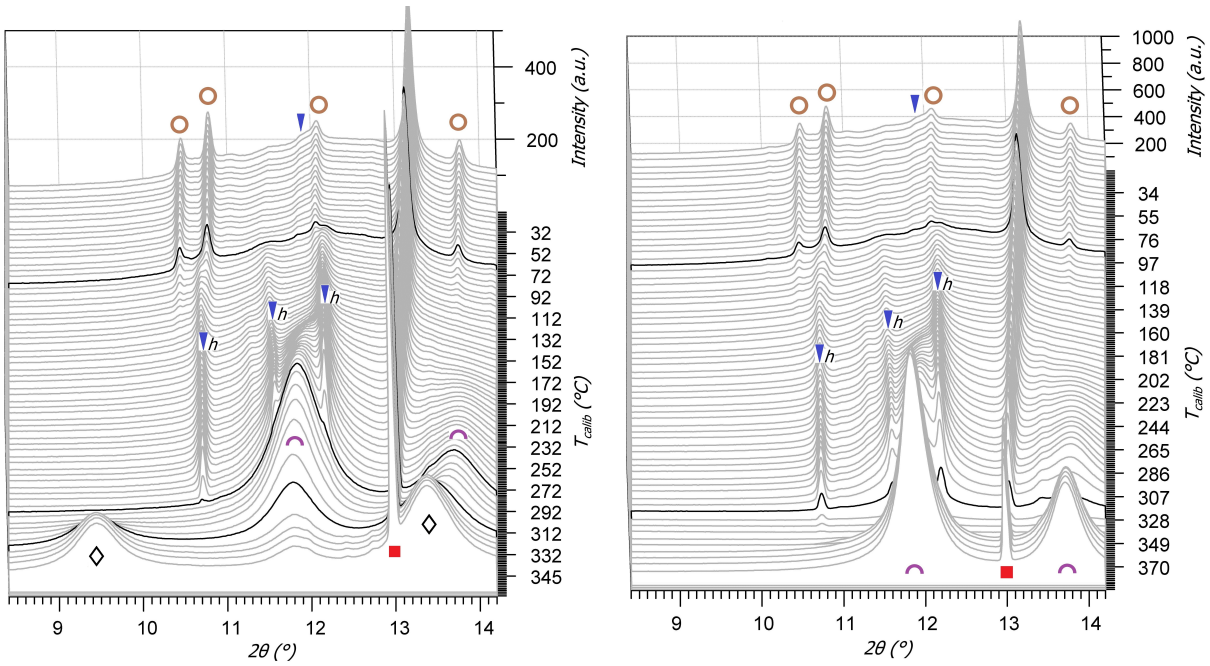


Figure 5.14: Decomposition of *LaLi* under vacuum (left) and back pressure (right).
Blue spikes: $LiBH_4$. Hexagonal phase marked *h*.
Green triangles: $LiLa(BH_4)_3Cl$.
Brown circles: $LaCl_3$.
Red squares: LiCl.
Purple arcs: $LaH_{2+\delta}$. Orthogonal phase marked *o*.
Black diamonds: $LaB_6$.

series, verifying that the heat activates the second metathesis reaction. The desired destabilizing additive is now present in the sample.

The melting of $LiBH_4$ is observed at $T_b = 311$ and 332°C for the vacuum and back pressure series, respectively (marked with the second black line). Even within the uncertainty are these values, especially the last, slightly too high, although a major chlorine substitution has taken place. To verify or reject this result, the following supplementary experiment was performed: A mixture of $LiBH_4$ and LiCl in molar ratio 2:1 was prepared only by using a hand mortar and pestle. A DSC-TGA measurement revealed an additional broad endothermic event at 289.1°C which is likely to correspond to a rapid anion substitution. The sharp endothermic peak belonging to the $LiBH_4$ melting was observed at 301.7°C, significantly higher than what has been reported previously[32]. This provides support to the melting temperature measured in the vacuum series. The calibration may therefore be wrong in the back pressure series. But again, it should be stressed that the atmospheres of the DSC-TGA and the two *in-situ* experiments are different, and the comparison basis is not optimal.

What is now most interesting, is that the alternative rare-earth based decomposition product $LaB_6$ is formed from around $T_{calib} = 344$°C in the vacuum series only (third black line). Simultaneously, $LaH_{2+\delta}$ decomposes. The onset of this reaction is a few degrees earlier, which is in good agreement with the temperature of decomposition measured with DSC (336°C). At the end of the series, narrow peaks belonging to the weakly scattering LiH were identified (not shown). It is quite clear that the desired destabilizing effect is achieved, namely that molten $LiBH_4$ reacts with $LaH_{2+\delta}$ and decomposes into $LaB_6$, $H_2$

and LiH at a drastically reduced temperature compared to pure $LiBH_4$.

However, in the back pressure series, this reaction is not initiated in the same temperature range. This is because the decomposition temperature is increased when the pressure is higher. The effect will be treated further in the discussion, when the results from the hydrogenation experiments have been presented as well.

### 5.3.4 $6LiBH_4 + YbCl_3 + 3LiH$ decomposition

In figure 5.15, the DSC-TGA-RGA results from the *YbLi* samples are shown. The dotted lines are the first measurements of the 2012 sample. The dashed line comes from the measurement of the 2012 sample after the transportation which can have caused it to oxidize. The solid line is the new 2013 sample. The first mass loss, which originates in the reduction of $LiYb(BH_4)_3Cl$ into $tet - Yb(BH_4)_{2-x}Cl_x$, is smaller for the old sample than for the new one, supporting the preceding lab-PXD results which indicated more $LiYb(BH_4)_3Cl$ in the new sample than in the old. No weight loss at around 100°C was observed after 7 months of storage and transportation, and slowly decomposition or oxidation of this phase can have taken place in the meantime. Also, the endothermic events are shifted towards higher temperatures, which might be the result of an inhibiting oxide layer on the crystallite surfaces.

Taking into account that *Yb* (figure 5.11) releases 2.53wt% of diborane and hydrogen at 100°C, the significant reduction of this event, at least for the dotted TGA trace (2012 sample), proves that the amount of trivalent ytterbium borohydride is drastically reduced. Coupled with the fact that the DSC trace strongly resembles that of pure $LiBH_4$, which was very weak for *Yb*, makes it clear that the SR-PXD refinements are reliable and the reaction products of equation 5.2 have been formed almost completely.

In the following, the two decomposition experiments (vacuum and back pressure) are treated in parallel and related to the DSC-TGA curves.

In figure 5.16, all the images of both decomposition series in the range $2\theta = 7 - 16°$ are displayed. It is generally observed that the indicated blower temperatures for the various events agree very well with the corresponding DSC-measured values, although no calibration was undertaken.

The first event, the $LiBH_4$ phase transition, is observed to happen in the *in-situ* data for $T_b = 106$°C (vacuum) and $T_b = 102$°C (back pressure) and is marked in both figures with the first black line. The temperatures coincide within the reading uncertainty. The event is found in the old DSC trace at 102.5°C, which is slightly lower than for *Yb* (110.6°C), but not as low as was the case in both the lanthanum samples (referring to the DSC-measured values). The peaks of $hex - LiBH_4$ are observed to rise from this point, although the first and second peaks are partly overlapping with other phases. The orthorhombic phase of $Yb(BH_4)_{2-x}Cl_x$ which was discussed in section 5.2.3 is seen to transform into the tetragonal phase at the second black lines, where $T_b = 148$°C (vacuum) and $T_b = 144$°C (back pressure). The first peak disappears gradually and is gone at around $T_b = 198$°C. The second peak of this tetragonal phase overlaps more or less exactly with the first $hex - LiBH_4$ peak ($2\theta = 10.8°$). They were distinguished from each other by analysis of the FWHM: For the 37$^{th}$ image ($T_b = 156$°C) in the *YbLiBack* series, this value was calculated with curve fitting to be 0.107° (standard deviation $\sigma = 0.005°$), whereas in the 65$^{th}$ ($T_b = 248$°C) the value is 0.074° ($\sigma = 0.004°$), clearly showing that these are peaks from two different phases. The width was qualitatively observed to decrease with the same pace as the rest of $Yb(BH_4)_{2-x}Cl_x$. This phase transition is found in the dotted

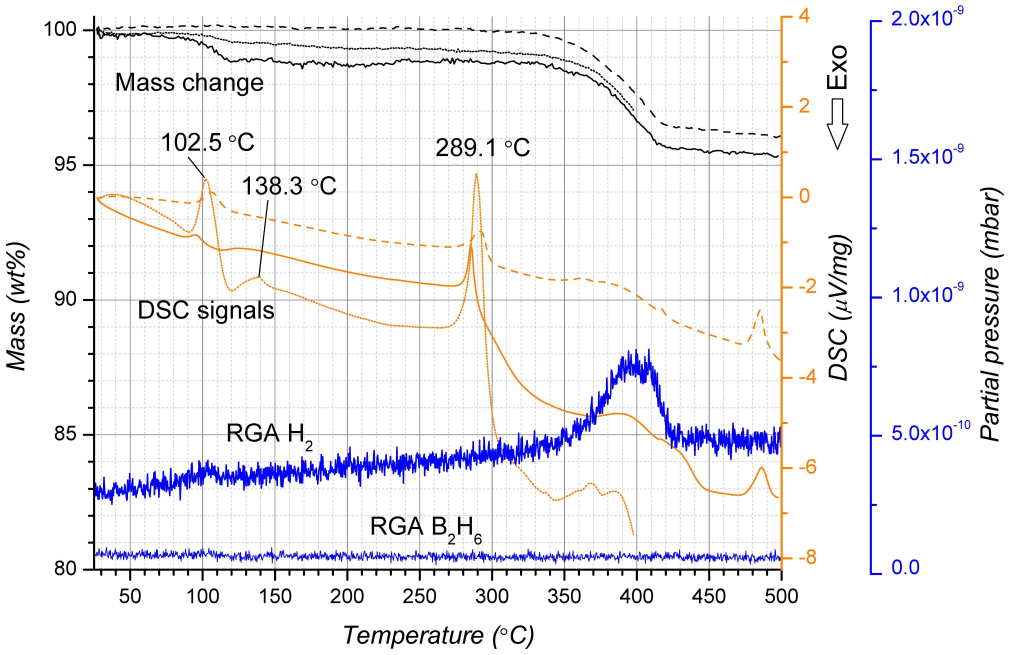


Figure 5.15: DSC and TGA curves of the 2012 measurement of the 2012 $YbLi$ sample (dotted), the renewed 2013 measurement of the 2012 sample (dashed) and the 2013 sample (solid) as a function of temperature. The temperature ramps of the three measurements were identical. The RGA traces are from the old sample, measured in 2013.

DSC curve as the weak endothermic event at 138.3°C.

The orthorhombic *Pnma* modification of $YbH_{2+\delta}$ starts to rise at the same time as $Yb(BH_4)_{2-x}Cl_x$ is gone, i.e. around $T_b = 198$°C in figure 5.16, which is a strong indication of the decomposition of the ytterbium borohydride. One of the peaks is seen at $2\theta = 12.53$ at the left side of the broad $YbH_{2+\delta}$ peak. For later images, $ortho - YbH_{2+\delta}$ increases in intensity in both series and the peaks are sharp.

Hexagonal $LiBH_4$ melts at the third black line in both figures. The blower indicates $T_b = 317$°C in the vacuum series, and $T_b = 308$ in the back pressure series. The sharp DSC peak at 289.1°C in figure 5.15 is considered to be the melting of lthium borohydride. It also resembles the shape of that for pure $LiBH_4$ (figure 5.3). This would mean that there is a slight error in the blower temperature at elevated temperatures. The degree of chlorine substitution does not necessarily have to be the same in the DSC and SR-PXD data either, which would yield different melting temperatures.

With the above argument mind, the second and biggest weight loss tracked by the TGA curve between 350 and 400°C is most probably not covered by the SR-PXD experiment, since the blower was set to heat no further than to 400°C. However, $ortho - YbH_{2+\delta}$ starts to disappear from the fourth black line in the vacuum decomposition only, and $LiCl/cub - YbH_{2+\delta}$ is observed to abruptly increase at this point. This is in the isothermal range, and the blower has reached 400°C already 13 images before. The decrease is relatively slow, which may indicate that the activation energy is barely achieved, and that the phase decomposes as the capillary adjusts to the ambivalent temperature. (All the peaks in the sample, LiCl included, are almost gone in a certain range around image 95. Such an unphysical process must be explained by en experimental failure, for example bad beam exposure due to eccentric rotation of the capillary.) Interestingly, $ortho - YbH_{2+\delta}$ does not vanish in the back pressure series. This is the same effect as was observed in

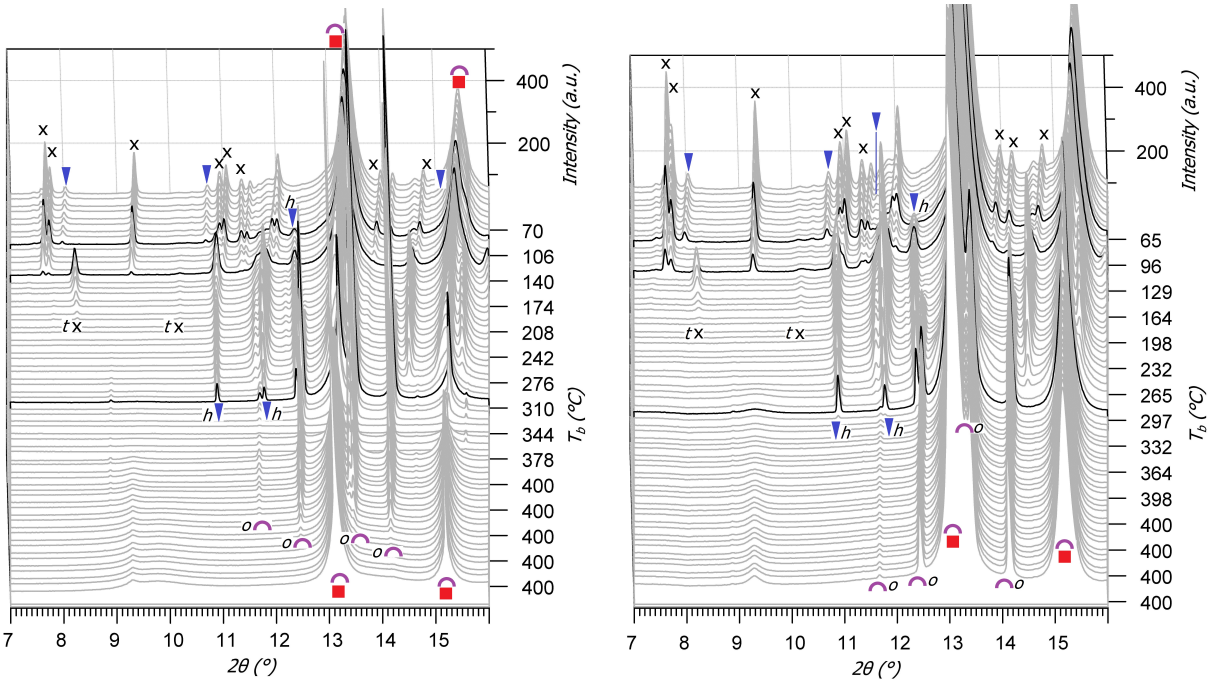


Figure 5.16: Decomposition of $YbLi$ under vacuum (left) and back pressure (right).
Blue spikes: $LiBH_4$. Hexagonal phase marked $h$.
Green triangles: $LiYb(BH_4)_{4-x}Cl_x$.
Black crosses: $Yb(BH_4)_{2-x}Cl_x$. Tetragonal phase marked $t$.
Red squares: LiCl.
Purple arcs: $YbH_{2+\delta}$. Orthogonal phase marked $o$.

the lanthanum case. To anticipate the upcoming events, it abruptly disappears once the $YbLiBack$ sample is exposed to 100 bar of hydrogen pressure, which indicates that the stability of this modification is highly dependent on pressure and temperature.

Finally, the second weight loss at $330 - 400°C$ is the decomposition of molten $LiBH_4$, which is the only compound that contains the amount of hydrogen released here (3.2%). Again, the presence of $YbH_{2+\delta}$ is lowering the total mass loss. The temperature of decomposition is higher than for $LaLi$, which is unexpected, since more $YbH_{2+\delta}$ was present in the $YbLi$ sample initially. This must be explained by less stable decomposition products. Also, no peaks which could be attributed to boron-ytterbium compounds were identified in either $YbLi$ decomposition series.

## 5.4 Hydrogenation properties

### 5.4.1 SR-PXD *in-situ* hydrogenation

**$La$ and $Yb$ samples**

We will only briefly examine the hydrogenation of the $La$ and $Yb$ samples, since no pcT experiments follow these series. The following discussion will constitute a comparison basis.

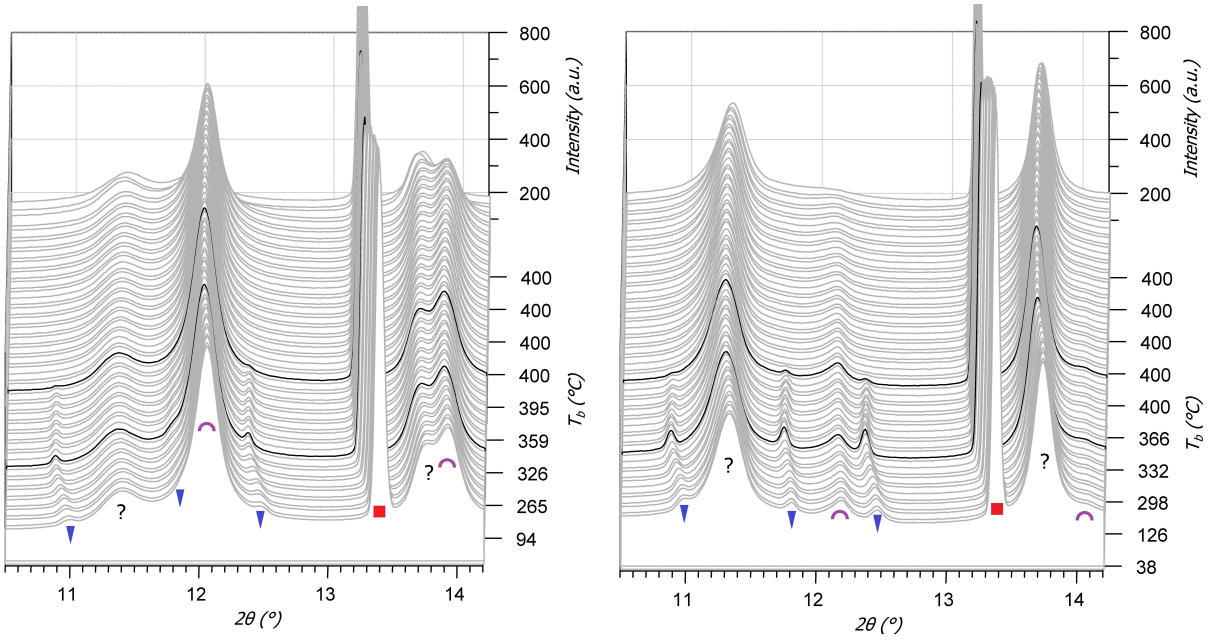


Figure 5.17: Hydrogenation and cooling of $LaVac$ (left) and $LaBack$ (right).
Blue spikes: $hex - LiBH_4$.
Red squares: LiCl.
Purple arcs: $LaH_{2+\delta}$.

In figure 5.17, the hydrogenation of the $LaVac$ (left) and the $LaBack$ (right) samples are shown. The three relatively weak peaks of tetragonal $LiBH_4$ appear at $T_b = 377°C$ (first black line) in figure 5.17 (the first and third are easiest to recognize), and at $T_b = 376°C$ in figure 5.17. If the *in-situ* decomposition of $LiBH_4$ is not completed, the peaks appearing here may come from undecomposed, molten material which solidifies when cooled under pressure. A sample composition calculation from a refinement of the hydrogenated sample would not help either, because only crystalline $LiBH_4$ is detected. Consequently, the accurate total amount of $LiBH_4$ before and after hydrogenation is not accessible from the present data, and it is not possible to say if an absorption has taken place by considering the powder diffraction measurements only.

Since the sample weight or desorbed gas is not analyzed in the SR-PXD measurements, we cannot be sure if $LiBH_4$ in fact has decomposed. However, recent pcT experiments performed on this sample by Olsen suggest that decomposition and rehydrogenation has taken place, at least partially: $La$ was desorbed in the pcT apparatus and was let dwelling at 400°C for 2 h. One part of the sample was investigated with DSC, showing an almost flat TGA curve. The other part was hydrogenated at 100 bar for 24 h, yet this time giving

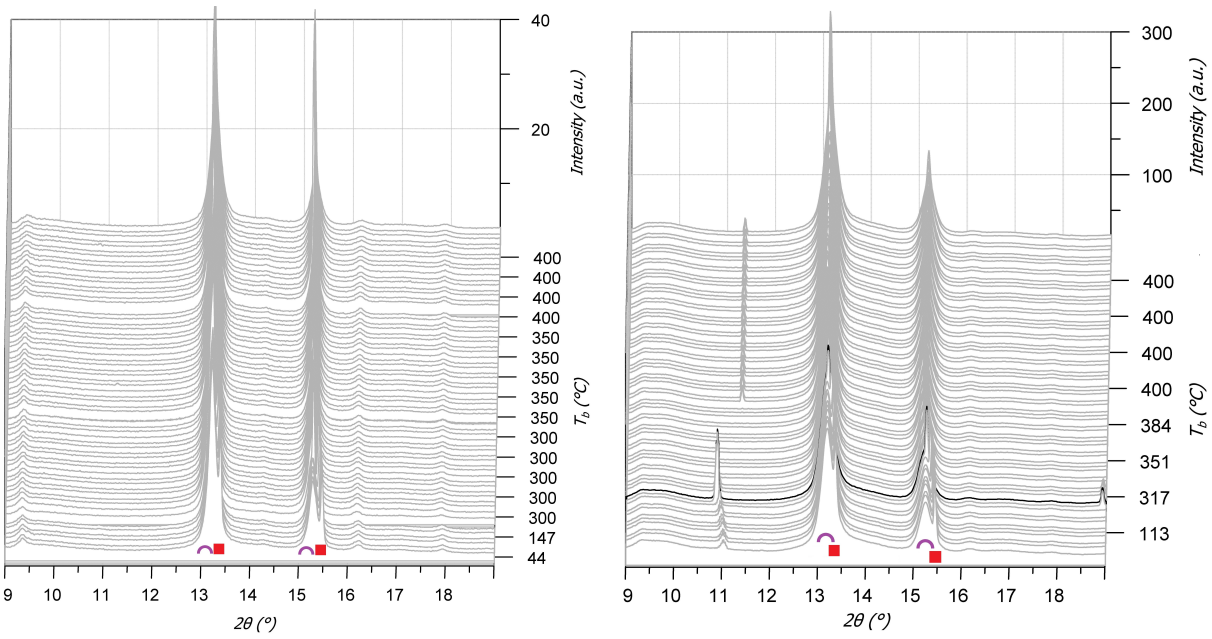


Figure 5.18: Hydrogenation and cooling of $YbVac$ (left) and $YbBack$ (right).
Red squares: LiCl.
Purple arcs: $YbH_{2+\delta}$.

a 2.2 wt% weight loss when examined with DSC-TGA, indicating a partial reversibility of the system.

The second black line in both figures marks the onset of the quick cooling from 300°C down to room temperature, easily identified by the starting of a steady contraction of the unit cell, for $LiBH_4$ as well as for LiCl. The phase transition back to orthorhombic $LiBH_4$ does apparently not occur.

The most interesting feature in these two series, however, is the different sets of broad peaks which are developed in both samples. The assumption from the $La$ decomposition analysis that $LaH_{2+\delta}$ is formed, is now reinforced: The peaks at $2\theta = 12.02°$ and $2\theta = 13.88°$ in figure 5.17 rise simultaneously in the beginning of the hydrogenation and belong thus very likely to the same phase. They have approximately the same FWHM, namely 0.229° and 0.238° respectively, supporting this. A FCC structure with $a = 5.70(1)$Å (at $T_b = 326$) explained all the peaks belonging to the phase. $LaH_{2+\delta}$ has a FCC structure with reported $a = 5.667$ Å[60], which is a very good candidate, taken into account the thermal expansion and the temperature and scattering angle uncertainties. The fact that this compound is formed or crystallizes when exposed to high hydrogen pressure makes it very convincing that this is $LaH_{2+\delta}$. It is also present in the $LaBack$ series (figure 5.17), although very weak. As mentioned, the explanation for this is that back pressure inhibits the decomposition events and consequently, $LaH_{2+\delta}$ is not formed to that great extent.

The unknown peaks represented by $2\theta = 11.39$ and $2\theta = 13.67$ are not believed to belong to the same phase, because of significantly different FWHM (0.487 and 0.195 respectively), although the relative intensity among them is similar in the two series.

In figure 5.18, the hydrogenation of the $YbVac$ (left) and $YbBack$ (right) samples are shown. Little is observed to happen in the $Yb$ hydrogenation, apart from a splitting of the $YbH_{2+\delta}$ and LiCl reflections and the upcoming of some small, sharp peaks in the back pressure series. None of these are Bragg peaks that originate from powder diffraction.

Closer examination of the unintegrated two-dimensional diffraction patterns revealed that the peak around $2\theta = 11.37°$ comes from the sapphire tube and is not masked properly, whereas the peak at $2\theta = 10.9°$ (rises at the black line) originates from two small circle sections, almost becoming dots. This might therefore belong to some sample material which has formed large single crystal grains.

The absence of $LiBH_4$ makes the temperature scale doubtful. Again, we neither here have supporting experiments confirming or rejecting the temperature scale.

### *LaLi* and *YbLi* samples

In figure 5.19, the SR-PXD series for the hydrogenation of the *LaLiVac* sample (left) and *LaLiBack* sample (right) are shown.

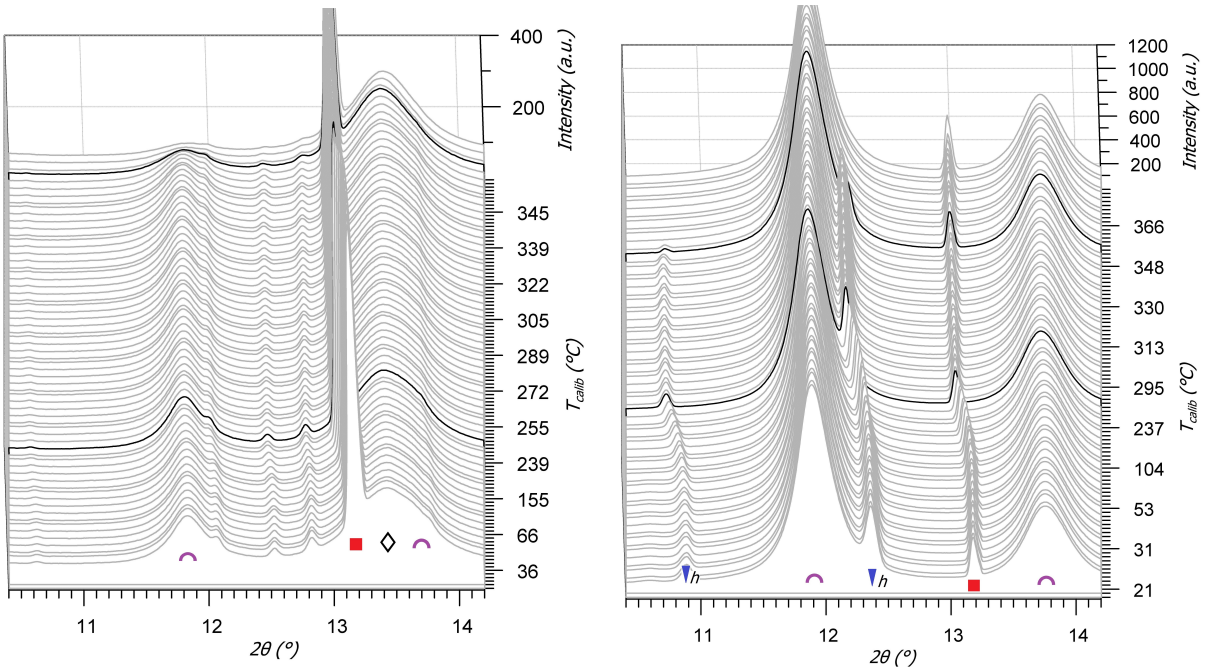


Figure 5.19: Hydrogenation and cooling of *LaLiVac* (left) and *LaLiBack* (right)
Blue spikes: $hex - LiBH_4$.
Red squares: LiCl.
Purple arcs: $LaH_{2+\delta}$.
Black diamonds: $LaB_6$.

In the hydrogenation of *LaLiBack*, $LaH_{2+\delta}$ is present throughout the whole process. In the hydrogenation of *LaLiVac*, it rises right after the 100 bar of hydrogen pressure has been applied (first black line), and stays unchanged afterwards. This is in essence similar to what was observed in the *La* case, although $LaH_{2+\delta}$ had not formed yet in that back pressure series.

The broad peak around $2\theta = 13.4°$ belongs to $LaB_6$, which stays unchanged throughout the hydrogenation. A reversal of the decomposition reaction is therefore not concerted and a possible hydrogen uptake must correspond to formation and possible growth (increased $\delta$) of $LaH_{2+\delta}$. The absence of $LiBH_4$ peaks proves that the vacuum decomposition has been completed.

The emerging of $hex - LiBH_4$ peaks in the *LaLiBack* hydrogenation at $T_{calib} = 348°C$ (first black line) is therefore considered to be solidification of molten, undecomposed

$LiBH_4$, as was previously assumed. It should be noted that the (002) reflection (around $2\theta = 11.8°$) does not appear. What was also observed from the unintegrated diffraction pattern, was that only certain short segments of the rings belonging to $LiBH_4$ appeared during hydrogenation. This is due to growth of single crystal grains with preferred orientation of the $c$ axis along the sapphire tube wall.

The onset of the quick cooling is seen to commence at the second black line in both figures. The diffraction peaks of all phases are seen to more or less shift to higher angles due to unit cell contraction.

The *YbLiVac* sample kept its diffraction pattern unchanged from the last decomposition image (figure 5.16) throughout the complete hydrogenation at 400 and 350°C. As can be seen in table 4.4, this sample was not measured during cooling. The only data of interest is the single image of the sample at room temperature, displayed in figure 5.20.

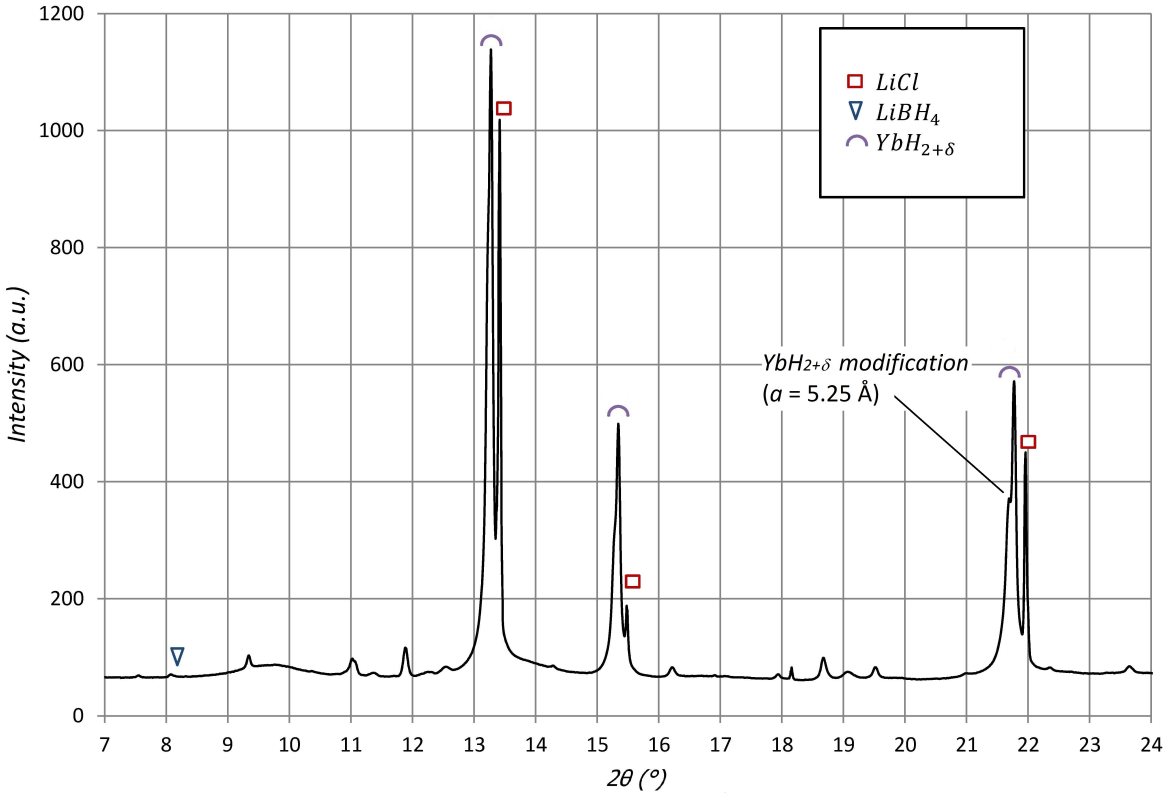


Figure 5.20: Image of *YbLiVac* at RT after hydrogenation. The three almost overlapping reflections are from the cubic unit cells LiCl (red squares), $YbH_{2+\delta}$ ($a = 5.192$ Å) and $YbH_{2+\delta}$ ($a = 5.25(3)$ Å) (purple arcs).

In addition to the splitting of LiCl (red squares) and $YbH_{2+\delta}$ (purple arcs), a third cubic phase is observed with almost overlapping reflections to the left of the two. This is best resolved at around $2\theta = 21.8$, where the discrepancy is bigger. The peaks are well explained by another FCC modification of $YbH_{2+\delta}$, which has a slightly bigger unit cell ($a = 5.25(3)$Å). The modification is reported[61] to form when $YbH_{2+\delta}$ is quenched from 450°C to room temperature in a short time.

There are traces of $ortho - LiBH_4$ (the first, strongest peak is marked with a blue spike) and possibly chlorine-stabilized $hex - LiBH_4$. During hydrogenation and cooling of *YbLiBack* (figure 5.21), a new phase developed from the black line ($T_b = 301$°C). This is none of the known $LiBH_4$ phases. In the very beginning of the *YbLiBack* hydrogenation,

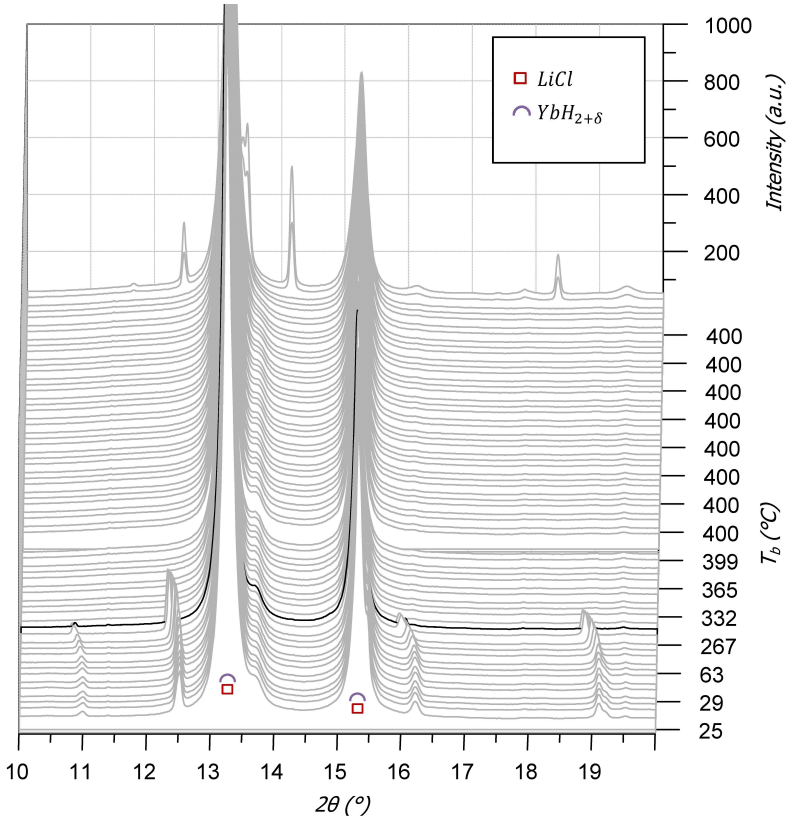


Figure 5.21: Hydrogenation and cooling of *YbLiBack*.
Red squares: LiCl.
Purple arcs: $YbH_{2+\delta}$.

orthorhombic $YbH_{2+\delta}$ is seen to abruptly disappear, closely following the pressure increase over the first few images.

None of the hydrogenation experiments actually hydrogenated and reversed any of the decomposed or partially decomposed samples. Conclusively, the dwelling time (30 min) was considered to be too short. Therefore, the *ex-situ* pcT hydrogenations were decided to last much longer (24 h), in order to get any interesting results (referring to section 4.2).

### 5.4.2 *Ex-situ* hydrogenation and redesorption

#### pcT desorption and absorption

As was explained in section 4.1.7, there are relatively large uncertainties related to calculations of desorbed or absorbed gas from the pcT raw data. The following results will therefore serve as indications of what will be verified or rejected by DSC-TGA, IR and PXD measurements of cycled samples. The *LaLi* and *YbLi* samples were treated according to table 4.5.

For the back pressure desorptions the system pressure $p_{sys}$, sample temperature $T_s$ and manifold temperature $T_m$ were used to calculate the number of moles of gas by utilizing the calibrated system volumes and hydrogen compressibility. To be able to compare the pcT with the SR-PXD experiments, stepwise isothermal absorption was not performed, because this requires long equilibration times. The analysis will therefore be constrained to the molar calculations of the total uptake and release of gas. Without a

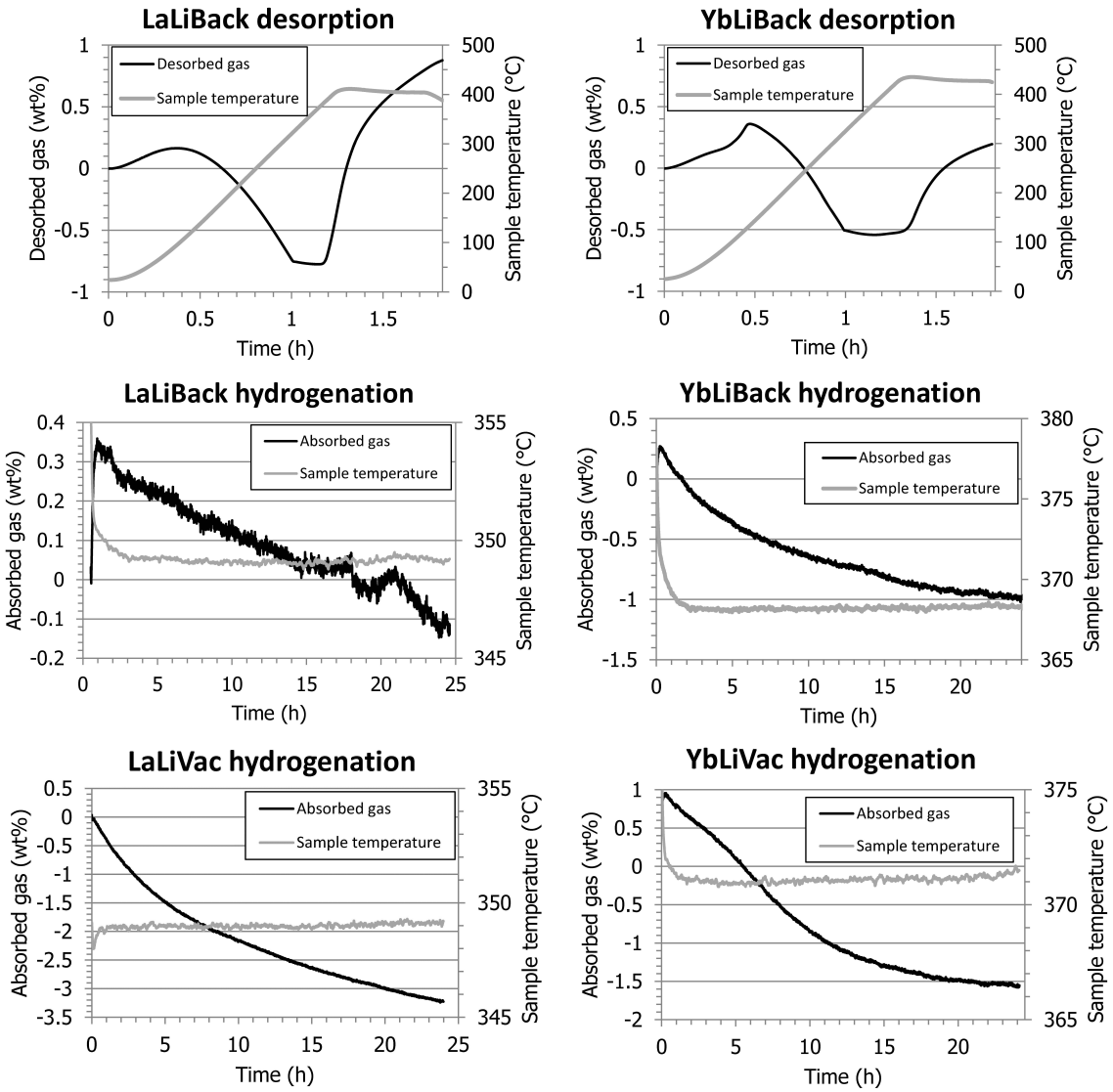


Figure 5.22: Desorption in the pcT apparatus of $LaLi$ (upper left) and $YbLi$ (upper right) under back pressure. Hydrogenation of $LaLiBack$ (middle left), $YbLiBack$ (middle right), $LaLiVac$ (lower left) and $YbLiVac$ (lower right).

closed system, molar calculations are not possible to perform, and the samples decomposed under dynamic vacuum are thus not analyzed in this way. The results from the pcT desorption and hydrogenation for $LaLiBack$ and $YbLiBack$ and the hydrogenation of $LaLiVac$ and $YbLiVac$ are graphically displayed in figure 5.22.

The calculated amount of desorbed gas during decomposition exhibits unexpected properties for both samples. The curves indicate a gas release in the beginning, followed by a gas uptake in the middle of the process. The initial "desorption" has not been observed in other experiments and is likely to be an effect from the non-stationary conditions. Later, the number of moles of hydrogen is not supposed to decrease, in fact, an uptake of hydrogen in the *as-milled* samples is only considered possible under extreme pressure and temperature conditions. The errors may originate in the following: There is a temperature gradient between the thermocouple and the sample during heating, the thermocouple being hotter than the sample. This would mean that a too high $T_s$ is inserted in the gas law, yielding a too low indicated amount of hydrogen gas in the system ($T_s \propto 1/n$). An

Table 5.9: Hydrogen gas absorption calculated from raw data (first row) and corrected for a possible leakage (second row), giving estimates for the maximum and minimum amount of absorbed gas, respectively.

| Sample | Absorbed hydrogen (wt%) | | | |
|---|---|---|---|---|
| | *LaLiVac* | *LaLiBack* | *YbLiVac* | *YbLiBack* |
| Raw data (max) | 3.25 | 0.47 | 2.51 | 1.25 |
| Leakage corrected (min) | 1.9 | 0 | 2.1 | 0.9 |

observed "absorption" is the result from this. Another interesting feature is the extra "bump" in the adsorption curve during *YbLi* decomposition shortly before half an hour, which is not observed for *LaLi*, although the temperature curves are very similar. This is likely to originate the first weight loss which only takes place for *YbLi*.

Then, the weight loss increases again at around the correct gas desorption temperatures; 335°C for *LaLi* and 400°C for *YbLi*. Although the exact onset of these desorptions are hard to read from the data due to the above discussed disturbing effects, the relative shift between them is consistent with previous observations (it is reminded that the SR-PXD data showed only a few °C shift between the vacuum and back pressure decomposition events, and *YbLi* decomposed about 50°C later than *LaLi*). The weight loss from the bottom of the desorption curves to the end of the experiments are 1.66 wt% and 0.74 wt% for *LaLi* and *YbLi* respectively, indicating that *LaLi* releases gas earlier and/or more than *YbLi*. The calculated weight loss is probably too low, since it will be the sum of the real desorption and the heat ramp "absorption" effect. Nevertheless, for both curves, it is easily seen that the dwelling was not long enough, since the derivatives of the adsorption curves are still very high at end of measurement.

Under hydrogenation, both back pressure absorption curves rise quickly in the first minutes of the experiments. This is believed to originate in the quick heating of the system by elevating the pre-heated oven, because the effect is stronger than in the start of the decomposition series (linear ramp). At stable conditions, the raw data show 2.7 times as high absorption for *YbLiBack* as for *LaLiBack* (exact values in table 5.9). However, the latter "absorbed" apparently more than it desorbed, which may be caused by a leak in the system[2]. According to the discussion in section 4.1.7 and appendix A, a leak will give a linear pressure drop at high pressure and for small pressure changes. For the *LaLiBack* hydrogenation, the constant slope over 24 h is clearly indicating a leak, and no absorption can be in fact be deduced. For the other three hydrogenation experiments, the pressure curves are not linear, but the slope is decreasing until it is almost constant. It is therefore possible to subtract the asymptote and deduce the minimum absorption. The total absorbed amounts of hydrogen gas with and without leakage correction are shown in table 5.9.

The vacuum decomposed samples are clearly superior with respect to absorption capacity, and there is apparently no absorbing host available in the *LaLiBack* sample. This is in agreement with the previous results that the back pressure decompositions did not proceed properly.

[2]The pressure drop during the $t = 85104$ s long *LaLi* absorption was $\Delta p_{sys} = 0.769$ bar. The volume of the total internal system was $V = 29.925$ mL. If this pressure drop only is due to a leak, the rate will be $\frac{\Delta p_{sys}}{Vt} = 0.302 \ \frac{\text{mbar}}{\text{Ls}}$, which is relatively high. (For comparison, the best case leak rate provided by Swagelok for the valve seats is $4^{-9} \ \frac{\text{mbar}}{\text{Ls}}$.)

What should be mentioned, is that the hydrogenated samples consisted of hard particles up to 1 mm thickness. Before these samples were investigated further, a hand mortar and pestle was used to crush them into powder. Presence of large particles will severely hamper reaction kinetics.

From this analysis, we can conclude that both *as-milled* samples do desorb gas under back pressure, with events more or less in accordance with the DSC-TGA-RGA experiments, but the full capacity is not released. On the other hand, it is likely that the vacuum desorptions were completed, according to previous results. Absorption of around 2 wt% in in the vacuum-decomposed samples is thereby explained. The *LaLiBack* and *YbLiBack* samples have clearly not decomposed completely and have thus poor absorption capacities.

### DSC-TGA of cycled samples

DSC-TGA measurements of the pcT decomposed and hydrogenated samples is one way to verify the weight change calculations in the previous section. For *LaLi*, only DSC-TGA of the hydrogenated *LaLiVac* and *LaLiBack* samples was performed, but for *YbLi* the pcT-decomposed sample was measured in addition. The two charts 5.23 and 5.24 present the measurements from the first and second decompositions of the *LaLi* and *YbLi*, respectively.

In figure 5.23, the DSC-TGA decompositions of the hydrogenated *LaLiVac* and *LaLiBack* samples are shown. Firstly, it is clearly seen that there is more gas released from *LaLiVac* (3.76 wt%) than from *LaLiBack* (1.89 wt%), in agreement with what was found from the pcT absorption measurements. But in both cases, the weight loss in the second decomposition is larger than the calculated amount of absorbed gas, verifying that the samples had not been completely decomposed. Secondly, the endothermic decomposition event has its maximum at 338.7°C for *LaLiBack* compared to 334.3°C for *a.m. LaLi*, and even later, 368.1°C for *LaLiVac*. The fact that this event closely follows the weight loss verifies that it indeed is the decomposition of $LiBH_4$. Moreover, this is the only calorimetric event which is significantly different among the three samples, and according to Züttel et al.[23], the only one which is pressure dependent. All DSC-TGA samples were measured at atmospheric pressure, and this difference must therefore originate in the different reactive additives in the samples which give different enthalpy of decomposition and consequently different decomposition temperatures. The additives present in the *LaLiBack* sample are obviously preferable with respect to decomposition temperature, although the weight loss is approximately halved. It was found that the SR-PXD hydrogenated *LaLiBack* sample contained much more $LaH_{2+\delta}$ than the *LaLiVac* sample. This proves that $LaH_{2+\delta}$ indeed forms a reactive hydride composite with $LiBH_4$ and lowers the temperature of decomposition.

For the *YbLi* cycle experiments, shown in figure 5.24, we observe much of the same features, although a major endothermic decomposition event is lacking. We here have measurements from the *as-decomposed YbLiBack*, plotted with dash-dot lines. The TGA trace is quite similar to hydrogenated *YbLiVac*, with a weight loss of 2.25 wt%, obviously verifying that the sample had not decomposed completely. However, the pcT calculations indicated that more gas was absorbed after vacuum decomposition ($\approx$ 2.5 wt%) than after back pressure decomposition ($\approx$ 1.3 wt%) so that this coincidence is possibly accidental. Finally, the hydrogenated *YbLiBack* sample does hardly release any gas at all. The unphysical weight increase must be due to experimental errors, such as insufficient

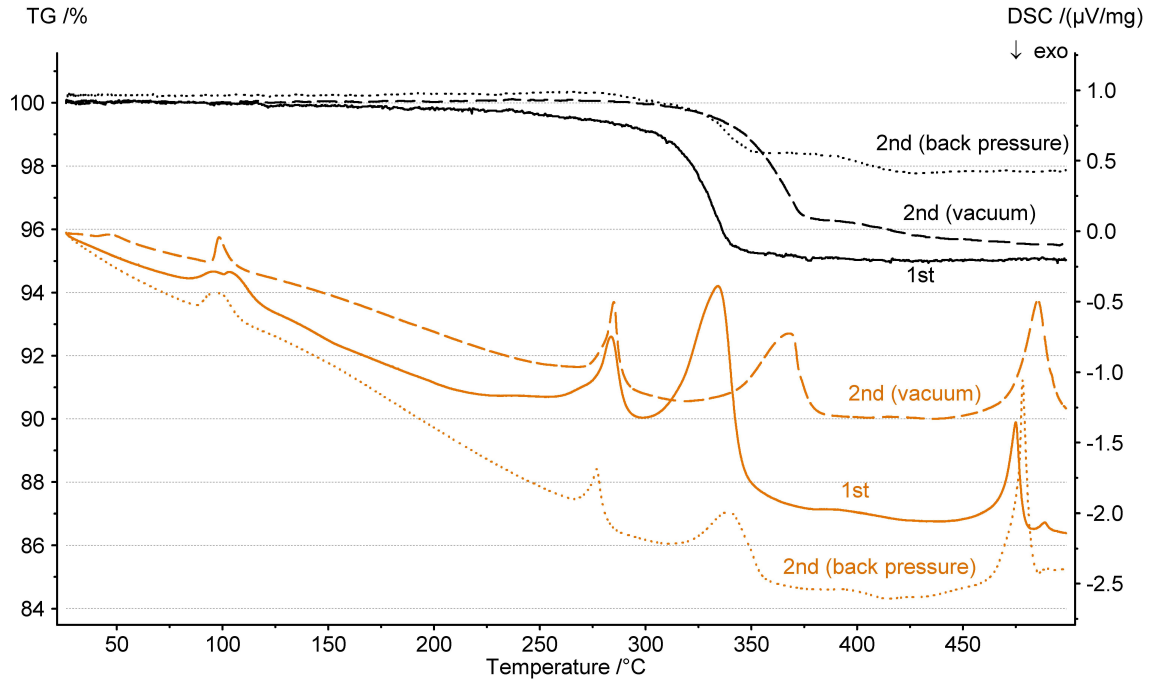


Figure 5.23: 1st DSC-TGA desorption of a.m. *LaLi* and 2nd DSC-TGA desorption of hydrogenated *LaLiVac* and *LaLiBack*

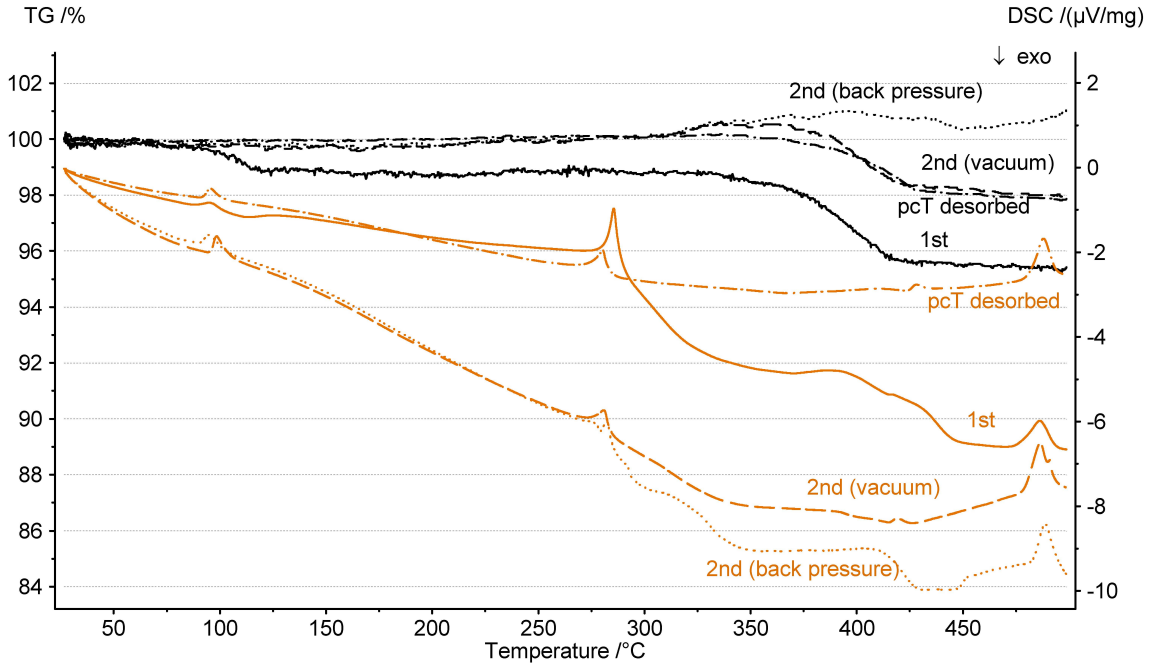


Figure 5.24: 1st DSC-TGA desorption of a.m. *YbLi*, DSC-TGA of pcT-desorbed *YbLiBack* and 2nd DSC-TGA desorption of hydrogenated *YbLiVac* and *YbLiBack*

background correction. Therefore, this measurement was repeated, with no big success: Less gas was released than from the decomposed sample, which actually means that the sample must have lost hydrogen during the hydrogenation experiment in some way, which

also is not very plausible. Therefore, the following IR results of the same sample will be of use in determining the nature of the reactions.

### IR measurements of cycled samples

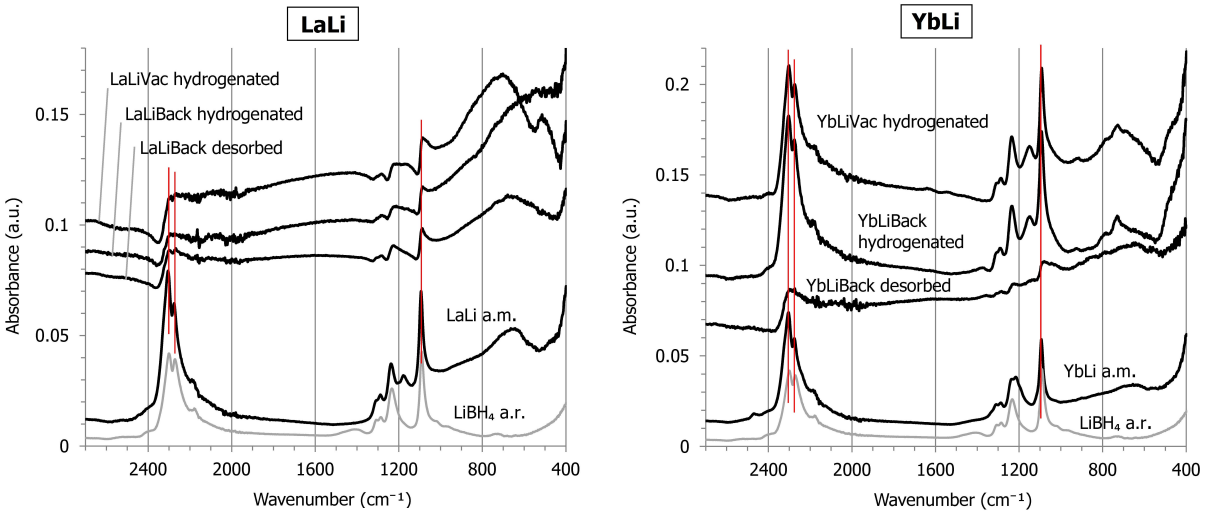


Figure 5.25: IR measurements of the three cycling stages of *LaLi* (left) and *YbLi* (right): The a.m. sample, the back pressure pcT-decomposed sample and both of the hydrogenated samples.

In figure 5.25, the vibrational spectra of the *as-milled*, desorbed and hydrogenated *LaLi* (left) and *YbLi* (right) are presented. For comparison, the spectrum of pure $LiBH_4$ is shown below in gray.

Both the as-milled samples resemble to a great extent the spectrum of pure $LiBH_4$. The common peaks were found at almost the same wavenumbers, listed in table 5.10. The two intense stretching modes $\nu_3'$ and $\nu_3''$ of the borohydride group are marked with red lines. Also a small contribution from the first overtone of the bending frequency $2\nu_4''$ is visible. In the region of the H-B-H bending modes, $\nu_2'$, $\nu_2''$ (both very weak), $\nu_4'$ and $\nu_4''$ (strong) are identified, the latter marked with a red line. The modes in a.m. *LaLi*

Table 5.10: Vibrational modes found in the *as-milled* *LaLi* and *YbLi* samples in figure 5.25, compared with the measured wavenumbers for pure $LiBH_4$. The uncertainty is $\pm 1$ $cm^{-1}$

| Mode | | Wavenumber ($cm^{-1}$) | | |
|---|---|---|---|---|
| | | $LiBH_4$ | a.m. *LaLi* | a.m. *YbLi* |
| $\nu_2''$ | Antisymmetric bending | 1286 | 1287 | 1288 |
| $\nu_2'$ | Symmetric bending | 1307 | 1309 | 1309 |
| $\nu_3''$ | Antisymmetric stretching | 2271 | 2275 | 2276 |
| $\nu_3'$ | Symmetric stretching | 2300 | 2304 | 2304 |
| $\nu_4''$ | Antisymmetric bending | 1090 | 1092 | 1093 |
| $\nu_4'$ | Symmetric bending | 1233 | 1237 | 1236 |
| $2\nu_4''$ | Antisymmetric bending overtone | 2179 | 2189 | 2189 |

and *YbLi* were all found at slightly higher wavenumbers than for $LiBH_4$. This systematic offset could be explained by impurity phases in the sample. In any case, these results clearly verify that there was a large portion of $LiBH_4$ in both the *LaLi* and the *YbLi* sample.

There is an additional peak in the bending region of a.m. *LaLi* at 1178 $cm^{-1}$, which is absent in the spectrum of a.r. $LiBH_4$. The relative intensity of $\nu_3'$ and $\nu_3''$ is also changed, which indicates a modification of the stretching modes as well. It could be speculated that this originates from the $LiLa(BH_4)_3Cl$ phase, since this borohydride was still present in small amounts after synthesis. The similar $LiCe(^{11}BD_4)_3Cl$ borohydride has been studied with IR spectroscopy[40], and it was found that the $\nu_2''$ mode was shifted 31 $cm^{-1}$ towards lower wavelengths compared to pure $Li^{11}BD_4$. The $\nu_2'$ mode was shifted 17 $cm^{-1}$. This shift was speculated to originate in weakening of the cation-boron bonding due to increased cation electronegativity. The increased separation between the peaks could indicate distorted coordination and altered bond lengths. $LiLa(BH_4)_3Cl$ should exhibit the same modifications, since the electronegativity of cerium ($\chi_P = 1.12$) is very equal to that of lanthanum ($\chi_P = 1.10$)[34]. Averaged with the electronegativity of $LiBH_4$ ($\chi_P = 0.98$), the cation electronegativities become 1.04 and 1.05 for $LiLa(BH_4)_3Cl$ and $LiCe(BH_4)_3Cl$ respectively.

In the a.m. *YbLi* sample, there is a similar additional peak at 1216 $cm^{-1}$. This also fits with the above proposed shift for the $\nu_2$ mode, although the mixed-metal borohydride present this time is $Yb(BH_4)_{2-x}Cl_x$, with a cation electronegativity of 1.1. The chlorine substitution might on the other hand balance out this increased charge transfer towards the ytterbium atom.

When considering the other *LaLi* samples, is it seen that both the desorbed and the hydrogenated samples exhibit spectra with weak remnants of the same vibrations. The bending and stretching frequencies are not fully recovered after hydrogenation. The "dips" observed around $\nu_3''$ and $\nu_4''$ are probably amplifications of boundary effects due to too little sample on the crystal surface. But in case of hydrogenated *LaLiVac*, the new peak at 1178 $cm^{-1}$ emerges again, indicating some reversibility of the compound containing this mode.

The *YbLi* sample, however, show remarkable reversibility. There are still vibrational modes observed in the back pressure decomposed *YbLi* sample, which is in agreement with the incomplete decomposition of the sample. The spectrum of lithium borohydride is fully restored after hydrogenation of both *YbLiVac* and *YbLiBack* samples, this time with the peak at 1178 $cm^{-1}$. Whereas the hydrogenation of *LaLiVac* leads to the formation of a compound, possibly $LiLa(BH_4)_3Cl$, that can decompose in the second cycle, the results for *YbLi* are partially conflicting with the DSC-TGA measurements of the same samples, because hydrogenated *YbLiBack* did not release gas upon heating. It is reminded that the TGA curve of hydrogenated *YbLiBack* was uncertain because of an apparent weight increase and large fluctuations. Together with the clear evidence of absorption provided by the pcT measurements, lithium borohydride is considered to be reversible in the *YbLi* sample. A possible explanation of the absent weight loss is that some new borohydride is formed in hydrogenated *YbLiBack* which is more stable than $LiBH_4$, but this has not been investigated further.

# Discussion

The motivation for research on lightweight hydrogen storage materials is mainly their possible applications in mobile energy consuming devices. In such systems, the enthalpy of decomposition must be low, not only to make the hydrogen available without consuming too much energy, but also to avoid vast amounts of heat being generated when the hydrogen is loaded and the storage material reassembled.

In this work, two different techniques of lowering the decomposition enthalpy of a promising lightweight host have been studied: The $6LiBH_4 + LnCl_3$ (Ln=La, Yb) samples consist of a mixture of $LiBH_4$ and $LiLn(BH_4)_3Cl$, and can thus be classified as mixed-metal borohydride composites. The $6LiBH_4 + LnCl_3 + 3LiH$ samples were synthesized in order to have only $LiBH_4$ and $LnH_{2+\delta}$ hydrides present, and can be classified as reactive hydride composites. It has been focused on the synthesis processes and decomposition pathways of both types of materials, and the reversibility of the reactive hydride composites was in particular investigated. We will in the following summarize the important results and evaluate the four composites as possible hydrogen storage materials.

Both the mixed-metal borohydride composites *La* and *Yb* have been synthesized according to the proposed common metathesis reaction, with some exceptions: The required milling time for synthesis of a rare-earth based borohydride increases with increasing ionic radius of the rare-earth element, and the synthesis of the lanthanum-based composite was therefore not completed. However, the metathesis reaction was re-activated upon heating to around 96°C, and from there on, the sample composition was correct. Negligible amounts of hydrogen gas was released during milling. Under the synthesis of the ytterbium-based composite, a large amount of diborane and hydrogen gas (2.0 wt%) was lost, originating in the reduction from trivalent to divalent ytterbium borohydride. Except for this was the metathesis reaction for the *Yb* sample more or less completed.

In the *La* composite, $LiLa(BH_4)_3Cl$ decomposed from 200°C *via* an unknown intermediate into $LaH_{2+\delta}$, which in turn formed a reactive hydride composite with $LiBH_4$ and decomposed at around 300°C. The hydrogen release started already at 150°C and 5.0 wt% had been released at 350°C. The unknown intermediate product of $LiLa(BH_4)_3Cl$ was assumed to finally decompose at 264°C (1 bar) and release a major amount of hydrogen. For comparison, $LiCe(BH_4)_3Cl$ was reported[40] to decompose at 246°C (1 bar). This difference is in good agreement with the slightly different averaged cation electronegativities 1.04 and 1.05 of $LiLa(BH_4)_3Cl$ and $LiCe(BH_4)_3Cl$ respectively: Inserted into equation 3.20, the resulting difference in $\Delta H_f$ between the two compounds is around 2.5 kJ/mol $BH_4$, which gives a decomposition temperature difference of 10-20 °C, naturally depending on what end products are formed. One should note that even very small electronegativity differences may lead to a significant altering of the decomposition temperature.

It can be speculated that the proposed[39] intermediate $Ce_2(B_{12}H_{12})$ in the $LiCe(BH_4)_3Cl$ decomposition also forms here, with lanthanum instead of cerium:

$$LiLa(BH_4)_3Cl \rightarrow \frac{1}{4}La_2(B_{12}H_{12}) + LiCl + \frac{1}{2}LaH_{2+\delta} + 4H_2 \quad (6.1)$$

This hydrogen release will constitute 1.1 wt% of the composite and corresponds well to the gradual mass loss between 150 and 250°C. Further decomposition of $\frac{1}{4}La_2(B_{12}H_{12})$ might result in the formation of $\frac{1}{2}LaB_6 + \frac{3}{2}H_2$, but this can not be confirmed at present. An additional 50% chlorine substitution into $LiBH_4$ would give a total mass loss of 4.6 wt% which still requires that $LiBH_4$ is decomposed through an alternative reaction with $LaH_{2+\delta}$ (or another decomposition compound). This decomposition was however not covered by the SR-PXD data, and neither the final decomposition pathway nor the reversibility are therefore revealed. But other hydrogenation experiments performed at IFE indicated that almost half of the hydrogen capacity can be recovered by exposing the sample to 100 bar and 400°C for 24 hours. The $6LiBH_4 + LaCl_3$ composite thus offers a decent dehydrogenation temperature ($150 - 350$°C) and relatively large storage capacity (5.5 wt%), but suffer from poor reversibility.

The $6LiBH_4 + YbCl_3$ composite is of little interest in the first place because the mixed-metal borohydride $LiYb(BH_4)_{4-x}Cl_x$ decomposes into $Yb(BH_4)_{2-x}Cl_x$, diborane and hydrogen both under synthesis and under heating to around 130°C. The reaction enthalpy of this reduction reaction must be relatively low, since it occurs at such a low temperature. The electronegativity of $Yb^{2+}$ is 1.1, making $Yb(BH_4)_{2-x}Cl_x$ less stable than $LiLa(BH_4)_3Cl$ if the chlorine content is about the same. The higher decomposition temperature of $Yb(BH_4)_{2-x}Cl_x$ must therefore originate from less stable end products. For example, boron has been lost as diborane which could make the formation of $YbB_6$ unfavorable. The decomposition temperature was also observed to vary less with the pressure than that of the the $LiLa(BH_4)_3Cl$ decomposition, verifying that $\Delta H$ was higher in the ytterbium case. The consequence is that the second hydrogen release took place much later (340-350°C) than for the lanthanum composite. But still, $LiBH_4$ was decomposing at a lowered temperature due to an alternative pathway, although the final products could not be verified with the present SR-PXD data.

The mixed-metal borohydride samples show a common interesting feature: The effect of an unstable mixed-metal borohydride that decompose at lower temperatures is combined with a lowering of the decomposition enthalpy of an alkali borohydride because the decomposition products of the former form a reactive hydride composite with the latter.

The synthesis of the reactive hydride composites *LaLi* did not complete either; $LaCl_3$ was still present, $LaH_{2+\delta}$ did not form and no gas was released during synthesis. It is therefore odd that the refinements indicated a 17% increase of $LiBH_4$, since this has to be taken from $LiLa(BH_4)_3Cl$ and the added 3LiH, with either hydrogen gas or lanthanum-hydrogen containing species as a result. Only the latter is in agreement with the GTM results. The first metathesis reaction (5.1) was again activated at around 95°C, and luckily, so was also the second reaction (5.2) at around 200°C, producing $LaH_{2+\delta}$ which allowed the desired decomposition to take place.

The decomposition under vacuum of *LaLi* showed a pathway similar to that of the cerium reactive hydride composite. The hydrogen release slowly started at 200°C, and at 334°C, $LiBH_4$ reacted with $LaH_{2+\delta}$ and decomposed *via*

$$6LiBH_4 + LaH_{2+\delta} + 3LiCl \rightarrow 6LiH + LaB_6 + (10 + \frac{\delta}{2})H_2 + 3LiCl \quad (6.2)$$

Reaction 6.2 releases 5.05 wt% of only hydrogen gas, in very good agreement with

the experimental findings. This occurs now at a later temperature and releases less hydrogen than the lanthanum mixed-metal composite, and the payoff should be increased reversibility, as was previously stated. However, the SR-PXD hydrogenation series, the pcT hydrogenations and calculations of absorption and the IR measurements of the hydrogenated samples all indicate a limited reversibility and absorption capacity (estimated uptake approximately 2 wt%). The lanthanum mixed-metal borohydride composite is therefore preferable over the reactive hydride composite which severely fails to meet the criteria of low decomposition enthalpy and good reversibility.

Nevertheless, the different decomposition temperatures observed among the cycled *LaLi* composites are worth discussing. It was seen in the SR-PXD series that back pressure inhibited the decomposition reaction severely. This becomes obvious when the van't Hoff equation (3.17) is considered. If we assume that the entropy change of the hydrogen desorption is approximately the same as for pure lithium borohydride (around 164 $\frac{\mathrm{J}}{\mathrm{Kmol}}$), the increase in decomposition temperature by a pressure increase from 1 to 5.4 bar becomes

$$\frac{T(5.4 \text{ bar})}{T(1 \text{ bar})} = \frac{1}{1 - \frac{R}{\Delta S} ln(5.4)} = 1.093 \tag{6.3}$$

i.e an increase of 9.3%. It is therefore no mystery that the decomposition did not commence in the back pressure series. Actually, in the vacuum series, the event was barely reached before the heating ended. Moreover, under back pressure decomposition in the pcT-apparatus, the system was closed and consequently the pressure rose to around 10 bar at the end of the heating. This would increase the decomposition temperature by 13%. A vacuum pressure of 10 mbar should similarly decrease the decomposition temperature by 19%, but this effect has not been observed, probably due to slow kinetics.

Why the two hydrogenated *LaLi* composites have different decomposition temperatures at 1 bar (referring to the DSC-TGA measurements of cycled samples), was explained by different amounts of $LaH_{2+\delta}$: The decomposition 6.2 has evidently been inhibited under back pressure, and there was thus more $LaH_{2+\delta}$ present in the hydrogenated *LaLiBack* composite which could form a reactive hydride composite with undecomposed $LiBH_4$ in the second decomposition. In the decomposition of *LaLiVac*, the lanthanum hydride was more or less gone and the enthalpy of decomposition was correspondingly higher. This conclusion is in some sort of agreement with the previously studied $6LiBH_4 + CeCl_3 + 3LiH$ composite, in the sense that back pressure decomposition improves the reversibility of the system. What in fact happens, is simply that more lanthanum hydride (and lithium borohydride) is preserved such that it takes part in the second decomposition as well. The seemingly improved reversibility is thus considered to be artificial.

*YbLi* was very successfully synthesized, except of the mentioned problem that large amounts of hydrogen and diborane gas were lost during milling. A decomposition pathway similar to equation 6.2 could not be verified with the SR-PXD, although it was found that $LiBH_4$ decomposes a little earlier ($350 - 400°C$) than pure $LiBH_4$, presumably due to lesser stable boron-ytterbium end products. The *ex-situ* hydrogenation experiments clearly indicate that more hydrogen gas was absorbed into the vacuum decomposed composites (2.1 - 2.5 wt%) than into the back-pressure decomposed composites (0.9 - 1.3 wt%), meaning that the latter had not decomposed completely. The gas release from hydrogenated *LaLiBack* during the second DSC-TGA decomposition is thereby explained. The IR measurements strongly indicate that $LiBH_4$ could be re-formed during hydrogenation, but the TGA trace from the decomposition of hydrogenated *YbLi* composites

did hardly show any weight loss although the calorimetric trace behaved similarly to the corresponding as-milled composites. This is apparently contradicting, but an explanation might be that destabilizing agent $YbH_2$ is lacking. The $YbLi$ reactive hydride composite is therefore considered to be partially reversible under the present conditions.

Although the synthesis problems with the ytterbium reactive hydride composite are overcome and remnants of mixed-metal borohydrides completely eliminated, this composite has still a too high decomposition temperature at 1bar and too low storage capacity for mobile applications.

Rare earth chlorides are at the moment very expensive (around 1000 NOK/g). They can be used as dopants or catalysts, but in a reactive hydride composite or a mixed-metal borohydride, the solutions should ideally provide so important advantages over cheaper storage materials that this compensates for the high cost. For the composites studied here, this is not the case. One can only imagine that they can be sold as niche products for applications that have very specific technical constraints.

But still, the field is interesting from a basic research viewpoint, because the techniques that are applied to tune the thermodynamic properties of complex hydrides work very well for rare-earth based additives. As transition metals hardly form stable borohydrides or well-behaving reactive composites, almost all the rare-earth elements have shown to form numerous borohydrides by mechanochemistry or wet chemistry, and rare-earth based additives actively take part in and alter sorption reactions of hosts like lithium borohydride.

# Conclusions

Ball-milling of $6LiBH_4+LaCl_3$ for 5 h at 400 rpm leads to the formation of the mixed-metal borohydride $LiLa(BH_4)_3Cl$. The metathesis reaction is not completed, but is re-activated upon heating to 96°C. Further milling with 3LiH for 1 h and subsequent heating to around 200°C produces the reactive hydride composite $6LiBH_4 + LaH_{2+\delta}$. Similarly, milling of $6LiBH_4 + YbCl_3$ leads to the formation of $LiYb(BH_4)_{4-x}Cl_x$, $Yb(BH_4)_{2-x}Cl_x$ and 2.0 wt% of $B_2H_6$ and $H_2$ gas. Continued milling with 3LiH for 1 h produces $6LiBH_4 + YbH_{2+\delta}$ and additionally 0.7 wt% of $B_2H_6$ and $H_2$ gas. LiCl is formed as by-product in all composites. In case of ytterbium, $\delta$ was estimated to be 0.6. The syntheses were shown to be reproducible.

Common for the *as-milled* $6LiBH_4+LnCl_3$ (Ln=La, Yb) composites is that the mixed-metal borohydrides decomposes first (from 150°C and 130°C for Ln=La and Yb, respectively), and that their product $LnH_{2+\delta}$ reacts with remnant $LiBH_4$. The latter subsequently decomposes at a lower temperature (approximately 300 and 366°C for Ln = La, Yb) compared to pure $LiBH_4$. For Ln=La, only hydrogen is released and constitutes in total 5.5wt%. For Ln=Yb, large amounts of diborane are released.

In the reactive hydride composites, $LiBH_4$ is similarly reacting with $LnH_{2+\delta}$ and decomposes around 334°C (Ln=La) and 380°C (Ln=Yb). Formation of $LaB_6$ and LiH was verified in case of Ln=La. Hydrogen release starts at approximately 200°C (Ln=La) and 300°C (Ln=Yb) and constitutes 5.0 and 4.5 wt%, respectively. The loss of diborane is suppressed for Ln=Yb. Decomposition under back pressure increases the decomposition temperature according to the van't Hoff equation.

Both the $6LiBH_4 + LnH_{2+\delta}$ hydride composites are partially reversible. After decomposition under vacuum, the composites absorb approximately 2 wt% $H_2$ in case of Ln=La, and 2.1 - 2.5 wt% $H_2$ in case of Ln=Yb. For the latter, $LiBH_4$ was observed by IR to reform after desorption and hydrogenation, but released almost no gas during the second decomposition, probably due to the absence of $YbH_{2+\delta}$.

Both the ytterbium-based composites releases diborane under synthesis and decomposition, and are therefore little attractive as hydrogen storage materials. Of the lanthanum-based materials, the mixed-metal borohydride composite releases more hydrogen at a lower temperature than the reactive hydride composite, and is therefore preferable since the latter shows poor reversibility.

# Abbreviations

| | |
|---|---|
| PXD | Powder X-ray Diffraction |
| SR-PXD | Synchrotron Radiation Powder X-ray Diffraction |
| PND | Powder Neutron Diffraction |
| BM01 | Beam Line One |
| ESRF | European Synchrotron Radiation Facility |
| DSC | Differential Scanning Calorimetry |
| TGA | Thermogravimetric Analysis |
| RGA | Residual Gas Analysis |
| a.m. | *As-milled* |
| a.r. | *As-recieved* |
| wt% | Weight percent |

# Appendices

# Leakage considerations

Here, we argue that the pressure in a leaking container will drop linearly for high initial pressures and small pressure changes.

Let $n_1$ moles of gas at temperature $T$ and pressure $p >> p_a$ be enclosed in a compartment of constant volume $V$. At time $t = 0$, a hole of areal $A$ is made in the container wall. The gas is assumed to be incompressible and the flow is assumed to be frictionless and isothermal. To simplify, we will assume the ambivalent temperature to be $T$ as well, which is a fair assumption at least for the pcT manifold. The amount of gas which has left the container at a later time $t$ is $n_2$, its volume (imagine it is filling an extremely elastic balloon) is $V_2$ and the pressure is atmospheric, $p_a$. The total amount of gas at any time will be

$$n = n_1 + n_1 = \frac{p(t)V + p_a V_2(t)}{RT} \tag{A.1}$$

and taking the time derivative of this equation yields

$$0 = V\frac{dp}{dt} + p_a\frac{dV_2}{dt} \tag{A.2}$$

The time change of $V_2$ is now equal to the volume flow out of the hole,

$$\frac{dV_2}{dt} = vA \tag{A.3}$$

where $v$ is the instantaneous gas velocity averaged over the velocity profile of the hole. By applying the Bernoulli equation between a point of almost no gas movement in the container and a point in the middle of the hole, and further assume that the elevations present in the system are negligible, we find that

$$\frac{p}{\rho g} = \frac{1}{2}v^2 \tag{A.4}$$

Here, $\rho$ is the constant gas density and g the gravity of Earth. Inserting A.3 and A.4 into equation A.2 yields the first-order nonlinear ordinary differential equation

$$\frac{dp}{dt} = -\frac{Ap_a}{V}\sqrt{\frac{2}{\rho g}}\sqrt{p} \tag{A.5}$$

which is solved by direct integration:

$$\int \frac{1}{\sqrt{p}}dp = -\frac{Ap_a}{V}\sqrt{\frac{2}{\rho g}}\int dt \tag{A.6}$$

giving the polynomial solution

$$p(t) = p_0 - \frac{Ap_a}{V}\sqrt{\frac{2p_0}{\rho g}}t + \left(\frac{Ap_a}{V}\right)^2 \frac{1}{2\rho g}t^2 \tag{A.7}$$

where the initial condition $p(t = 0) = p_0$ is used. This solution is obviously only valid under the above stated approximations, which are believed to be valid for the pcT system. A more correct calculation would take adiabatic expansion into account, this however gives a much more complicated differential equation to solve and is not necessary here. By inserting $\rho_H = 8.99 \cdot 10^{-5} kg/L$, $g = 9.81 m/s^2$ and assuming that the initial pressure is $p_0 = 100$ bar we get

$$p(t) = 5.67\left(\frac{Ap_a}{V}\right)^2 t^2 - 47.6\left(\frac{Ap_a}{V}\right) t + 100 \qquad [p] = bar \tag{A.8}$$

In equation A.8, $(\frac{Ap_a}{V})$ has the same power as $t$ in each term which means that the size of the hole, the container volume and surprisingly also the ambivalent pressure only affect the time scale of the leakage, and the curve shape is only dependent on the pressure range. For pressure changes from $t = 0$ up to 20 bar, the quadratic term is negligible (for a drop from 100 to 80 bar, $(\frac{Ap_a}{V}) = 0.44$), and consequently, the pressure will drop linearly with time.

# Refinement data

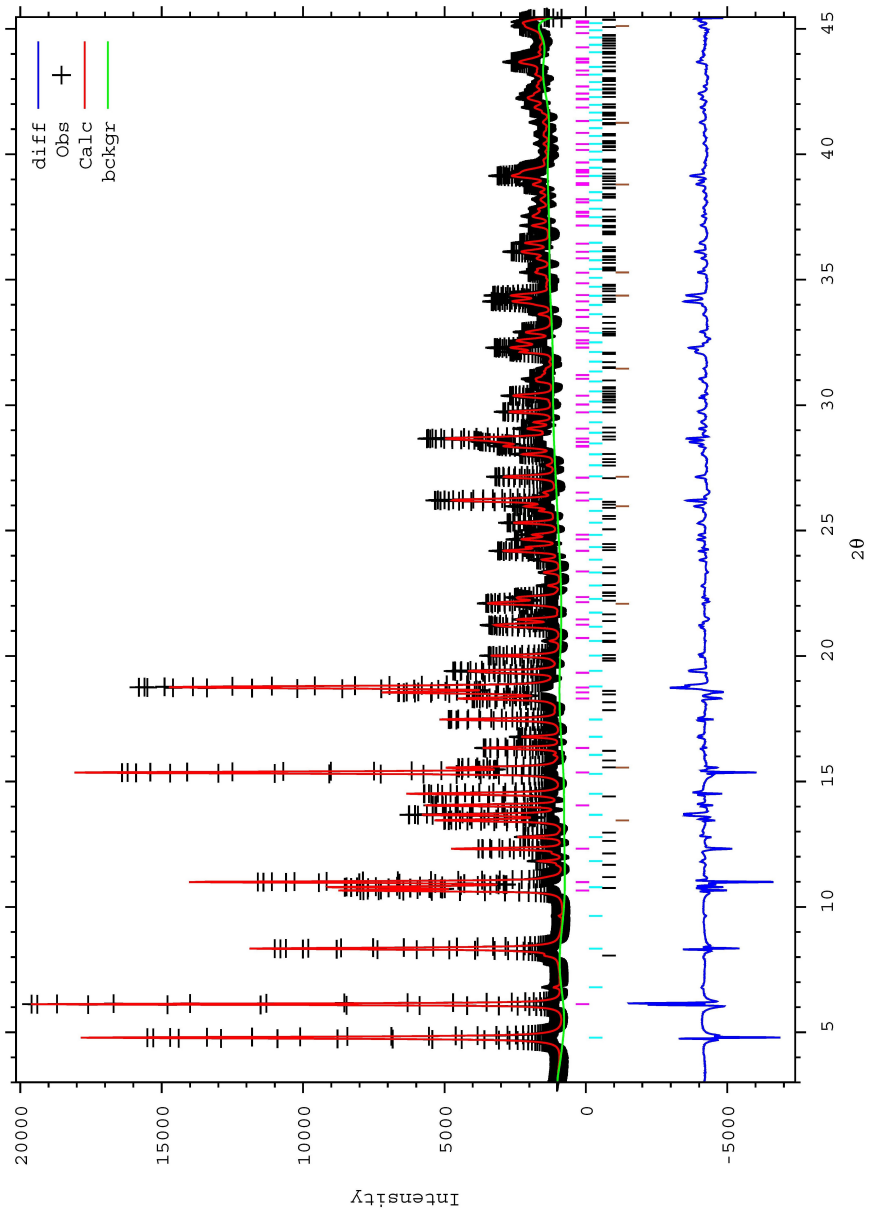


Figure B.1: Refinement of the a.m. *La* sample. $R_{wp} = 6.77\%$, $R_p = 5.02\%$, $S_{wp} = 8.285$. 41 variables were refined, among 24 were terms in a shifted Chebyshev background polynomial.

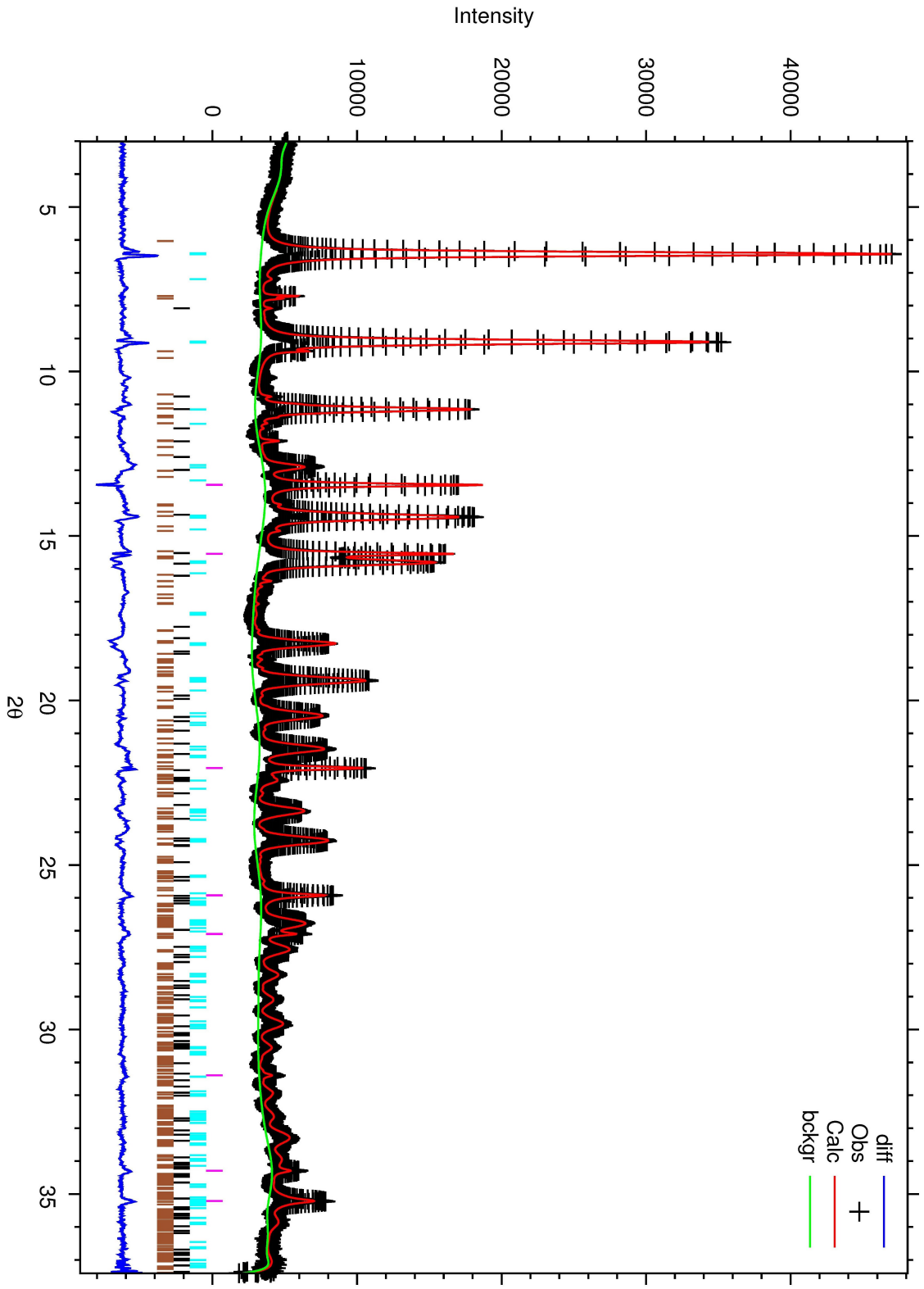


Figure B.2: Refinement of the a.m. $Yb$ sample. $R_{wp} = 4.35\%$, $R_p = 3.32\%$, $S_{wp} = 9.378$. 50 variables were refined, among 36 were terms in a shifted Chebyshev background polynomial.

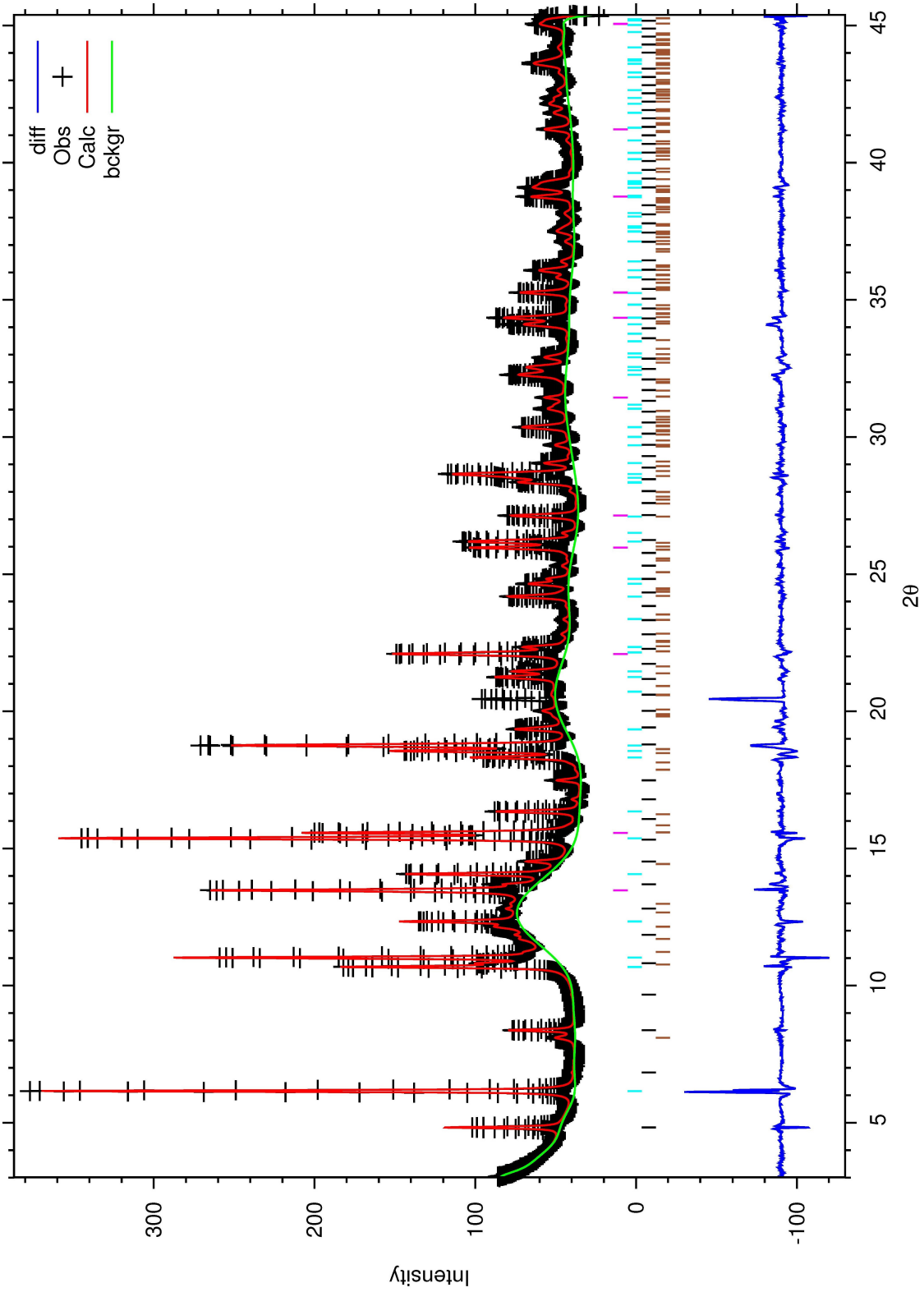


Figure B.3: Refinement of the a.m. *LaLi* sample. $R_{wp} = 4.19\%$, $R_p = 2.39\%$. Background points were selected manually.

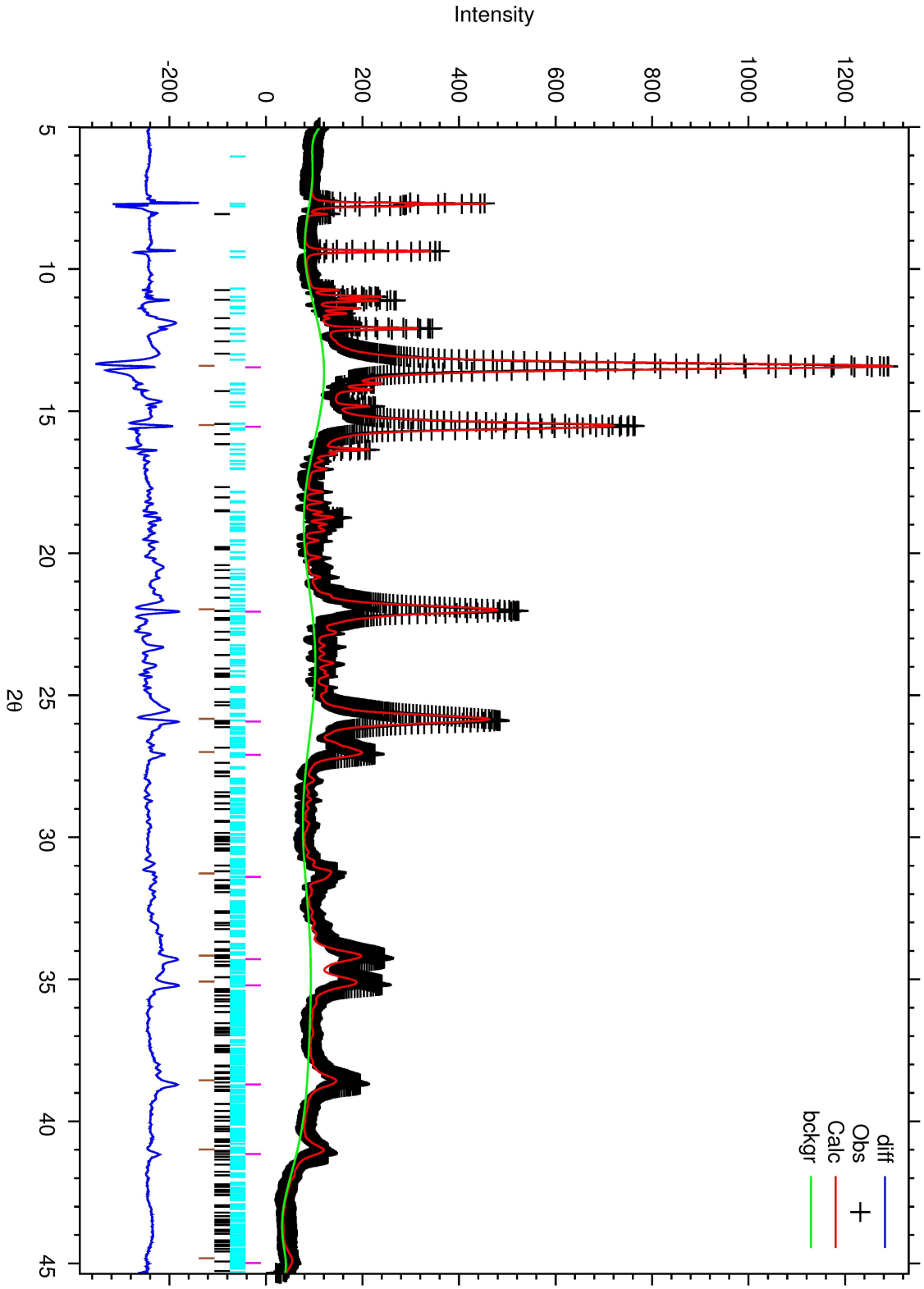


Figure B.4: Refinement of the a.m. $YbLi$ sample. $R_{wp} = 5.59\%$, $R_p = 4.17\%$. Background points were selected manually.

# Color photo gallery

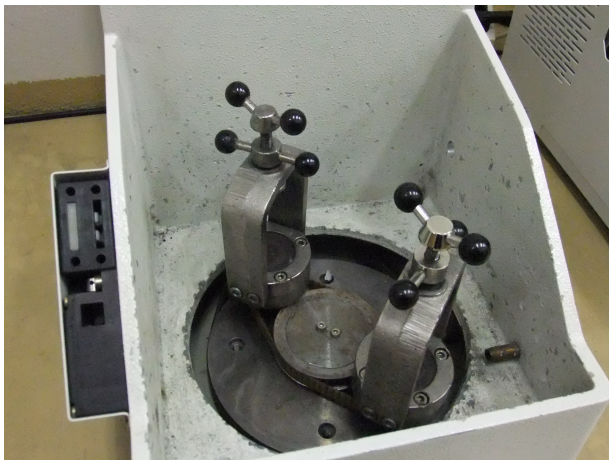

Figure C.1: Inside the Fritsch planetary ball mill


Figure C.2: Outside the Fritsch planetary ball mill

Figure C.3: The grinding bowls, the lids, the balls, the metal frames and the gaskets

Figure C.4: The MBraun Unilab glovebox

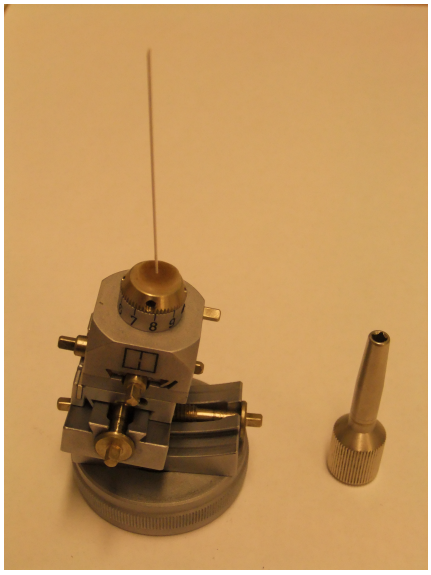

Figure C.5: The Hilgenberg capillary fastened to the Bruker sample holder

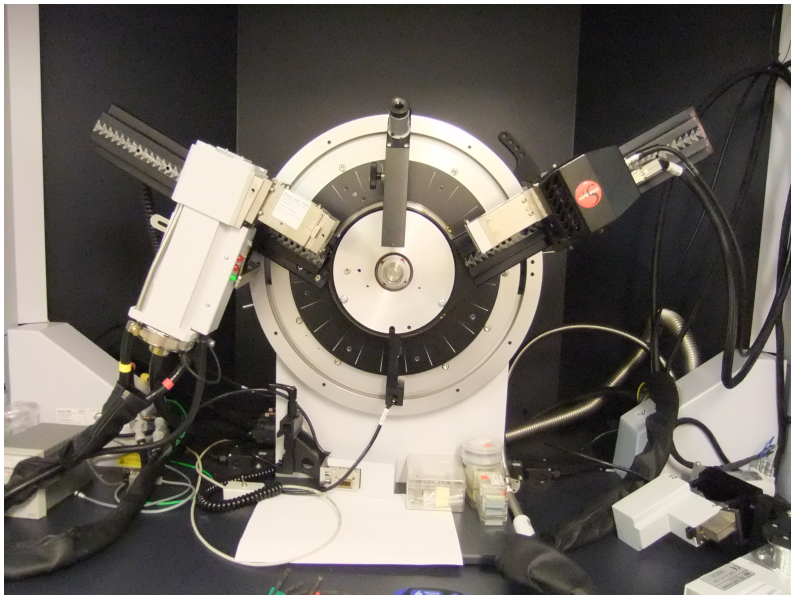

Figure C.6: The Bruker AXS D8 Advance diffractometer

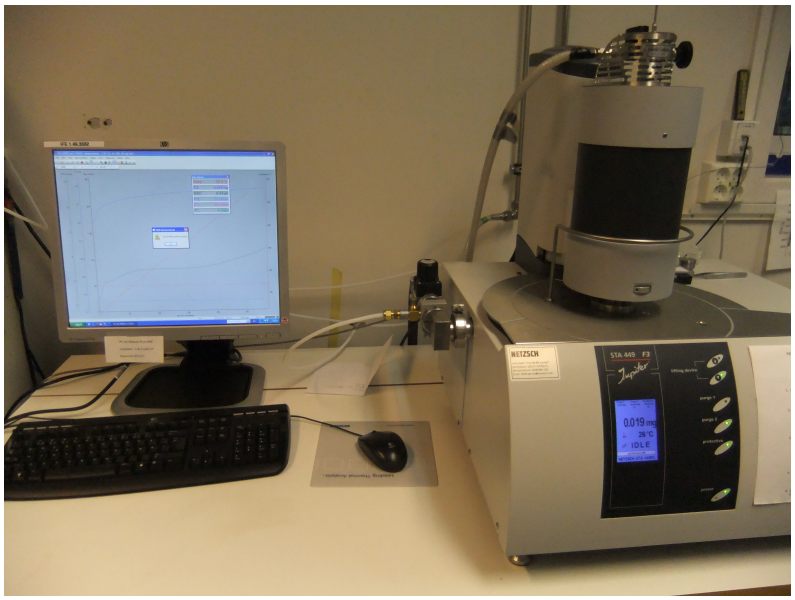

Figure C.7: The Netzsch STA 449 *F3* Jupiter apparatus

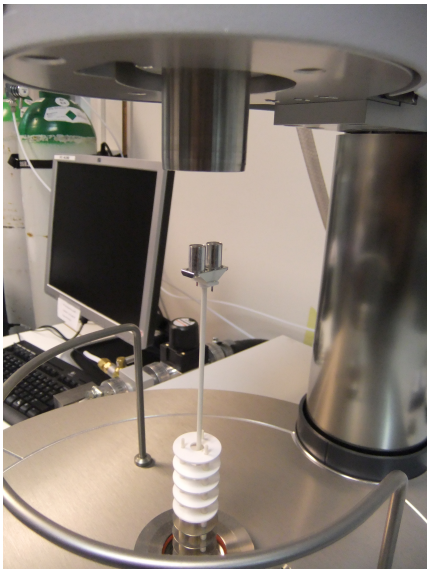

Figure C.8: Sample and reference crucibles of platinum. The furnace is elevated

Figure C.9: The view inside the ESRF synchrotron

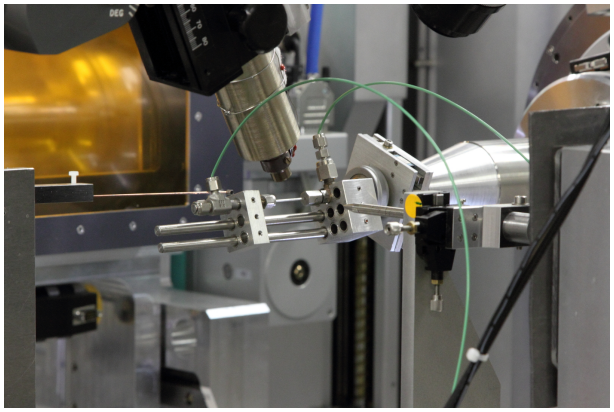

Figure C.10: The collimated ray outlet, the sample holder, the PILATUS detector in the background, the gas blower above the sample and the IR camera below the sample

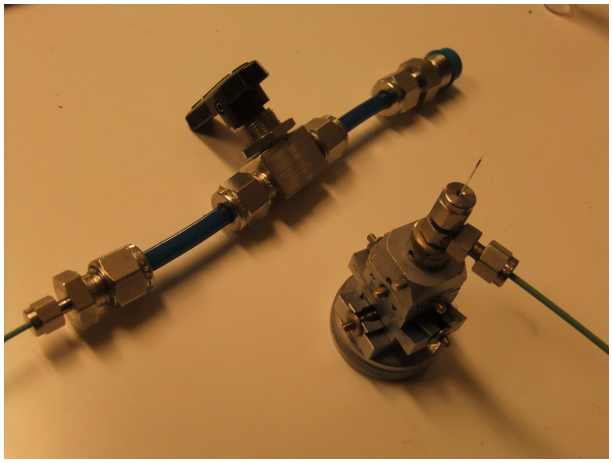

Figure C.11: The sample holder with a pressure tubing connection

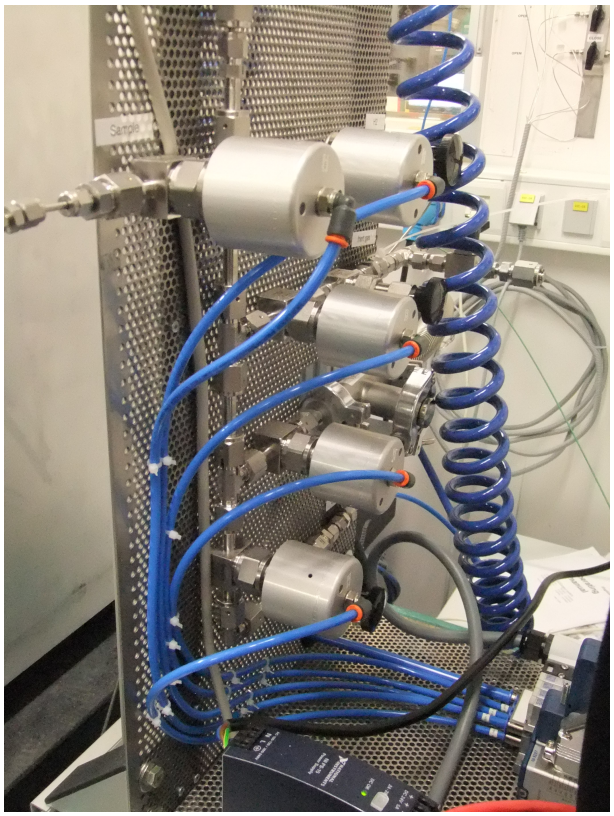

Figure C.12: The IFE-build gas rig

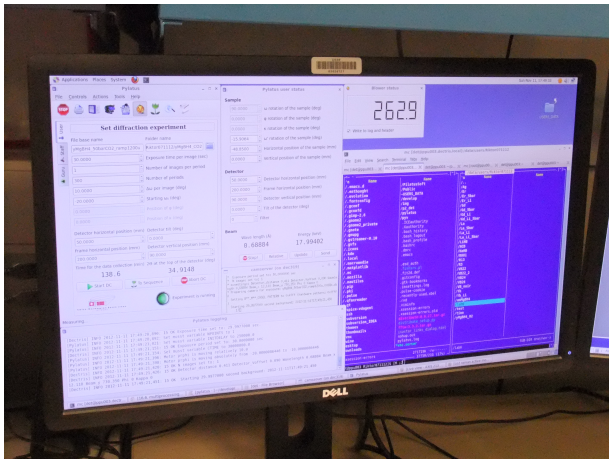

Figure C.13: The special-tailored Pylatus software

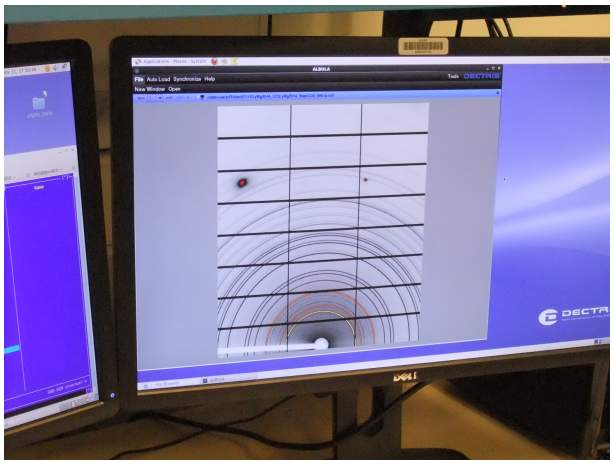

Figure C.14: A picture from an experiment in the Pylatus software

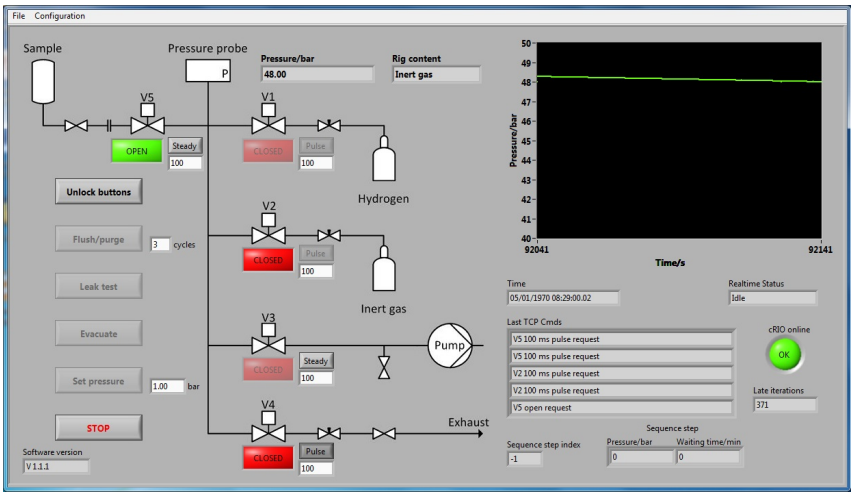


Figure C.15: The special-tailored LabView gas rig software

# Bibliography


[1] Homepage of NEL Hydrogen, 29.04.13 <http://www.nel-hydrogen.com/home/?pid=70>

[2] Homepage of University of Michigan, Materials Science and Engineering, 29.04.13 <http://www.mse.engin.umich.edu/people/peterjon/projects/hecam-hydrogen-energy-with-carbon-materials/>

[3] Hauback, B. C.: *Materials for hydrogen technology. Metal hydrides.* Lecture notes for MENA3200, UiO, 2010

[4] Homepage of Daimler AG, 29.04.13 <http://media.daimler.com/dcmedia/0-921-1417474-1-1422684-1-0-0-1422684-0-1-11702-0-0-1-0-0-0-0-0.html?TS=1367222448562>

[5] Mori, et al.: *Hydrogen-Storage Materials for Fuel Cell Vehicles. High-pressure MH System.* J. Japan Inst. Metals, 2005, **69** 3, 308-311

[6] Walker, G.: *Solid-State hydrogen storage. Materials and chemistry.* Woodhead Publishing Limited, Cambridge, 2008

[7] Homepage of U. S. Department of Energy, 26.04.13 <http://www1.eere.energy.gov/hydrogenandfuelcells/storage/pdfs/targets_onboard_hydro_storage_explanation.pdf>

[8] Zumdahl, S. S.: *Chemical Principles.* Houghton Mifflin Company, 6th edition, 2009

[9] Züttel, A. and Schlapbach, L.: *Hydrogen-storage materials for mobile applications.* Nature, 2001, **414**, 353-358

[10] Li, H. et al.: *Recent Progress in Metal Borohydrides for Hydrogen Storage.* Energies, 2011, **4**, 185-214

[11] Nakamori, Y. et al.: *Correlation between thermodynamical stabilities of metal borohydrides and cation electronegativities: First-principles calculations and experiments.* Phys. Rev. B., 2006, **74**, 045126

[12] Jensen, T., Filinchuk, Y. et al.: $LiCe(BH_4)_3Cl$*, a New Lithium-Ion Conductor and Hydrogen Storage Material with Isolated Tetranuclear Anionic Clusters.* Chem. Materials, 2012, **24**, 1654-1663

[13] Vajo, J. J. et al.: *Thermodynamic destabilization and reaction kinetics in light metal hydride systems.* J. Alloys Compd., 2007, **446-447**, 409-414

[14] Jensen, C. M.: *Complex hydrides for Hydrogen Storage.* Chem. Rev., 2007, **107**, 4111-4132

[15] Züttel, A. et al.: *Hydrogen: The future energy carrier.* Phil. Trans. R. Soc. A, 2010, **368**, 3329-3342

[16] Homepage of U. S. Department of Energy, 29.04.13 <http://www.fueleconomy.gov/feg/fcv_sbs.shtml>

[17] Hemmer, P. C.: *Faste stoffers fysikk.* Tapir forlag, Trondheim, 1987

[18] Giacovazzo, C. et al.: *Fundamentals of Crystallography.* Oxford University Press Inc., New York, 1992

[19] Kittel, C.: *Introduction to Solid State Physics.* John Wiley & Sons, Inc., 8th Edition, 2005

[20] v. Issendorff, B.: *Lectures on Solid State Physics.* Albert-Ludwigs Universität Freiburg, 2012

[21] David, W. I. F. et al.: *Structure Determination from Powder Diffraction Data.* Oxford University Press Inc., New York 2002

[22] Gennari, F. C. et al.: *Destabilization of* $LiBH_4$ *by* $MH_2$ *(M = Ce, La) for hydrogen storage: Nanostructural effects on the hydrogen sorption kinetics.* Int. J. Hydrogen Energy 2011, **36**, 15231-15238

[23] Züttel, A. et al.: *Tetrahydroborates as new hydrogen storage materials.* Scripta Materialia, 2007, **56**, 823-828

[24] Orimo, S. et al.: *Material properties of* $MBH_4$ *(*$M = Li, Na$*, and* $K$*).* Mater. Sci. Eng. B, 2004, **108**, 51-53

[25] Hummelshøj, J.S. et al.: J. Chem. Phys., 2009, **131**, 14101-14109

[26] Hagemann, H. et al.: $LiSc(BH_4)_4$*: A Novel Salt of* $Li^+$ *and Discrete* $Sc(BH_4)_4^-$ *Complex Anions.* J. Phys. Chem. A 2008, **112**, 7551-7555

[27] Bogdanovic, B. and Schwickardi, M.: *Ti-doped* $NaAlH_4$ *as a hydrogen-storage material - preparation by Ti-catalyzed hydrogenation of aluminum powder in conjunction with sodium hydride.* Appl. Phys. A, 2001, **72**, 221-223

[28] Rude, L. H. et al.: *Tailoring properties of borohydrides for hydrogen storage: A review.* Phys. Status Solidi A, 2011, **208**, 8, 1754-1773

[29] Soulie, J.P. et al: *Lithium boro-hydride* $LiBH_4$. Journal of Alloys Compd., 2002, **346**, 200-205

[30] Züttel, A. et al.: *Hydrogen storage properties of* $LiBH_4$. Journal of Alloys Compd., 2003, **356**, 515-520

[31] Kang J. K. et al.: *Lightest borohydride probed by synchrotron X-ray diffraction: Experiment calls for a new theoretical revision.* J. Phys. Chem. C, 2008, **112**, 10579-10584

[32] Arnbjerg, L. M. et al.: *Structure and Dynamics for LiBH4-LiCl Solid Solutions.* Chem. Materials, 2009, **21**, 5772-5782

[33] Matsuo, M. et al.: *Stabilization of lithium superionic conduction phase and enhancement of conductivity of* $LiBH_4$ *by LiCl addition.* Appl. Phys. Lett., 2009, **94**

[34] Aylard, G. and Findlay, T.: *SI Chemical Data.* 6th edition, John Wiley & Sons Australia, Ltd., Milton 2008

[35] Orimo, S. et al.: *Experimental studies on intermediate compound of* $LiBH_4$. Appl. Phys. Lett., 2006, **89**, 021920

[36] Orimo, S. et al.: *Dehydriding and rehydriding reactions of* $LiBH_4$. J. Alloys Compd., 2005, **404-406**, 427-430

[37] Jin, S. et al.: *Reversible hydrogen storage in* $LiBH_4 - MH_2$ *(M = Ce, Ca) composites.* J. Phys. Chem. C, 2008, **112**, 9520-9524

[38] Shim, J. et al.: *Effect of hydrogen back pressure on dehydrogenation behavior of* $LiBH_4$*-based reactive hydride composites.* J. Phys. Chem. Let., 2010, **1**, 59-63

[39] Gennari, F. C. and Esquivel, M.R.: *Synthesis and dehydriding process of crystalline* $Ce(BH_4)_3$. J. Alloys Compd., 2009, **485**, 47-51

[40] Frommen, C. et al.: *Synthesis, Crystal Structure, and Thermal Properties of the First Mixed-Metal and Anion-Substituted Rare Earth Borohydride* $LiCe(BH_4)_3Cl$. J. Phys. Chem. C, 2011, **115**, 23591-23602

[41] Ley, M.B. et al.: $LiCe(BH_4)_3Cl$*, a New Lithium-Ion Conductor and Hydrogen Storage Material with Isolated Tetranuclear Anionic Clusters.* Chem. Mat., 2012, **24(9)**, 1654-1663

[42] Olsen, J. E. et al.: *Crystal structures and properties of solvent-free* $LiYb(BH_4)_{4-x}Cl_x$, $Yb(BH_4)_3$ *and* $Yb(BH_4)_{2-x}Cl_x$. RSC Adv., 2013. DOI: 10.1039/C3RA40435H

[43] Gennari, F. C. et al.: *Reversible hydrogen storage from* $6LiBH_4 - MCl_3$ *(M = Ce, Gd) composites by* in-situ *formation of* $MH_2$. Int. J. Hydrogen Energy, 2011, **36**, 536-570

[44] Coppens, P.: *Synchrotron Radiation Crystallography.* Academic Press Ltd., London, 1992

[45] Homepage of DECTRIS Ltd., 23.11.12 <https://www.dectris.com/>

[46] Leon, A.: *Hydrogen Technology. Mobile and Portable Applications.* Springer-Verlag, Heidelberg, 2008

[47] Broom, D. P.: *The accuracy of hydrogen sorption measurements on potential storage materials.* Int. J. Hydrogen Energy, 2007, **32**, 4871-4878

[48] Blach, T. P. and Gray, E. MacA.: *Sieverts apparatus and methodology for accurate determination of hydrogen uptake by light-atom hosts.* J. Alloys Compd., 2007, **446-447**, 692-697

[49] Homepage of National Institute of Standards and Technology, 26.04.13 <http://webbook.nist.gov>

[50] Hemmes, H. et al.: *Thermondynamic properties of hydrogen at pressures up to 1 Mbar and temperatures between 100 and 1000 K.* J Phys C Solid State Phys 1986, **19**, 3571-3585

[51] Homepage of the Inorganic Crystal Structure Database, 10.05.13 <http://www.fiz-karlsruhe.de/icsd_home.html>

[52] Louer, D. and Boultif, A.: *Trial and Error Method for the Automatic Indexing of Powder Diffraction Patterns - Variation of Parameters by Successive Dichotomy.* J. Appl. Cryst., 2004, **37**, 724-731

[53] Favre-Nicolin, V. and Cerny, R.: *FOX, 'free objects for crystallography': a modular approach to ab initio structure determination from powder diffraction.* J. Appl. Cryst., 2002, **35**, 734-743

[54] Toby, B. H.: *EXPGUI, a graphical user interface for GSAS.* J. Appl. Cryst., 2001, **34**, 210-213

[55] Larson, A.C. and Von Dreele, R.B.: *General Structure Analysis System (GSAS).* Los Alamos National Laboratory Report LAUR, 1994, 86-748

[56] McQuaker, Neil Robert *Vibrational spectra of the ammonium halides and the alkali-metal borohydrides.* University of British Columbia, 1970

[57] Zavorotynska, O. et al.: *Vibrational Properties of $MBH_4$ and $MBF_4$ Crystals ($M$ = Li, Na, K): A Combined DFT, Infrared, and Raman Study.* J. Phys. Chem. C, 2011, **115(38)**, 18890-18900

[58] Ferraro, J. R. et al.: *Introductory Raman Spectroscopy.* 2nd edition. Academic Press, San Diego, California 2003.

[59] Sirdeshmukh, D.B. et al.: *Alkali Halides. A handbook of physical properties.* Springer-Verlag, Heidelberg, 2001

[60] Holley, C. E. jr. et al.: *The crystal structure of some rare earth hydrides.* J. Phys. Chem., 1955, **59**, 1226-1228'

[61] Warf, J. C. and Hardcastle, K. I.: *Rare Earth-Hydrogen Systems. IV. The Higher Hydride of Ytterbium, a New Type of Hydride.* J. Am. Chem. Soc., 1961, **83**, 1736-1740